
Doctoral Dissertations

Student Theses and Dissertations

Spring 2019

Design, fabrication, and characterization of functionally graded materials

Sreekar Karnati

Follow this and additional works at: https://scholarsmine.mst.edu/doctoral_dissertations



Part of the [Mechanical Engineering Commons](#)

Department: Mechanical and Aerospace Engineering

Recommended Citation

Karnati, Sreekar, "Design, fabrication, and characterization of functionally graded materials" (2019).
Doctoral Dissertations. 3098.

https://scholarsmine.mst.edu/doctoral_dissertations/3098

This thesis is brought to you by Scholars' Mine, a service of the Missouri S&T Library and Learning Resources. This work is protected by U. S. Copyright Law. Unauthorized use including reproduction for redistribution requires the permission of the copyright holder. For more information, please contact scholarsmine@mst.edu.

DESIGN, FABRICATION, AND CHARACTERIZATION OF FUNCTIONALLY
GRADED MATERIALS

by

SREEKAR KARNATI

A DISSERTATION

Presented to the Graduate Faculty of the

MISSOURI UNIVERSITY OF SCIENCE AND TECHNOLOGY

In Partial Fulfillment of the Requirements for the Degree

DOCTOR OF PHILOSOPHY

in

MECHANICAL ENGINEERING

2019

Approved by

Frank F. Liou, Advisor

Douglas A. Bristow

Edward C. Kinzel

Heng Pan

Joseph W. Newkirk

Copyright 2019
SREEKAR KARNATI
All Rights Reserved

PUBLICATION DISSERTATION OPTION

This dissertation consists of the following three articles which have been submitted for publication, or will be submitted for publication as follows:

Paper I: Pages 9-33 have been submitted to The International Journal of Advanced Manufacturing Technology.

Paper II: Pages 34-64 are intended for submission to Metals.

Paper III: Pages 65-83 have been submitted to Progress in Additive Manufacturing.

ABSTRACT

The aim of this research was to investigate the feasibility of fabricating custom designed, graded materials using Laser Metal Deposition (LMD) that will cater for functionality and unconventional repair. The ultimate goal of the project is to establish the versatility of LMD for fabricating advanced materials and tackling problems that have been conventionally difficult or in cases infeasible. In order to accomplish these goals, this research involved investigations into, the feasibility of using elemental powders as modular feedstocks, the feasibility of fabricating tailored gradients with these custom compositions, and finally leveraging the advantages of grading materials using LMD to successfully fabricate conventionally infeasible material systems. The copper-nickel material system was chosen for demonstrating the modular feedstock concept. While the use of elemental nickel lead to porosity issues, Delero-22 a nickel-silicon-boron alloy was identified as a viable substitute. A wide range of copper-nickel alloys were fabricated through the deposition of blended powder feedstocks. Also, using these blended powder feedstocks, graded material structures of copper-nickel alloys were successfully fabricated. Varying energy input through pulse width modulation of laser power was identified as a viable means for manipulating chemistry gradient within these graded materials. The influence of varying chemistry on mechanical properties was evaluated through the use of DIC coupled mini-tensile testing. A clear distinction in the strain field indicating the spatially varying chemistry was identified during tensile testing. Also, the feasibility of depositing on highly reflective alloys of aluminum such as Al2024 and Al6061 was also investigated. Leveraging the higher absorptivity of Al4047 and remelting during LMD, a strong metallurgical bond was obtained between the substrate and the deposit. Preheating the substrate was identified to increase the reliability and quality of deposition. The bond between the substrate and deposit was found to be stronger than the deposit.

ACKNOWLEDGMENTS

I would like to express my sincere gratitude to my advisor and mentor Dr. Frank F. Liou for believing in me and for giving me the opportunity to work on various exciting projects in LAMP lab. I am immensely grateful for the exposure and guidance I received during my tenure at Missouri S&T. I would like to thank Dr. Joseph W. Newkirk for the close participation, advice, and guidance that he has provided throughout this endeavor. I would also like to thank my committee members, Dr. Douglas A. Bristow, Dr. Edward C. Kinzel and Dr. Heng Pan for their insightful comments and encouragement. I'd like to also thank the Department of Mechanical Engineering, Department of Materials Science and Engineering, Advanced Materials Characterization Lab and Material Research Center for their support on various aspects of this research.

My sincere thanks also goes to Dr. Sriram Praneeth Isanaka for his encouragement, advice, and critique on various aspects of this work. I am thankful to the members of the LAMP lab for making this journey an exciting and educational experience. Especially Aaron Flood and Todd E. Sparks for the several insightful discussions into various aspects of science and life. I am also grateful for the support I received from all my friends at Rolla.

Finally, I would like to express my deep gratitude to my parents, Dr. Somaiah Karnati and Mrs. Shantha Devi Karnati, and my sister Priyanka Karnati for their unconditional love and support. Without their never-ending positivity and encouragement, I would not have been able to pursue my interests with such passion.

TABLE OF CONTENTS

	Page
PUBLICATION DISSERTATION OPTION	iii
ABSTRACT	iv
ACKNOWLEDGMENTS	v
LIST OF ILLUSTRATIONS	ix
LIST OF TABLES	xiii
 SECTION	
1. INTRODUCTION	1
1.1. TECHNICAL OBJECTIVES	3
1.2. RESEARCH NEED	4
1.2.1. Pre-Alloyed Powders vs. Blended Powders	5
1.2.2. Copper-Nickel Material System	5
1.2.3. Tailored Grading	6
1.2.4. Aluminum Deposition	7
 PAPER	
I. CHARACTERIZATION OF COPPER-NICKEL ALLOYS FABRICATED USING LASER METAL DEPOSITION AND BLENDED POWDER FEEDSTOCKS	9
ABSTRACT	9
1. INTRODUCTION	10
2. EXPERIMENTAL SETUP	13

3. RESULTS AND DISCUSSION	14
4. CONCLUSIONS	30
ACKNOWLEDGEMENTS	31
REFERENCES	31
II. ON THE FEASIBILITY OF TAILORING COPPER-NICKEL FUNCTION- ALLY GRADED MATERIALS FABRICATED THROUGH LASER METAL DEPOSITION	34
ABSTRACT	34
1. INTRODUCTION	35
2. MATERIALS AND METHODS	37
3. RESULTS AND DISCUSSION	41
3.1. DEPOSITION OF 100/0 AND 30/70 FEEDSTOCKS	41
3.2. DISSIMILAR GRADED MATERIAL DEPOSITION.....	45
4. CONCLUSIONS	60
ACKNOWLEDGEMENTS	61
REFERENCES	61
III. SUBSTRATE PREHEATING DURING LASER METAL DEPOSITION OF AL4047 ON AL2024 AND AL6061	65
ABSTRACT	65
1. INTRODUCTION	66
2. RATIONALE.....	67
3. EXPERIMENTAL SETUP	69
4. RESULTS AND DISCUSSION.....	71
5. CONCLUSIONS	80
ACKNOWLEDGEMENTS	81
REFERENCES	81

SECTION

2. CONCLUSIONS	84
REFERENCES	85
VITA	87

LIST OF ILLUSTRATIONS

Figure	Page
1.1. Instantaneous melt pool composition for different powder mixtures and re-melting depths and overlaps (calculated basing rule of mixtures) while depositing a horizontal layer.	7
 PAPER I	
1. Schematic diagram of the deposition setup during a thin wall deposition.	13
2. (a) Dimensions of the miniature tensile specimen in mm, (b) Specimen loaded in the self-aligning grips with extensometer set, (c) Specimen broken after the test.	15
3. As-deposited microstructures of elemental powder blends (Etched using 70% volume nitric acid).....	16
4. XRD plots of material fabricated from elemental copper-nickel powder blends. .	17
5. The as-blended composition of powder feedstocks and optical images of the microstructures (as polished) of as-deposited (fabricated in Ar and N ₂ atmospheres) material from respective blends.....	20
6. The Vickers hardness values (10gm load) plotted against the weight percentage of Delero-22(remaining elemental nickel powder) in the blend.	21
7. XRD peak patterns from as-deposited material made using blends of elemental copper and Delero-22 alloy powders.	21
8. Variation in hardness with increasing copper content.	22
9. SEM image and the EDS line scan analysis data gathered across the dendritic (copper-nickel solid solution) , matrix (Ni ₃ B) and dendritic phases on a 75% Delero-22 deposit.....	23
10. Optical micrographs of the as-deposited microstructure (etched using 70% vol. nitric acid) using powder blends listed in Table 4.	26
11. Secondary dendrite arm spacing measurements with one standard deviation error bars for all 5 blends under varying scan speed.	27
12. Box plot charts of mechanical properties gathered from miniature tensile testing.	28
13. The fracture surfaces of miniature tensile samples made from blends listed in Table 4.	29

PAPER II

1.	A schematic representation of the LMD deposition process used in the study. ...	38
2.	Power and Duty Cycle (D.C.) values used in the initial 4 layers at the dissimilar material interface while fabricating the copper-nickel FGM thin-wall deposits...	40
3.	Dimensions of the miniature tensile test specimen; all the dimensions are in mm.	41
4.	Machined thin-wall deposits of solely nickel-rich 100/0 (left) and copper-rich 30/70 (right) with a significant difference in overall height for the same 40 layers of deposition.	42
5.	Peak patterns of 100/0 and 30/70 from X-ray Diffraction analysis.	43
6.	Optical microscope images of (a) 100/0 nickel-rich deposit and (b)30/70 copper-rich deposit (c) bands of coarsened dendrites on 100/0 deposits, suspected to be originating from remelting during successive layer by layer deposition.	44
7.	Optical microscope image of 100/0 nickel-rich deposit taken using Nomarski interference contrast.	45
8.	EDS line scan analysis across the dendritic and inter-dendritic phases on an as-polished 30/70 deposit.	46
9.	Copper-nickel FGM deposit fabricated with 100/0 as the pre-deposit and 30/70 as the second deposit. Set 3 duty cycle ramp down parameter were used at the dissimilar material interface.	47
10.	Optical microscope image of the dissimilar material interface on a graded material deposit fabricated by depositing 30/70 on 100/0 using the set 1 (see Figure 2) duty cycle ramp down.	48
11.	EDS line scan analyses across dissimilar graded material interfaces for the three sets, (a) set 1, (b) set2 and (c) set 3, of duty cycle ramp downs (see Figure 2) when 100/0 nickel-rich deposit was fabricated on 30/70 copper-rich pre-deposit.	49
12.	EDS line scan analyses across dissimilar graded material interfaces for the three sets, (a) set 1, (b) set2 and (c) set 3, of duty cycle ramp downs (see Figure 2) when 30/70 copper-rich deposit was fabricated on 100/0 nickel-rich pre-deposit.	50
13.	Length of the chemical gradient for the different cases of graded material deposition as measured from Figure 11 and Figure 12.	51
14.	Schematic diagram of transverse sections of FGM deposits detailing the influence of remelting on the gradient development during dissimilar material deposition.	53

15.	Variation in Vickers hardness values (HV0.2) along the height of the graded material deposits.....	55
16.	Strain fields calculated from gage length elongation values calculated from DIC analysis for (a) Set 1 100/0 on 30/70, (b) Set 1 30/70 on 100/70, (c) Set 3 100/0 on 30/70 and, (d) Set 3 30/70 on 100/0 deposits.	56
17.	Box and whisker plots of (a) 0.2% Offset yield strength, (b) Ultimate tensile strength and (c) strain at break from crosshead displacement for the miniature tensile specimens prepared from deposits of different combinations.	57
18.	Silica inclusion on the fracture surface of a tensile specimen prepared from Set 3 30/70 on 100/0 deposit.....	57
19.	Strain values calculated along the center-line of the gage length of miniature tensile specimens cut from deposits of Set 1 duty cycle for 100/0 on 30/70.....	58
20.	Strain values calculated along the center-line of the gage length of miniature tensile specimens cut from deposits of Set 1 duty cycle for 30/70 on 100/0.....	59
21.	Strain values calculated along the center-line of the gage length of miniature tensile specimens cut from deposits of Set 3 duty cycle for 100/0 on 30/70.....	59
22.	Strain values calculated along the center-line of the gage length of miniature tensile specimens cut from deposits of Set 3 duty cycle for 30/70 on 100/0.....	60

PAPER III

1.	Deposition of Al4047 on Al2024 through sintering followed by remelting [19]. .	68
2.	Top view of 4 replications of 8 layer deposits of Al4047 on an Al2024 substrate. Power of 1kW and 150mm/min scan speed were used for all deposits.	69
3.	Schematic layout of the deposition system used in the current study.	70
4.	Dimensions of the miniature tensile specimen in mm (top).	72
5.	2inch long deposit of Al4047 on an Al6061 substrate at room temperature (left) and 1inch long deposit of Al4047 on an Al6061 substrate preheated to 473K (right).....	72
6.	Stitched optical microscope images of microstructure gathered at the interfaces of deposits of all conditions.	74
7.	Secondary electron image with a false color overlay of EDS area map showing the silicon (yellow) and aluminum (blue) in the microstructure of Al4047 deposit.	75
8.	EDS line scan data gathered across the interface of an Al4047 deposit on an Al2024 substrate with substrate preheat.	76

9.	95% confidence intervals of measured SDAS values and calculated average cooling rates.	77
10.	Variation of microhardness across the substrate-deposit interface of Al4047 deposits on both Al2024 and Al6061 alloys.....	78
11.	Mechanical property values from mini-tensile testing with one-sigma error bars.	79
12.	Fracture surface images of broken minitensile sample with ductile (left, alpha aluminum) and brittle (right, silicon) failure signatures.	80

LIST OF TABLES

Table	Page
PAPER I	
1. The composition of Delero-22 alloy in weight percentage.	14
2. The composition of blends listed in 3.	16
3. The relative as-blended and as-deposited composition of copper, and, nickel in %wt.	22
4. The set of powder blends mixed to match commercially available copper-nickel alloys.	24
PAPER II	
1. The composition of Delero-22 alloy in weight percentage.	39
2. Compositions of blended powder feedstocks used in the study.....	39
PAPER III	
1. Optimized process parameters employed in the experimentation.	71

SECTION

1. INTRODUCTION

Functionally Graded Materials (FGM) are monolithic, inhomogeneous materials whose anisotropy is tailored per a designer's definition to cater to a specific application. The concept of FGM was first proposed by material scientists investigating novel means for fabricating thermal barrier materials [1]. Spatially altering the material properties or material composition can be used to achieve such anisotropy. Techniques such as plasma spraying [2], die compaction [3], powder metallurgy [4], slip casting [5], and additive manufacturing [6] have been shown to be successful in fabricating FGMs. Apart from Additive Manufacturing (AM), these processes though possess limited scope for attaining fine resolution (localized spatial control) in grading material composition. These techniques are also limited in their capability for fabricating complex geometries. Laser Metal Deposition (LMD), on the other hand, is quite versatile and competent in fabricating complex geometries. The localized delivery of the feed material in LMD provides the unique opportunity of tailoring composition within a part. The design freedoms available through FGM when coupled with the versatility of LMD provide the scope for fabricating advanced multi-functional parts.

Existing literature on fabricating FGM using additive manufacturing is mostly limited to identifying viable material systems among the pre-alloyed powder compositions that are currently commercially available. These material compositions were originally designed and intended for production processes such as casting, welding, rolling etc. and are not customized for AM. Also, the manufacturing of these FGMs' is a complicated process due to the possible issues of incompatibility among the constituent elements. Incompatibility arises issues of difference in thermal expansion coefficients, crystal structure, and formation of detrimental intermetallic compounds [2,7-9]. Researchers have also shown

that theorizing compatibility from a strictly metallurgical perspective, i.e. a phase diagram with no possible formation of intermetallic compounds doesn't guarantee structural integrity post fabrication. This is because of the development of residual stresses from compositional variations and directional heat transfer intrinsic to additive manufacturing. Robust control and sophisticated design are crucial to overcoming the hurdles during fabrication of FGM. The potential for fabricating FGM with LMD is significant, however, a vast amount of research and investigation is required to transform these prospects into reality. Custom tailoring of compositions to make pre-alloyed powders, to meet unique and low volume grading requirements is very expensive and often requires extensive infrastructure. A simple, feasible and economical alternative would be to incorporate blended powders into the AM deposition. Premixing of powders to required compositions [10,11], or mixing powder on-line by using a multi-powder feed system[12] can be adopted to implement varying composition. However, deposition of blended powder comes with its own set of challenges. While pre-alloying has achieved limited success, successful deposition of pre-alloyed powder doesn't ensure the successful deposition of blended powders of the same composition. The difference in laser absorptivity among the blended components, coupled with the separation of powder during transport through the delivery system, can cause significant differences between as-blended and as-deposited compositions[11,13]. The as-deposited microstructure of the blended powders and pre-alloyed powders could end up being significantly different. Segregation of particles due to lack of complete melting, or density differences can also skew the composition of the as-deposited material [14].

The need of the hour is a significant amount of investigation to successfully incorporate elemental powder based fabrication into additive manufacturing. In the current research, the feasibility of fabricating various compositions of copper-nickel from blended elemental powders will be investigated. The conclusions and findings from these studies will be leveraged to design and demonstrate the feasibility of fabricating a graded system that is infeasible using conventional manufacturing.

The ability to spatially alter material properties or material composition provides the designer the capability to pre-plan and incorporate functions to different spatial locations in a component. For example, a rocket nozzle fabricated with an FGM system could be tailored to exhibit multiple benefits. The surface of the nozzle that is exposed to high temperatures and pressures can be fabricated with a material capable of minimal creep at elevated temperatures. While the composition of material surrounding these surfaces could be tailored to achieve high heat dissipation. Similarly, long-life bearings could also be fabricated by designing and fabricating them as an FGM. The contact bearing surface would comprise a hard, wear resistant composition while the supporting volume of material would be tailored to be tough and resilient. Theorization and fundamental research have been carried out to identify FGM systems for a multitude of applications such as lightweight heat exchangers, rocket nozzles, long life bearings, high-performance turbine blades etc. [2,15-18]. However, to create multi-functional, and multi-material components using additive manufacturing or LMD, developing a comprehensive strategy that will investigate the effects of geometry, composition, and, thermal history and thereby allow the creation of detailed process plans is warranted. A voxel-based path plan, where each voxel represents the position, composition (and the required process parameters to achieve it) needs to be generated in advance [15]. The work performed as a part of this research would be crucial in laying the foundation to FGM fabrication. This research would be instrumental in establishing a philosophy for choosing composition-process-geometry combinations and successfully fabricating novel FGMs.

1.1. TECHNICAL OBJECTIVES

The capability of fabricating custom compositions is critical to fabricating FGM with wide ranges of compositional variance. Incorporation of modular feedstocks such as elemental powders into LMD is critical for attaining such capabilities. The research performed under this effort will present evidence that supports the benefits and design

flexibility possible from using elemental powders. Additional flexibility in grading is also theorized to be feasible from controlling laser parameters to induce differing amounts of dilution/ re-melting. The principal objectives of this work were

- Investigate the feasibility of the fabricating various compositions of alloys using elemental powders
- Identify possible solutions to ensure successful deposition through modular feedstocks
- Fabricate tailored gradients using flexible feedstocks and controlled process parameters
- Investigate the scale of difference in material properties and mechanical performance through characterization
- Apply the knowledge gleaned from these studies, demonstrate feasibility of achieving grading in a conventionally infeasible

1.2. RESEARCH NEED

The existing literature on additive manufacturing processes based on powder feedstock involves research of mostly pre-alloyed powders. To cite a few examples, Boschetto et.al. performed their study on surface roughness using AlSi10Mg pre-alloyed powder [19]. Feng et.al. in their study on the high-temperature hardness of laser claddings used Inconel-625 as the precursor material [20]. Dutta and Froes, in their report, extensively discuss the incorporation of titanium pre-alloyed powders into various additive manufacturing techniques [21]. They state that immense cost benefits are feasible from additively manufacturing titanium and titanium alloys. They also state that additively manufactured titanium material is almost as good if not better than conventionally fabricated titanium. Although significant advances and claims have been made by using pre-alloyed powders, the compositions of these powders were originally tailored for conventional production

processes. Their incorporation in additive manufacturing often creates unforeseen challenges. The literature on these materials from conventional production processes is often not relevant or applicable for additive processes due to the vast differences in solidification dynamics.

1.2.1. Pre-Alloyed Powders vs. Blended Powders. Production and procurement of pre-alloyed powders can be a costly affair due to the need for expensive infrastructure. The adoption of a more modular approach can avoid these bottlenecks. The fabrication of a wide variety of compositions and thereby alloys becomes possible by incorporating elemental powders as feedstocks. The authors theorize that the incorporation of elemental feedstocks can exponentially expand the capability of any additive manufacturing based fabrication technology. Premixing of powders to the required composition or mixing powder on-line by using a multi-powder feed system can be adopted to implement compositional change. While employing elemental powders does look promising, there are a great number of aspects that need investigation. Particularly more knowledge pertaining to the differences between materials fabricated using pre-alloyed powders and blended powder of the same composition needs to be gathered [22]. Influence of feedstock parameters, process setup and parameters over the chemistry and microstructure of the final material needs to be assessed.

1.2.2. Copper-Nickel Material System. Copper and copper alloys are a great choice for applications requiring high electrical and thermal conductivity. They are also resistive to corrosion in alkaline environments. Nickel and its alloys, on the other hand, are known for their high strength and toughness. These alloys exhibit high strengths at elevated temperatures and possess high corrosion and oxidation resistance. An FGM involving copper and nickel would potentially be a boon to the creation of a thermal barrier system. Copper and nickel exhibit complete and mutual solubility with no possible intermetallic compound formation [23]. Both the metals have similar densities and FCC crystal structures. Copper is also highly reflective to infrared light and is therefore near impossible to deposit using fiber lasers [24]. LMD of copper-nickel blended powders is however feasible due

to the presence of nickel. The nickel powder is expected to initiate and sustain the melt pool, the copper powder would be absorbed into the melt pool and solidify as the required copper-nickel alloy. Homogenous deposition of powder blends is critical to fabricating tailored gradients in FGM. The current research involved investigation into the feasibility of fabrication, and homogeneity in the outcome material. The study also involved the characterization of the material properties of the fabricated material.

1.2.3. Tailored Grading. The strategic blending of elemental powders to manipulate feedstock composition for attaining designed gradient would be the simplest method for tailoring the FGM. Depositing series of blends of powders gives control over grading, however, this approach needs more than a few layers to attain the required gradient. Thereby, increasing the thickness of the final part. If plausible, eliminating the deposition of series of blends of powders and depositing the final composition directly can decrease the minimum thickness. However, without proper control, steep concentration gradients might be created. These gradients could create residual stresses and lead to low structural integrity. The authors believe tailored grading can be achieved through changing process parameters.

By using varied feedstock compositions, controlling the dimensions of the melt pool and portions of the melt pool corresponding to re-melting of the layers around the melt pool, one can control the composition of the newly solidified material. If there is a compositional difference between the previous and current tracks, the proportion of re-melting influences the final composition of the newly solidified material. Greater the amount of re-melting, greater the dilution from the substrate or the neighboring track. Using the rule of mixtures model, the instantaneous composition of the melt pool can be calculated, Figure 1.1 shows the variation of composition with layer number under different scenarios of re-melting and feedstock composition while assuming a hemispherical melt-pool and complete mixing.

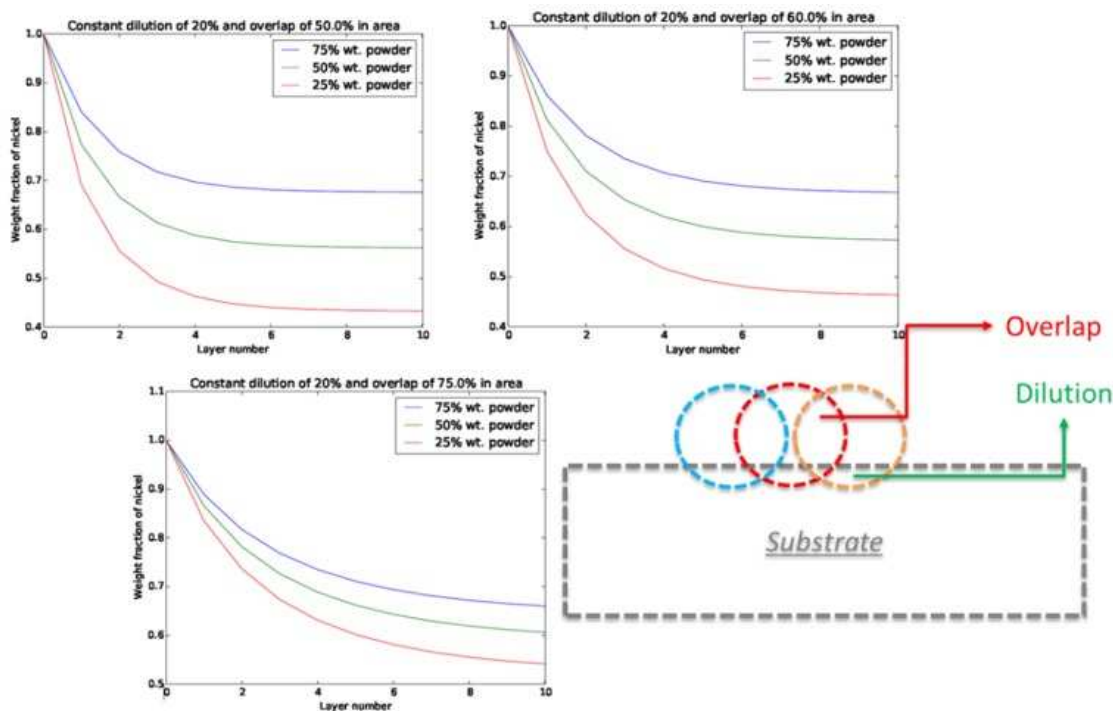


Figure 1.1. Instantaneous melt pool composition for different powder mixtures and re-melting depths and overlaps (calculated basing rule of mixtures) while depositing a horizontal layer. The composition of the substrate is 100% wt. Ni and the feed stock composition varies from 75% to 25% wt. Ni (remaining is copper).

Changing the feedstock composition and changing the track overlap can influence the grading pattern. The authors theorize controlled manipulation of these parameters can be means to achieving tailored gradients.

1.2.4. Aluminum Deposition. Aluminum alloys have always found favor in applications that have demanded high strength to weight ratios [25]. Their lower densities make them ideal for aerospace and other applications that prize weight savings while still exhibiting exceptional strength. Some aluminum alloys are even being looked at as replacements for steel. Owing to their favorable properties, they have been employed in the manufacture of a large number of aerospace components which today require repair and refurbishment. While replacement of the component is viable in some scenarios, it is an expensive solution. In other cases, even the supply chain needed to repair these legacy components have long

been shut down. In order to address this knowledge shortfall, organizations like the United States Navy are trying to develop novel solutions with the capability to additively manufacture and repair these legacy components. The research presented in this dissertation is a step in this direction, and provides a potential solution that can be adopted and implemented in existing LMD systems to address this need. An additional benefit of this research would be the ability to add features to pre-cast parts which would bridge the flexibility of LMD systems to the favorable economics of conventional manufacturing.

Pure aluminum and copper exhibit significant reflectivity to incident light [24]. Aluminum reflects approx. 92% of visible light and 98% of the near infrared radiation. Copper, on the other hand, reflects almost all of the incident near in the near infrared spectrum. However, the feasibility of depositing blended copper-nickel powders indicates that workarounds are possible for overcoming issues of reflectivity. By employing differing alloying elements, the reflectivity of the aluminum alloys can be varied and some of them can be made to be relatively more absorptive of the incident laser light. This increased absorptivity aids in the initiation of the melt pool and thereby the LMD process. This feasibility provides the prospects for repairing defects or adding features on components composed of highly reflective aluminum alloys. This dissertation includes an investigation into the feasibility of this theory.

PAPER**I. CHARACTERIZATION OF COPPER-NICKEL ALLOYS FABRICATED USING LASER METAL DEPOSITION AND BLENDED POWDER FEEDSTOCKS**

Sreekar Karnati^{*, a}, Frank F. Liou^a, Joseph W. Newkirk^b

^aDepartment of Mechanical & Aerospace Engineering

Missouri University of Science and Technology

Rolla, Missouri 65409-0050

^bDepartment of Materials Science & Engineering

Missouri University of Science and Technology

Rolla, Missouri 65409-0050

*Corresponding author, Tel: 573-341-4603, Fax: 573-341-4115

Email: skw92@mst.edu

ABSTRACT

In the current study, the feasibility of fabricating copper-nickel alloys by using laser metal deposition and blended powder feedstocks was investigated through material characterization. Material fabricated from the blended powder mixtures containing elemental nickel was seen to possess large amounts of gas and shrinkage porosity. Due to this porosity, elemental nickel powder was deemed to be an unviable modular feedstock. Instead, Delero-22, a high nickel content alloy was identified as a viable substitute for elemental nickel. The silicon and boron alloy additions in Delero-22 alloy were identified to be crucial in overcoming the porosity prevalent when using elemental nickel. Counterparts to commercially available copper-nickel alloys were then fabricated using blended

elemental copper and Delero-22 alloy powders. Thus fabricated alloys were characterized using X-Ray Diffraction, Scanning Electron Microscopy, Vickers hardness testing, Energy Dispersive X-Ray Spectroscopy, and mini-tensile testing. Analyses revealed the deposited material was formed with homogenous microstructure and the resultant compositions were close to as-blended feedstocks. The results from tensile testing showed an increase in strength caused by solid solution strengthening upon addition of copper to nickel. The addition of copper also increased the ductility of the material. Analysis of the fracture surface revealed changes in the fracture mechanism from transgranular to ductile with an increase in copper content. Variation in scan speed during laser metal deposition resulted in a change in average secondary dendrite arm spacing and variability in tensile performance.

Keywords: Elemental powders; Additive manufacturing; Laser metal deposition; Miniature tensile testing

1. INTRODUCTION

The laser metal deposition process is an additive manufacturing technology that has the ability to fabricate complicated geometries with excellent material properties. The process involves melting of blown powder in a layer by layer fashion to fabricate desired geometries. Lewis and Schlienger [1] demonstrated that the layer by layer build schema used in laser metal deposition provides the possibility of setting up a single stage manufacturing unit. The use of a powder based feedstock offers the scope for easy adoption of a wide variety of materials. The existing literature on additive manufacturing processes based on powder feedstock mostly employ pre-alloyed powders. To cite a few examples, Boschetto et al. [2] performed their study on surface roughness using AlSi10Mg pre-alloyed powder. Feng et al. [3] performed a study on the high temperature hardness of laser claddings through the use of Inconel-625 as the precursor material. Dutta and Froes [4], in their report extensively discuss the incorporation of titanium pre-alloyed powders into various additive manufacturing techniques. They state immense cost benefits are feasible from additively manufacturing

titanium and titanium alloys. They also state additively manufactured titanium material is almost as good if not better than conventionally fabricated titanium. Although significant advances and claims have been made by using pre-alloyed powders, the compositions of these powders were originally tailored for conventional production processes. Their incorporation in additive manufacturing often creates unforeseen challenges. The literature on these materials from conventional production processes is often not relevant or applicable to additive processes due to the vast differences in solidification dynamics.

Production and procurement of pre-alloyed powders can be a costly affair due to the need for expensive infrastructure. The adoption of a more modular approach can avoid these bottleneck issues. The fabrication of a wide variety of compositions and thereby alloys becomes possible by incorporating elemental powders as feedstocks. The authors theorize that the incorporation of elemental feedstocks can make the fabrication technology more advanced and capable. By doing so, a true voxel-based fabrication technology (as described by Doubrovski et al. [5]) capable of creating a monolithic part with spatially variant material properties and material composition would be possible for metals as well. Premixing of powders to the required composition or mixing powder on-line by using a multi-powder feed system can be adapted to implement compositional change. Yan et al. [6] successfully demonstrated the feasibility of fabricating Ti-6Al-4V alloy from blended elemental powders. They also studied the impact of process parameters and blend composition on output material properties. Müller et al. [7] modeled the powder transport and successfully fabricated a graded structure by varying feedstock composition online. Li et al. [8, 9] demonstrated a successful grading from titanium to steel by employing a customized transition route. This grading was only feasible due to the incorporation of elemental powders. While employing elemental powders does look promising, there are a great number of aspects that need investigation.

The feasibility of successfully depositing of a pre-alloyed powder doesn't ensure the feasibility of depositing blended powder of the same composition. The difference in laser absorptivity among the blended components, and, separation of powder during transportation can cause significant differences between as-blended and as-deposited compositions [10]. Clayton [11] investigated the feasibility of fabricating stainless steel 316, stainless steel 430 and Ti-6Al-4V alloys by using elemental powder mixtures as feedstocks. The study involved a comparison of microstructure and hardness between materials fabricated using elemental mixtures and pre-alloyed powders. The as-deposited microstructure of the blended powders and pre-alloyed powders was found to be significantly different for stainless steel 430 and Ti-6Al-4V deposits. However, the depositions of stainless steel 316 were found to produce similar material. Chen et al.[12] studied the impact of differences in particle size distributions of elemental powder mixtures on the composition of the as-deposited material. They state that differences in particle sizes and particle densities causes differences between as-deposited composition and as-blended composition. They proved, up to the spec composition can be fabricated by controlling the particle size distributions of the precursor elemental powders. Investigations performed by Schwendner et al. [13] concluded that segregation of particles due to the lack of complete melting, or density differences can also skew the composition of the as-deposited material. To conclude, a significant amount of investigation is still required to successfully incorporate elemental powder based feedstock into laser metal deposition. In the current study, an investigation into the feasibility of fabricating various compositions of copper-nickel material from blended powders was performed.

Copper and copper alloys are a great choice for applications requiring high electrical and thermal conductivity. They are also resistive to corrosion in alkaline environments. Nickel and its alloys, on the other hand, are known for their high strength and toughness. These alloys exhibit high strengths at elevated temperatures and possess high corrosion and oxidation resistance. A functionally graded system involving copper and nickel would

potentially be a boon to the creation of a thermal barrier system. Utilization of elemental copper and nickel powder feedstocks in laser metal deposition can enable the capability to produce various compositions on demand. However, this is only feasible if the laser metal deposition can produce good quality homogenous material over a wide range of blended compositions. This study aims at investigating this feasibility.

2. EXPERIMENTAL SETUP

The deposition of the materials under this study was carried out on a system equipped with a CNC stage and an edge nozzle feed setup connected to a Bay state technologies Model 1200 powder feeder. A 1kW fiber laser from IPG Photonics was used as the power source. A schematic diagram of the deposition setup is shown in Figure 1. The powders employed in the study were elemental copper (99.9% pure, from Oerlikon Metco, -100/+325 mesh, gas atomized), elemental nickel (99.9% pure, from Atlantic Engineering Equipment, -100/+325 mesh, gas atomized), and, Delero-22 alloy (composition in Table 1), from Kennametal Stellite, -100/+325, gas atomized). The powder feedstocks were prepared by mixing precisely weighed amounts of each powder in a container using a Turbula mixer. Each blend of powder was mixed for 30 minutes to ensure uniformity within the blend.

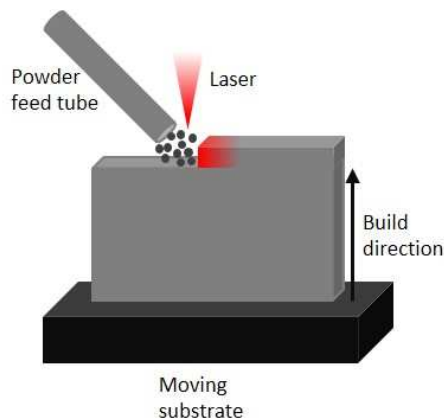


Figure 1. Schematic diagram of the deposition setup during a thin wall deposition.

Table 1. The composition of Delero-22 alloy in weight percentage.

Element	C	S	Ni	B	Cr	Fe	P	Si
Weight %	0.01	0.000	Bal.	1.3	0.0	0.4	0.003	2.4

Preliminary depositions were performed by using blends of elemental copper and elemental nickel. Later, elemental nickel powder was substituted by Delero-22 alloy. The deposited material was characterized using, a Helios Nanolab 600 SEM equipped with an Oxford Energy Dispersive X-Ray Spectrometer, a Panalytical X'pert Research Diffractometer, a Struers Duramin hardness tester, and an Instron universal testing machine. The analyses involved Scanning Electron Microscopy, Energy Dispersive X-ray Spectroscopy (EDS), optical microscopy, X-Ray Diffraction (XRD) and tensile testing towards the characterization of the material properties and microstructures.

The tensile characterization of the material was carried out by testing miniature specimens on an Instron universal testing machine. A Hansvedt DS-2 wire-EDM was used to cut these specimens to the dimensions shown in Figure 2). In case of a grip-specimen misalignment, the grips reposition minimally based on the need to avoid torquing or bending of the miniature tensile specimen. The tensile tests were carried out at a closed loop controlled strain rate of 0.015/min till a strain of 1% (for accurate offset yield strength measurement) and then the rate was ramped up to 0.5/min till failure.

3. RESULTS AND DISCUSSION

The initial stages of the study involved the fabrication and characterization of deposits made from blended powder feedstocks containing elemental nickel and elemental copper powders. The composition of these powder blends was as listed in Figure 3. These

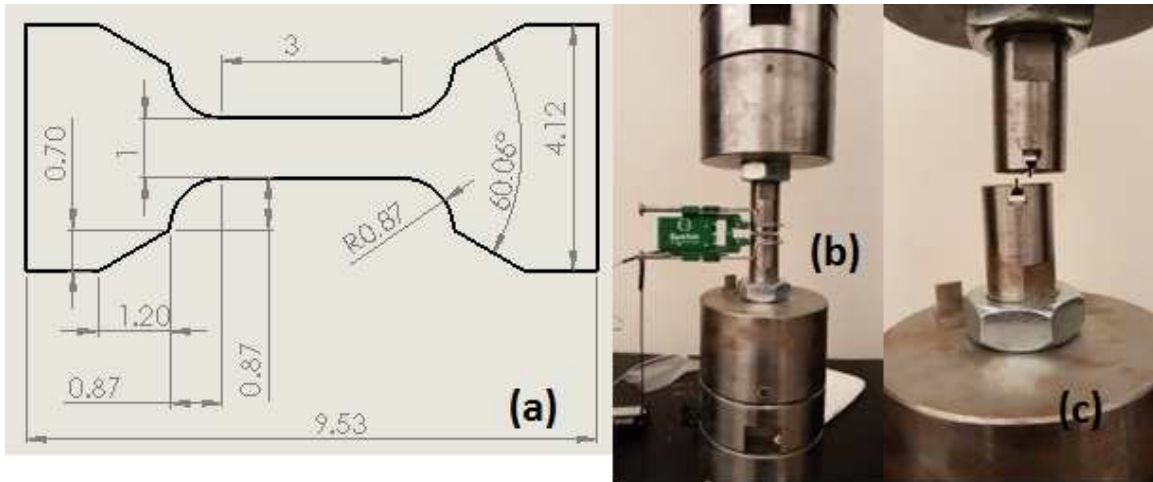


Figure 2. (a) Dimensions of the miniature tensile specimen in mm, (b) Specimen loaded in the self-aligning grips with extensometer set, (c) Specimen broken after the test.

depositions were carried out at a constant power of 700W and scan speed of 300mm/min. The deposited material was sectioned, mounted, polished and etched to reveal the microstructure.

The images of microstructure revealed gas porosity (spherical in shape) and shrinkage porosity (irregular in shape). With the exception of blend-2, all the compositions formed a single-phase material with equiaxed grains. The bright dendritic phase seen in the microstructure image of blend-2 was expected to have solidified first and the dark matrix solidified last. This contrast reflects the compositional difference between the two phases.

The occurrence of the different phases in the microstructure can be attributed to the rapid cooling of the laser metal depositions process. With increasing copper content the solidus and liquidus of the material are expected to decrease. Therefore, by using the same power parameters, the superheat in the melt pool is expected to increase with increasing copper content. This excess heat results in a slower cooling rate resulting in a homogenous microstructure. This phenomenon is theorized as the reason behind only blend-2 producing segregation. The maximum copper content in the blends was limited to 75% due to its high

reflectivity at the employed laser's operating wavelength. At levels of copper higher than that of blend-4, controllable and consistent deposition was unachievable due to difficulty in sustaining a melt pool.

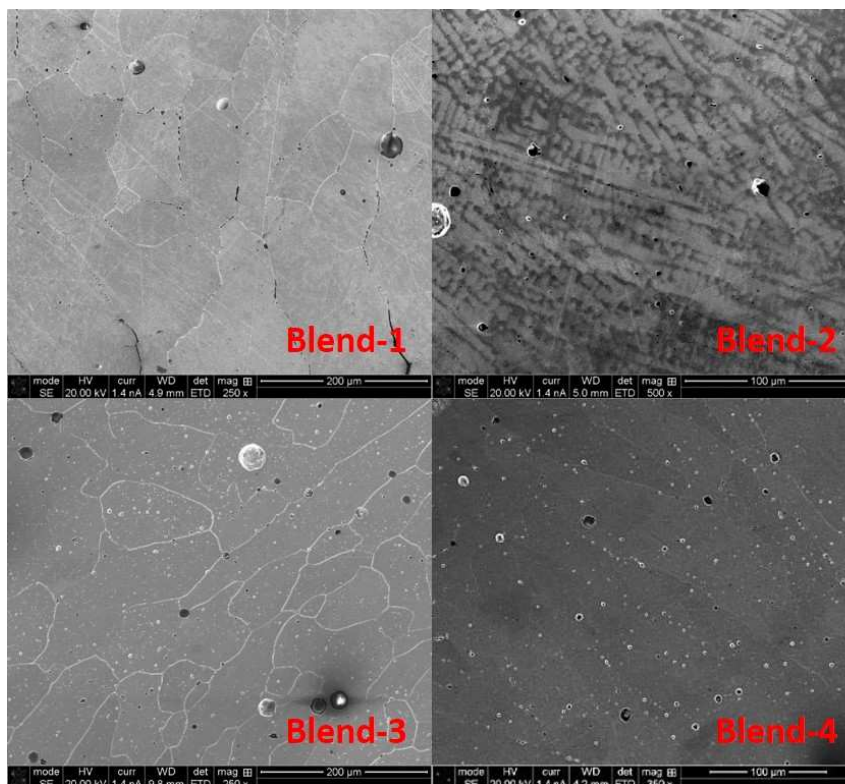


Figure 3. As-deposited microstructures of elemental powder blends (Etched using 70% volume nitric acid). Images reveal spherical gas porosity and inter-dendritic shrinkage within the deposits.

Table 2. The composition of blends listed in 3.

Element	Blend 1	Blend 2	Blend 3	Blend 4
Cu (%wt.)	0	25	50	75
Ni (%wt.)	100	75	50	25

XRD was also performed on these deposits to identify the change in peak pattern with reference to the change in copper content. This analysis also revealed that the deposited material was a single phase solid solution. The identified peak pattern ascertained the

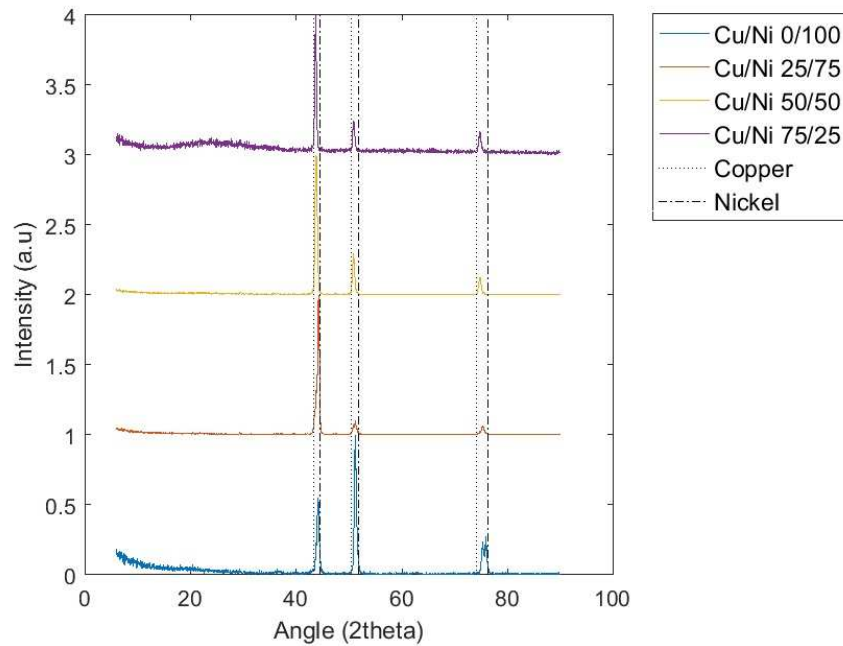


Figure 4. XRD plots of material fabricated from elemental copper-nickel powder blends. The increase in copper causes a shift in pattern from nickel peak (dot-bar-dot) positions towards copper peak (dotted line) positions.

formation of FCC crystal structure in the material. The increase in copper content was evident by the shift in XRD peak patterns from the positions close nickel towards the positions of copper [14].

Despite imposing strict inert atmosphere conditions (continuous argon purging) during deposition and powder handling, the porosity in these deposits persisted. Much of this porosity was noticed to be gas porosity (spherical pores). This porosity was suspected to be the outcome of the entrapment of the oxygen gas evolved upon dissociation of nickel oxide. It is known that nickel oxide has low thermal stability and dissociates at high temperatures causing oxygen evolution. The high surface tension of nickel [15] and the rapid cooling and solidification phenomenon of laser metal deposition. Varying process parameters to manipulate the melt pool characteristics and adding chromium to serve as a gettering agent were identified as potential means for achieving porosity free deposits.

Both of these approaches, when employed both separately and collectively, were incapable of eliminating porosity. Therefore, a substitute for elemental nickel powder was deemed necessary.

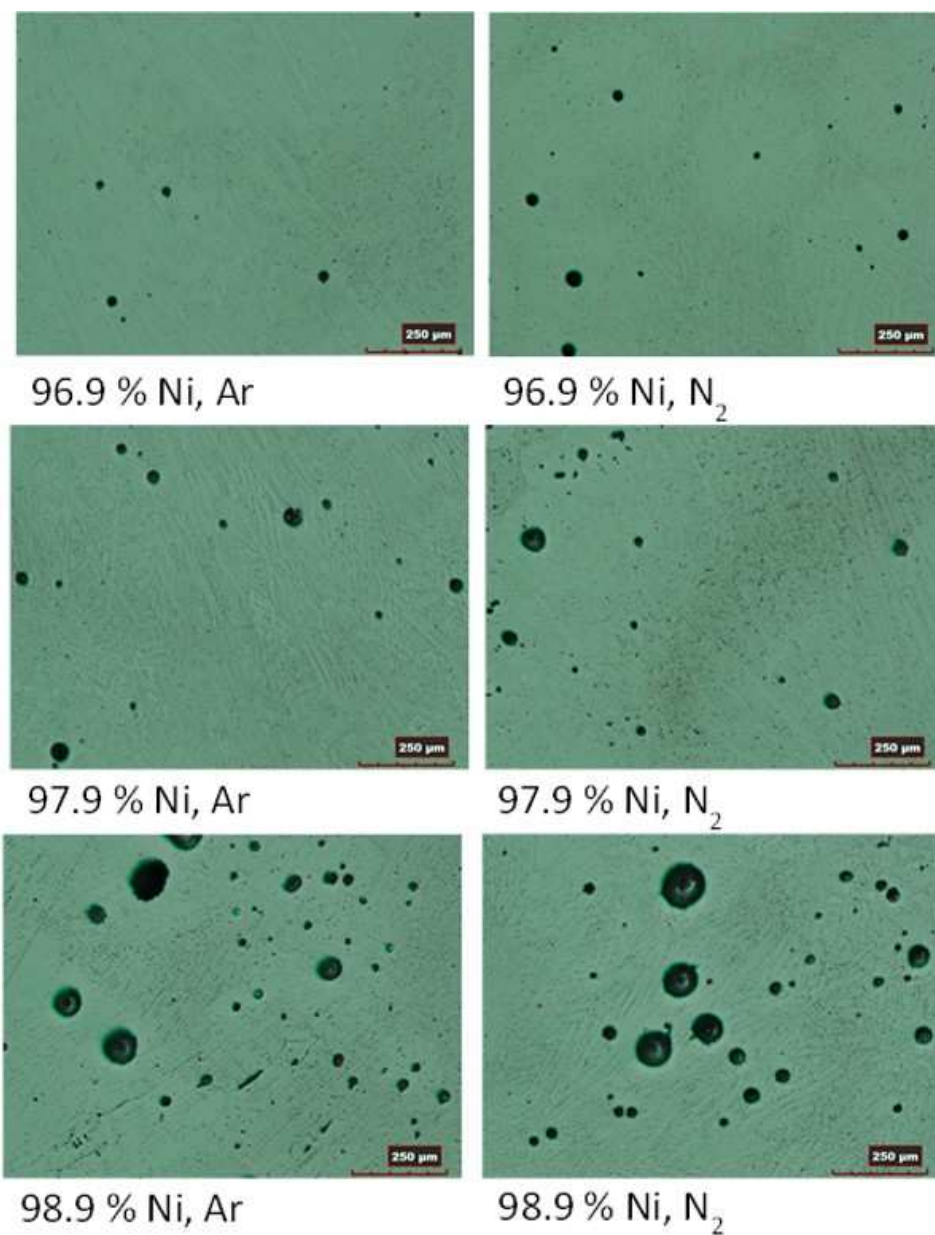
After an extensive search for suitable alloy additions and commercially available options for gas atomized powders with high nickel content, Delero-22 alloy was identified as a potential substitute for elemental nickel powder. The composition of the powder is listed in Table 1, wherein the powder has a nickel composition equivalent to 96% in weight. This alloy is traditionally used for thermal spray applications. The authors anticipated the silicon and boron alloy additions to improve the fluidity of nickel and also provide oxygen gettering during deposition. Silicon is completely soluble in nickel (at current weight % of silicon) but boron forms nickel boride [16, 17]. The presence of these borides increases the hardness and wear resistance of the alloy. While this composition of the alloy was optimized for thermal spraying applications, its applicability for laser metal deposition had yet to be investigated.

Blends of powder with elemental nickel and Delero-22 alloy were deposited to assess the impact of silicon and boron towards porosity elimination. These deposits were also expected to find if a viable blend with higher (>96% wt.) nickel was possible. The composition of the powder blends and the corresponding microstructure of the as-deposited material are shown in Figure 5. These depositions were carried out in both argon and nitrogen atmospheres, as literature [18] showed a significant impact of shielding atmosphere on porosity formation in laser welding of nickel alloys. With increasing silicon and boron content, a significant decrease in porosity was observed. Porosity persisted in the deposits fabricated under both atmospheres. Low amounts of intermittent porosity were found in blend 1 deposits as well (Figure 5). However, the material deposited using just Delero-22 alloys was near-fully dense. Therefore, this point onwards, Delero-22 alloy was used as the source material for nickel in all powder feedstocks.

From the images of microstructure in Figure 5, it is evident that by incorporating Delero-22 alloy, the as-deposited material was no longer constituted by a single phase but a dual phase material. The presence of nickel boride can be realized through the rise in mean hardness values with increase in wt. % of Delero-22 (Figure 6). The nickel boride phase was identified to be Ni_3B , after comparing the crystallographic data gathered from XRD to existing literature (see Figure 7) [19]. With increasing weight % of boron, the boride phase is expected to become more prominent and thereby cause an increase in hardness. The large standard deviation in the micro-hardness values in Figure 6 can be attributed to the wide difference in hardness of the nickel and nickel boride phases.

As porosity-free deposits were now feasible with Delero-22 alloy, different blends of copper-Delero-22 (composition listed in Figure 7) were mixed and deposited. A constant power of 750W and a constant scan speed of 500 mm/min were used for deposition. The XRD peak patterns gathered from these deposits are shown in Figure 7. Two phases, the first a copper-nickel solid solution (FCC crystal structure), and the second a nickel boride (Ni_3B) phase were identified from the peak patterns. The FCC peak pattern was observed to shift from nickel peak locations towards copper peak locations with increasing copper content. Nickel boride phase was present within detection limits of XRD in deposits of 100, 75, and, 50% wt. Delero-22 alloy. The boride peaks were absent in the peak pattern from the deposit with 25% wt. Delero-22 alloy.

Microhardness measurements were performed on the copper-Delero-22 deposits using a Vickers hardness tester. The hardness data plotted against the as-blended copper composition is shown in Figure 8. The mean hardness values were observed to decrease with increasing copper content. The standard deviation was also observed to decrease with increasing copper content. This could be attributed to the nickel boride phase becoming less prominent.



Blend #	Deloro-22 wt. %	Elemental Ni wt. %	Total Ni wt. %
1	75	25	96.9
2	50	50	97.6
3	25	75	98.9

Figure 5. The as-blended composition of powder feedstocks and optical images of the microstructures (as polished) of as-deposited (fabricated in Ar and N₂ atmospheres) material from respective blends. The porosity was noticed to substantially decrease with increasing silicon and boron content under both atmospheres.

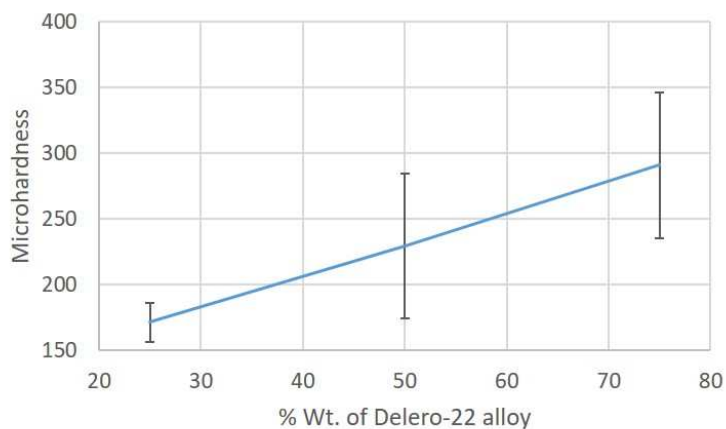


Figure 6. The Vickers hardness values (10gm load) plotted against the weight percentage of Delero-22(remaining elemental nickel powder) in the blend.

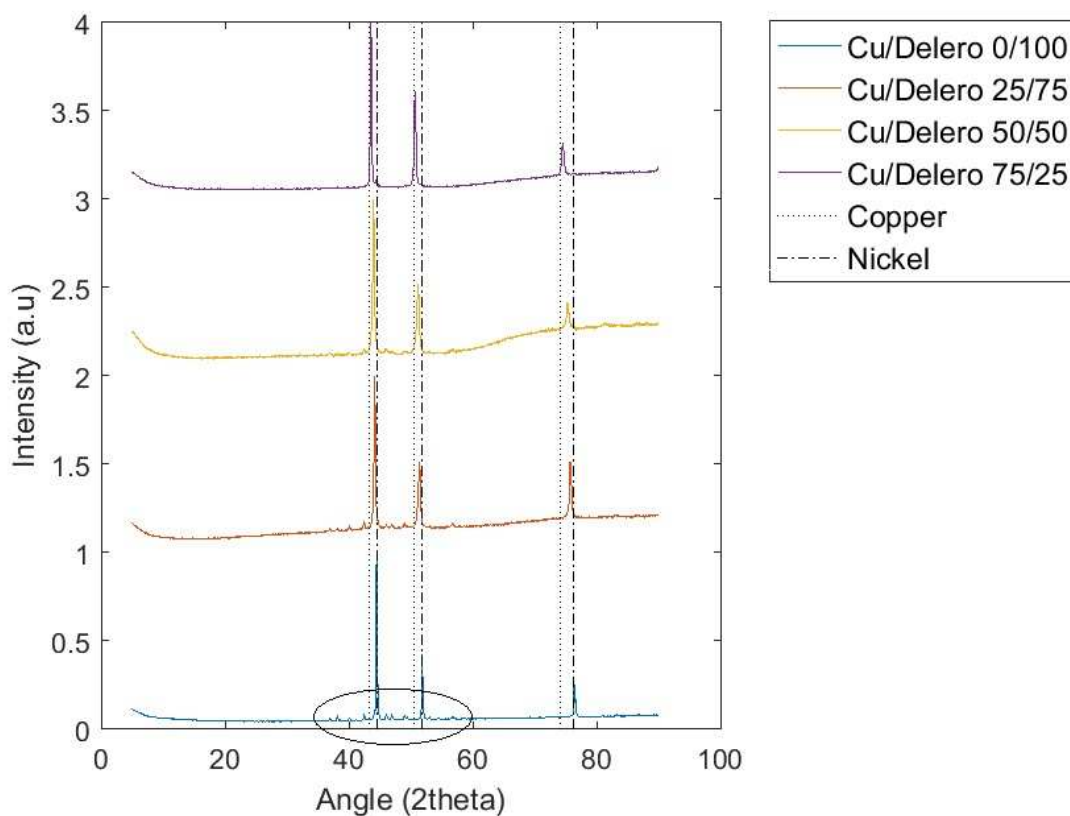


Figure 7. XRD peak patterns from as-deposited material made using blends of elemental copper and Delero-22 alloy powders. The peaks in highlighted by the oval pertain to Ni_3B .

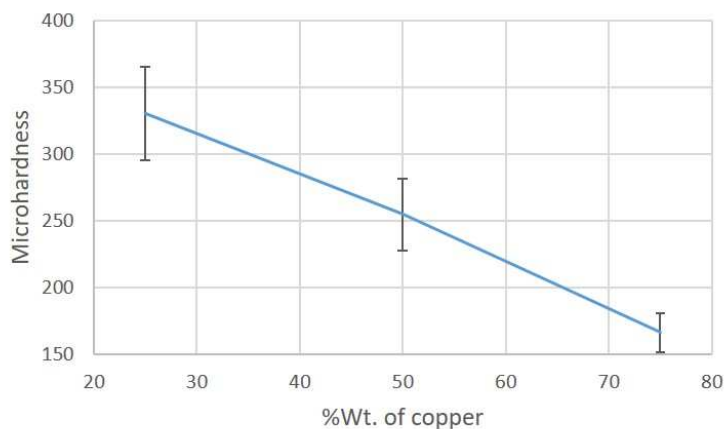


Figure 8. Variation in hardness with increasing copper content.

Standard-less EDS analyses (point and line scan) were performed to quantify the chemistry of the fabricated material. The as-blended compositions, as-blended copper to nickel ratios and copper to nickel ratios in as-deposited material, obtained from EDS analyses, are shown in Table 3. The amount of copper and nickel were approximately within 4% of weight from the as-blended compositions.

Table 3. The relative as-blended and as-deposited composition of copper, and, nickel in %wt.

Blend #	Delero-22 alloy %wt.	Elem. Cu %wt.	Rel. Ni %wt. blended	Rel. Cu %wt. blended	Rel. Ni %wt. deposited	Rel. Cu %wt. deposited
1	75	25	74	26	77	23
2	50	50	49	51	46	54
3	25	75	24	76	20	80

Line scan EDS analysis was performed across the phases to capture the presence of nickel boride in the microstructure. Boron is a lower atomic number element and is not easily detected by EDS analysis. However, it is known that the nickel boride phase will be the last phase to solidify (interdendritic phase) due to its lower melting point. A line scan

analysis across the boundary of the dendritic and interdendritic phases is shown in Figure 9. Nickel and copper are found to be homogeneously present in the dendritic phase. The peaks of nickel and complimentary troughs of copper and silicon are representative of the Ni_3B phase(matrix). Also, some amount of segregation of silicon can be noticed around the Ni_3B matrix. However, within the dendritic phase, silicon appears to be homogeneously distributed. Although the nickel boride peaks were absent in the XRD peak pattern of 25% Delero-22 deposit (see Figure 7), nickel boride was found to be present through EDS analysis.

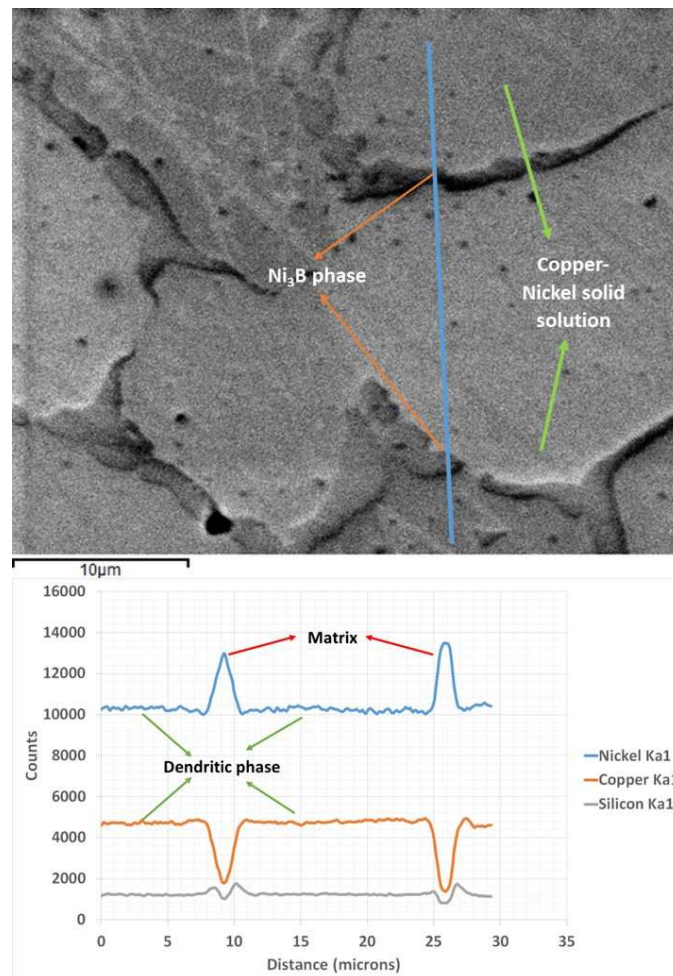


Figure 9. SEM image and the EDS line scan analysis data gathered across the dendritic (copper-nickel solid solution) , matrix (Ni_3B) and dendritic phases on a 75% Delero-22 deposit. The peaks in nickel composition belong to Ni_3B phase.

Upon the success of fabricating flaw free copper-nickel deposits, the study was expanded towards the fabrication and characterization of compositions equivalent to commercial copper/nickel alloys. The blend designations and their compositions are shown in Table 4.

Table 4. The set of powder blends mixed to match commercially available copper-nickel alloys.

Elem.	Blend 1	Blend 2	Blend 3	Blend 4	Blend 5
Copper	0	10	30	50	70
Nickel	100	90	70	50	30

Copper and nickel have a positive enthalpy of mixing and issues of immiscibility [20]. To absolutely ensure homogeneity within the deposit, the power parameters were altered from the preliminary studies. A pulse-width-modulated laser power was implemented during these depositions. The peak power was set at 1kW, and, the operating frequency was set to 250 Hz. The energy input was varied by changing the duty cycle. The first 4 layers of each of the deposits were fabricated at a 1kW power and a 100% duty cycle. This ensured a flaw-free bonding between the deposit and the substrate. Over the course of the next 4 layers, the power was brought down by gradually changing the duty cycle to 43%. The remainder of the deposit was carried out at a constant duty cycle of 43%. The duty cycle of 43%, was initially evaluated to be optimal for depositing all blends of powder. The pulsed implementation oscillates the melt pool and is thereby expected to promote mixing. The high power was expected to result in high cooling rates and also overcome the positive enthalpy of mixing. These depositions were used to fabricate 40mm long and 6mm tall thin-wall structures (single melt pool thickness). This implementation also facilitated the successful fabrication of the required thin wall geometry.

Optical microstructure images from the Figure 10, reveal a dendritic microstructure in all the deposits. With increasing copper content, coarsening of dendrites can be observed in the microstructure. This can be attributed to the increasing superheat in the melt pool. As the copper content is increased the solidus/liquidus temperature decreases. By using the same power parameters for all blends, excess heat input can be expected for the blends with higher copper content. To study the impact of energy input, the scan speed was varied. Scan speeds of 500mm/min and 600mm/min with the same power parameters were used to fabricate the 5 blends of powder listed in Table 4. Secondary Dendrite Arm Spacing (SDAS) was calculated to quantify the impact of process parameters on solidification (see Figure 11).

At constant power, lowering scan speed is expected to increase the energy density. This would lead to an increase in superheat, and, consequently, a slower solidification rate can be expected. This is expected to be noticed by an increase in SDAS values. The mean SDAS measurements in Figure 11 suggest slower cooling rates at lower scan speed. The mean values drop with increasing scan speed, however, due to wide standard deviations, no statistically significant difference was found between the measurements at different scan speeds. The wide standard deviations can be attributed to anisotropy caused in thin-wall deposits [21].

Miniature tensile specimens fabricated from the above deposits were tested to quantify their mechanical properties. A total of 8 specimens were cut per each blend and parameter set. Therefore, a total of 80 specimens were prepared from the 5 blends and 2 parameter sets. These specimens were hand ground up to 600 grit to remove any surface imperfections resulting from the EDM finish. Upon testing these 80 specimens, 73 valid measurements were obtained. The data gathered from these tests was represented as box and whisker plots as shown in Figure 12. Box and whisker plots are a convenient way of graphically representing variability in data. The box represents the 1st and 3rd quartiles of the data, the horizontal line in the box represents the median (2nd quartile), the 'X'

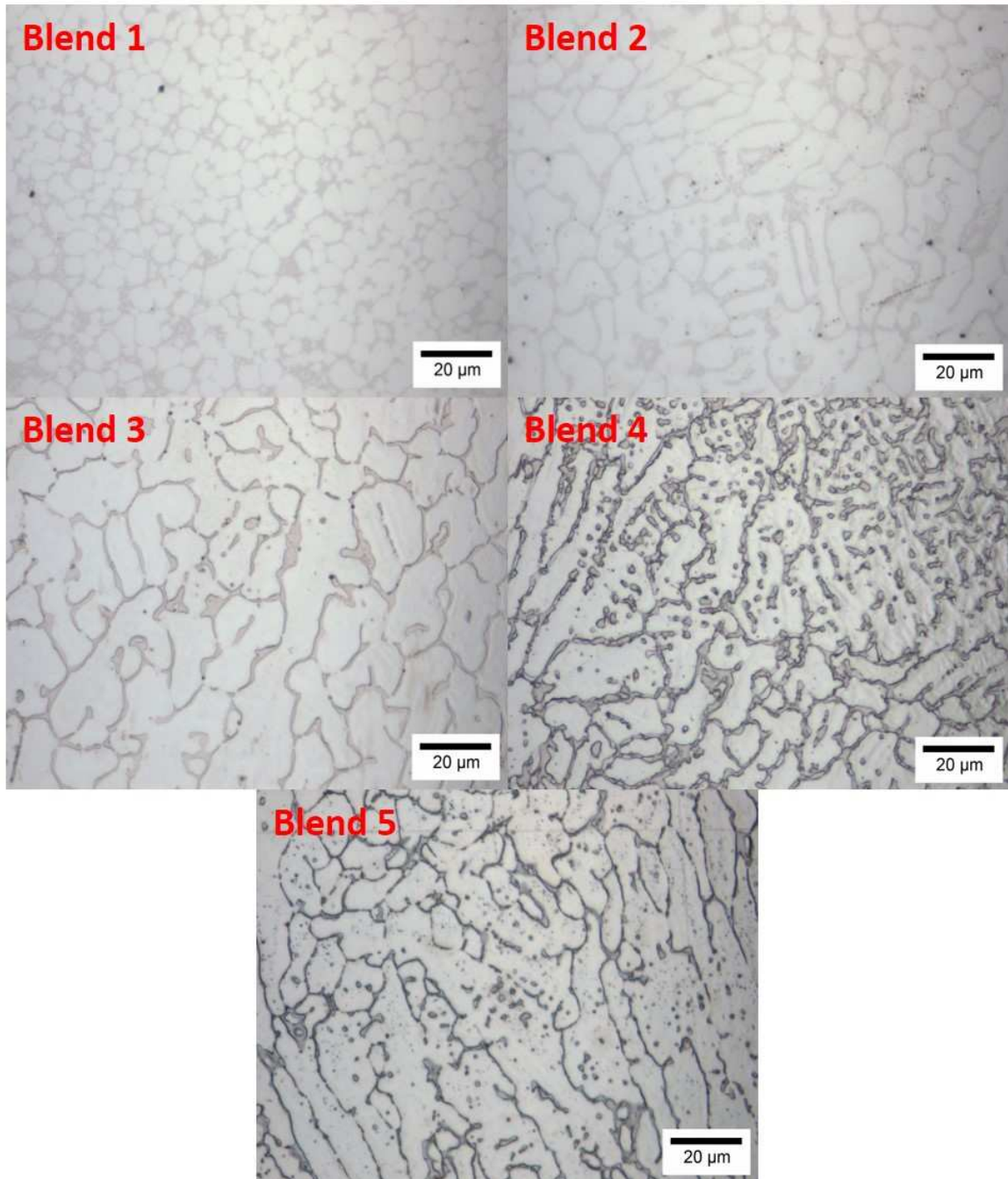


Figure 10. Optical micrographs of the as-deposited microstructure (etched using 70% vol. nitric acid) using powder blends listed in Table 4. The dendritic phase in the micrographs is the copper-nickel solid solution and the matrix is nickel boride.

mark represents the mean, and the vertical lines (whiskers) represent the minimum and maximum values of the data. Like SDAS measurements, a wide variation was noticed

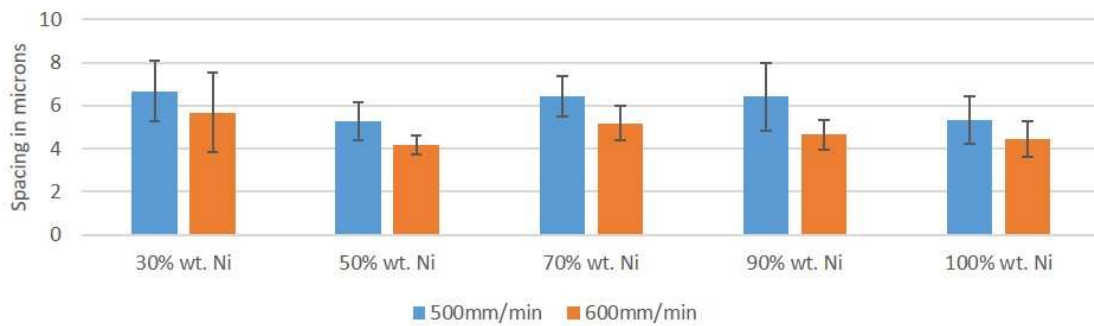


Figure 11. Secondary dendrite arm spacing measurements with one standard deviation error bars for all 5 blends under varying scan speed.

in the tensile property values as well. This variability can be attributed to the anisotropy caused by the directional solidification occurring during thin-wall fabrication. The gage length of the tensile specimens was along the length of the deposits. It is possible that the plane of maximum shear stress was aligned with the weaker sections of the material causing early failure. However, the trends in median values of the property estimates agree with the commercially available alloys. A rise in strength is seen with the increase in copper due to solid solution strengthening. The ductility of the material was also noticed to improve with the addition of copper. The variability in ultimate strength values seems to have been influenced by the change in scan speed. Especially for the case of 70 and 90 %wt. nickel. With slower scan speeds the variation in strength and ductility was seen to decrease.

The Fracture surface of the broken tensile samples was examined to identify the failure mechanism of the different compositions. SEM micrographs of the fracture surfaces are shown in Figure 13. These images indicate a change in fracture mechanism from transgranular to ductile with an increase in copper content. This suggests the material changes from brittle to ductile upon addition of copper. This change is also supported by the increasing values of maximum strain obtained from tensile testing.

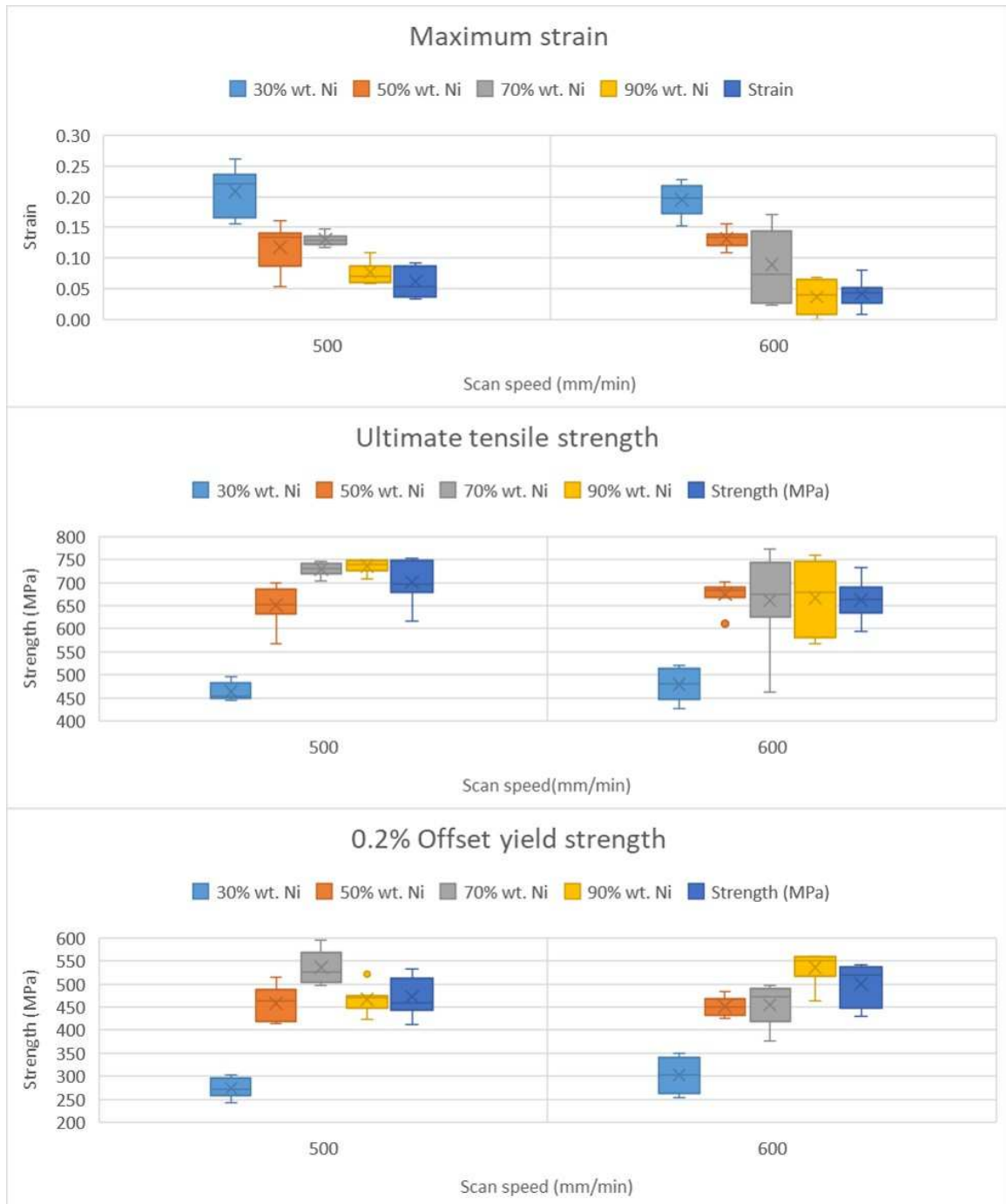


Figure 12. Box plot charts of mechanical properties gathered from miniature tensile testing. The mean (X) and median (-) values indicate a rise in ductility and drop in strength with increasing copper.

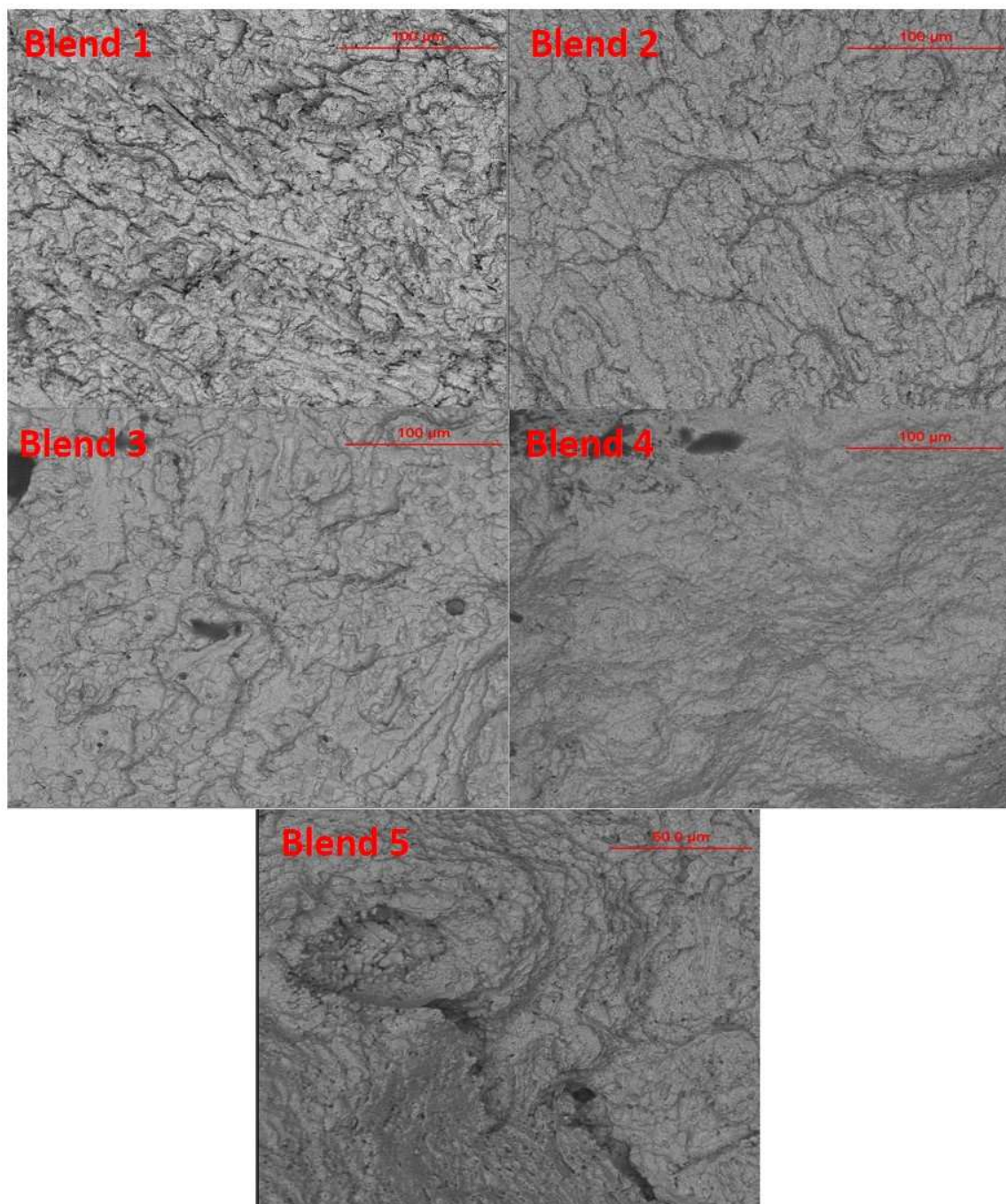


Figure 13. The fracture surfaces of miniature tensile samples made from blends listed in Table 4.

4. CONCLUSIONS

The current study involved testing the feasibility of fabricating copper-nickel alloys from blended powders. Elemental sources and sources with high percentage content of nickel were used as the precursor materials for the study. The main conclusions from the study were

- Depositing blends of elemental copper and elemental nickel powders produced solid solutions of copper-nickel alloys. This was corroborated by the XRD and metallography
- Deposits made from elemental nickel contained a significant amount of porosity. The porosity was constituted by gas (spherical pores) and shrinkage (irregular) pores
- Porosity was not avoidable by changing process parameters or adding chromium for gettering purposes
- Delero-22, a nickel-rich alloy was found to be a viable replacement for the elemental nickel powder. The silicon and boron alloy additions improved the fluidity and resulted in a substantial removal of porosity
- Unlike the material made from elemental blends, deposits made from elemental copper and Delero-22 alloy blends had two phases. This observation was corroborated by, XRD, metallography, and hardness testing. The microstructure was found to be made up of the copper-nickel solid solution and Ni_3B phases
- Blends of elemental copper and Delero-22 alloy were prepared to match commercially available copper-nickel alloys. Thin wall deposits made from these blends were sectioned to prepare miniature tensile samples.

- Homogenous microstructure was obtained in deposits made from all blends of copper-Delero-22 alloys. Solid solution strengthening was observed with increasing copper. Ductility was also observed with an increase in copper content
- The fracture mechanism changed from transgranular to ductile fracture with the addition of copper. This implies a change in material from being brittle to ductile

ACKNOWLEDGEMENTS

This work was funded through NASA EPSCoR program MO-NNX13AM99A, and NSF grants CMMI-1547042 and CMMI 1625736. The support from Intelligent Systems Center (ISC) and Material Research Center (MRC) in various stages of this study is also appreciated.

REFERENCES

- [1] Gary K Lewis and Eric Schlienger. Practical considerations and capabilities for laser assisted direct metal deposition. *Materials & Design*, 21(4):417–423, 2000.
- [2] Alberto Boschetto, Luana Bottini, and Francesco Veniali. Roughness modeling of AlSi10Mg parts fabricated by selective laser melting. *Journal of Materials Processing Technology*, 241:154–163, 2017.
- [3] Kai Feng, Yuan Chen, Pingshun Deng, Yuyan Li, Haixing Zhao, Fenggui Lu, Ruifeng Li, Jian Huang, and Zhuguo Li. Improved high-temperature hardness and wear resistance of Inconel 625 coatings fabricated by laser cladding. *Journal of Materials Processing Technology*, 243:82–91, 2017.
- [4] B Dutta and F H Froes. The Additive Manufacturing (AM) of titanium alloys. *Metal Powder Report*, 2017.
- [5] E L Doubrovski, E Y Tsai, D Dikovskiy, J M P Geraedts, H Herr, and N Oxman. Voxel-based fabrication through material property mapping: A design method for bitmap printing. *Computer-Aided Design*, 60:3–13, 2015.
- [6] Lei Yan, Xueyang Chen, Wei Li, Joseph Newkirk, and Frank Liou. Direct laser deposition of Ti-6Al-4V from elemental powder blends. *Rapid Prototyping Journal*, 22(5):810–816, 2016.

- [7] Pierre Muller, Pascal Mognol, and Jean-Yves Hascoet. Modeling and control of a direct laser powder deposition process for Functionally Graded Materials (FGM) parts manufacturing. *Journal of Materials Processing Technology*, 213(5):685–692, may 2013.
- [8] W. Li, L. Yan, S. Karnati, F. Liou, J. Newkirk, K.M.B. Taminger, and W.J. Seufzer. Ti-Fe intermetallics analysis and control in joining titanium alloy and stainless steel by Laser Metal Deposition. *Journal of Materials Processing Technology*, 242, 2017.
- [9] W. Li, S. Karnati, C. Kriewall, F. Liou, J. Newkirk, K.M. Brown Taminger, and W.J. Seufzer. Fabrication and characterization of a functionally graded material from Ti-6Al-4V to SS316 by laser metal deposition. *Additive Manufacturing*, 14, 2017.
- [10] Wei Li, Sreekar Karnati, Yunlu Zhang, and Frank Liou. Investigating and eliminating powder separation in pre-mixed powder supply for laser metal deposition process. *Journal of Materials Processing Technology*, 254:294–301, apr 2018.
- [11] Rodney Michael Clayton. *The use of elemental powder mixes in laser-based additive manufacturing*. PhD thesis, Missouri University of Science and Technology, 2013.
- [12] Xueyang Chen, Lei Yan, Wei Li, Frank Liou, and Joe Newkirk. Effect of Powder Particle Size on the Fabrication of Ti-6Al-4V using Direct Laser Metal Deposition from Elemental Powder Mixture, 2016.
- [13] Katrin I Schwendner, Rajarshi Banerjee, Peter C Collins, Craig A Brice, and Hamish L Fraser. Direct laser deposition of alloys from elemental powder blends. *Scripta Materialia*, 45(10):1123–1129, 2001.
- [14] Howard E Swanson, Eleanor Tatge, and States United. *Standard X-ray diffraction powder patterns. Vol. I, Data for 54 inorganic substances*. National Bureau of Standards, [Washington, D.C.], 1953.
- [15] M E Fraser, W K Lu, A E Hamielec, and R Murarka. Surface tension measurements on pure liquid iron and nickel by an oscillating drop technique. *Metallurgical Transactions*, 2(3):817–823, 1971.
- [16] P K Liao and K E Spear. B (Boron) Binary Alloy Phase Diagrams. *ASM Handbook*, Vol 3,:2.8–9.8, 1992.
- [17] P Nash and A Nash. Ni (Nickel) Binary Alloy Phase Diagrams, 1992.
- [18] Tsung-Yuan Kuo and Yong-Ding Lin. Effects of Different Shielding Gases and Power Waveforms on Penetration Characteristics and Porosity Formation in Laser Welding of Inconel 690 Alloy. *MATERIALS TRANSACTIONS*, 48(2):219–226, 2007.
- [19] B C Chakoumakos and M Paranthaman. Neutron powder diffraction study of the superconducting quaternary intermetallic compound YNi₂B₂C. *Physica C: Superconductivity*, 227(1):143–150, 1994.

- [20] M A Turchanin, P G Agraval, and A R Abdulov. Phase equilibria and thermodynamics of binary copper systems with 3d-metals. VI. Copper-nickel system. *Powder Metallurgy and Metal Ceramics*, 46(9):467–477, 2007.
- [21] Kai Zhang and Xiao Feng Shang. Microstructure and Properties of Thin-Wall Part by Laser Metal Deposition Shaping. *Materials Science Forum*, 675-677:563–566, 2011.

II. ON THE FEASIBILITY OF TAILORING COPPER-NICKEL FUNCTIONALLY GRADED MATERIALS FABRICATED THROUGH LASER METAL DEPOSITION

Sreekar Karnati^{*, a}, Frank F. Liou^a, Joseph W. Newkirk^b

^aDepartment of Mechanical & Aerospace Engineering

Missouri University of Science and Technology

Rolla, Missouri 65409-0050

^bDepartment of Materials Science & Engineering

Missouri University of Science and Technology

Rolla, Missouri 65409-0050

*Corresponding author, Tel: 573-341-4603, Fax: 573-341-4115

Email: skw92@mst.edu

ABSTRACT

In this study, pulse width modulation of laser power was identified as a feasible means for varying chemical gradient in copper-nickel graded materials. Graded material deposits of 70%wt. copper-30%wt. nickel on 100%wt. nickel and vice versa were deposited and characterized. The 70/30 copper-nickel wt. ratio in the feedstock powder was achieved through blending elemental copper and Delero-22 alloy. At the dissimilar material interface over the course of 4 layers, the duty cycle of power was ramped down from a high value to optimized deposition conditions. This change was theorized to influence the remelting and deposition height and in extension vary the chemistry gradient. EDS analysis showed significant differences in the span and nature of chemistry gradient with varying duty cycle. These observations were also supported by the variation in microhardness values across the interface. The influence of different chemistry gradients on tensile performance was

observed through mini-tensile testing coupled with digital image correlation (DIC). The strain fields from DIC analysis showed variations in strain for different chemistry gradients. The strength measurements from these specimens were also different for different chemistry gradients. The site of failure was observed to always occur within the copper-rich region.

Keywords: Laser metal deposition; functionally graded materials; blended elemental powders; digital image correlation; miniature tensile testing; X-ray energy dispersive spectroscopy;

1. INTRODUCTION

Functionally Graded Materials (FGM), are monolithic inhomogeneous materials whose anisotropy is tailored per designer's definition. The concept of FGMs was first proposed by material scientists investigating novel means for fabricating thermal barrier materials [1]. Spatially varying material properties or material composition can be used to achieve such anisotropy. The design freedoms available through FGMs' provide scope for fabricating highly efficient multifunction parts. Theorization and fundamental research has been carried out to identify FGM systems for applications such as lightweight heat exchangers, rocket nozzles, long life bearings, high-performance turbine blades etc. [2, 3, 4, 5, 6]. Techniques such as plasma spraying [4], die compaction [7], powder metallurgy [8], slip casting [9], and additive manufacturing [10, 11, 12, 13, 14, 15] have been shown to be successful in fabricating FGMs'. While successful all of the above processes excluding additive manufacturing possess limited scope for attaining fine resolutions in grading material composition. Also, these techniques are often limited in their capability to fabricate complicated geometries. Additive Manufacturing (AM) has been proven to be a versatile and competent technique for fabricating complex geometries. The layer by layer build approach enables the feasibility for fabricating intricate and complicated shapes. Laser Metal

Deposition is an AM technique, which involves blowing the feed material into the melt pool while depositing in a layer by layer fashion. The localized delivery of the feed material in LMD provides the unique opportunity of tailoring composition within a component.

Most of the existing literature involving FGMs' and AM is limited to identifying viable material systems. The choice of materials is often driven by the interest of aerospace and automobile industry. Most of these chosen material compositions are primarily intended for production processes such as casting, welding, rolling, machining, forming etc. and are not customized for AM. Adding to that, incorporating such materials into FGMs' often leads to unforeseen situations. Compatibility from a metallurgical perspective though, i.e. a phase diagram with no possible formation of intermetallic compounds doesn't guarantee structural integrity post fabrication [10]. Mostly, these FGMs are complicated due to the issues of compatibility among the constituent elements [4, 10, 11, 12, 14, 16, 17]. In cases where the main elements of the alloys are compatible, probable incompatibility among the remaining alloying elements could potentially leave the FGM system susceptible to flaws and early failure. In FGMs' the grading of the composition is intended to selectively transition properties. The presence of alloying materials can also limit the minimum feasible resolution possible during such composition grading. Control over grading is crucial, as it can help alleviate stress issues arising from the difference in physical properties such as thermal expansion coefficient, crystal structure, lattice parameter etc. In LMD, the unique opportunity for varying feedstock on the fly makes it very appealing for fabrication of FGMs'. This feature can be exploited to achieve a controlled gradient within FGM's.

To create multifunctional, and multi-material components using LMD, planning should be performed for geometry, composition, and, thermal history. A voxel-based path plan, where each voxel represents the position, composition and the required process parameters to achieve it needs to be generated in advance [2, 18]. Particularly, in order to vary the chemical composition within the part, the composition of the feedstock needs to be varied during deposition. In LMD, this is typically achieved by swapping out powder as needed.

Custom tailoring of compositions of pre-alloyed powders, to meet the grading requirements is very expensive and often requires extensive infrastructure. The feasible and economical alternative would be to incorporate blended powders into the deposition process. Premixing of powders to required compositions [19, 20, 21, 22, 23, 24, 25] or mixing powder on-line by using a multi-powder feed system [5] can be adopted to implement varying composition. While blending powders creates the possibility for creating custom combinations, it is only a viable option for making significant changes to feedstock composition. Creating blended feedstocks to produce grading at fine levels of composition is counterproductive. Also, demanding deposition of several blended powder feedstocks to produce a required grading schema could substantially increase the volume of the graded material component.

In this study, the authors theorize varying laser parameters could be a potential means to attaining control over grading at a finer scale. The feasibility of using pulse width modulation for manipulating laser power to achieve different chemical gradients in LMD is presented. This study was performed on copper-nickel FGMs'. The influence of varying chemistry on hardness and tensile performance was also investigated.

2. MATERIALS AND METHODS

The LMD system used in the current study consisted of a 1kW fiber laser from IPG Photonics. The operating wavelength of the laser was 1064nm. A spot size of 2mm was used during deposition. Along with it, a custom built 3-axis CNC system was used for facilitating motion during deposition. A Baystate model 1200 powder feeder was used for feeding powder during deposition. A schematic drawing of the deposition system is shown in Figure 1. An edge nozzle setup was used to feed the powder into the melt pool. Argon gas was used to transport the powder and also shield the deposition process from oxidation. The graded material deposits were fabricated by making a pre-deposit of the first material as a thin-wall structure followed by the deposition of the second material also as a

thin-wall structure on top of the pre-deposit. This lead to the grading of composition across the height of the thin-wall deposit. The thin-wall structures were made to a single melt pool thickness i.e. 2mm thick nominal.

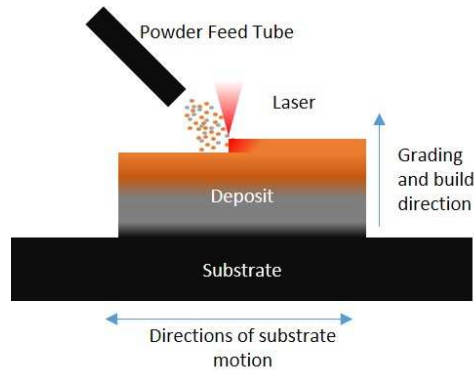


Figure 1. A schematic representation of the LMD deposition process used in the study. The gradient in the deposit illustrates grading within the deposit, the different color in powder particles is used to represent blended powder feedstock.

The graded material deposits in this study were made from -100/+325 mesh gas atomized powders of elemental copper and Delero-22 alloy. The 99.9% pure copper powder was procured from Oerlikon Metco and the Delero-22 powder was procured from Kennametal Stellite. Delero-22 is a nickel-silicon-boron alloy. The composition of this alloy is listed in Table 1. The boron and silicon in the alloy are expected to improve the fluidity of the material during deposition. At the current levels, silicon is completely soluble in nickel. However, the boron reacts with nickel and produces nickel borides which improve the hardness of the material. This alloy is primarily used for thermal spraying applications however, it exhibits excellent compatibility with LMD. The compositions of the blended feedstock powders used in the current study are shown in Table 2. These two compositions were classified as nickel-rich and copper-rich with a relative nickel/copper weight ratio of 100/0 and 30/70 respectively. Hereon they will be referred to as 100/0 and 30/70.

Table 1. The composition of Delero-22 alloy in weight percentage.

Element	Silicon	Boron	Nickel
Weight %	2.5	1.4	Balance

Table 2. Compositions of blended powder feedstocks used in the study.

Powder type	Elemental Cu (%wt.)	Delero-22 alloy (%wt.)	Ni/Cu wt. ratio
Nickel-rich	0	100	100/0
Copper-rich	29.13	70.83	30/70

Graded material deposits from both nickel-rich (100/0) to copper-rich (30/70) and copper-rich (30/70) to nickel-rich (100/0) compositions were performed and characterized under the current study. All the depositions were carried out at a scan speed of 500mm/min and a powder feed rate of 1.5 rev./min. Peak power of 1kW and a duty cycle of 43% at 500 Hz modulation frequency were used for all the deposits. These parameters were chosen from a preliminary optimization study aimed at getting good quality single bead deposits of Delero-22 alloy. A layer thickness of 0.15mm was used for path planning. These deposits were performed on 50mmx12.5mmx6.35mm AISI 304 stainless steel substrates. In the case every deposit, the first material was deposited for 40 layers. This was done to ensure no constituent elements from the substrate would interfere with the gradient under this study.

In a PWM implementation of laser power, varying duty cycle varies the total on-time of the laser. However, the peak power is held constant. Therefore varying the duty cycle varies the net energy input during deposition. While the melt pool width/diameter is expected to be relatively the same, varying duty cycle should vary the depths of the melt pool. The width is expected to be the same since the power/beam intensity is the same for all the duty cycles [26]. This variation in melt pool dimensions was theorized to vary the remelting between successive layers and the volume of material deposited in every layer. At the dissimilar material interface, this variation in melt pool attributes is expected to achieve

different grading schemes. To investigate this hypothesis, three sets of depositions with varying duty cycles were performed. The duty cycle was only varied in the initial 4 layers of deposition at the dissimilar material interface.

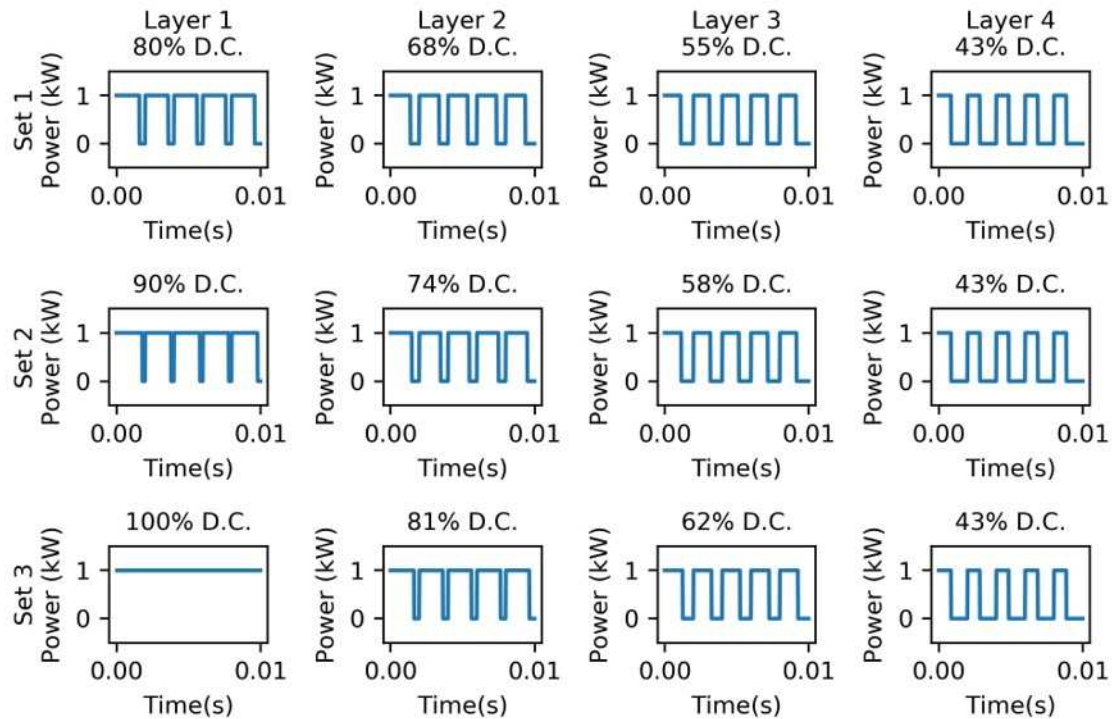


Figure 2. Power and Duty Cycle (D.C.) values used in the initial 4 layers at the dissimilar material interface while fabricating the copper-nickel FGM thin-wall deposits.

The D.C. variation shown in Figure 2 was used for both 100/0 on 30/70 and 30/70 on 100/0 deposits. These deposits were then sectioned and processed for various analyses. Longitudinal sections of these deposits were used for both chemistry and hardness analysis. The chemical analysis was done through standard-less X-ray Energy Dispersive Spectroscopy (EDS) on ASPEX-PICA 1020 SEM. The hardness testing was on a Struers Duramin hardness testing machine.

These deposits were also sectioned for preparing miniature tensile test specimens [25]. The dimensions of the specimens are shown in Figure 3. These specimens were cut with the gage length along the grading direction. The specimens were tested at a constant

crosshead speed of 0.6mm/min. These tensile tests were imaged to perform Digital Image Correlation (DIC) analysis [25]. The DIC technique was used to estimate the evolution of the strain field on the miniature tensile specimens. This was used to realize the inhomogeneous strain development in the FGMs'.

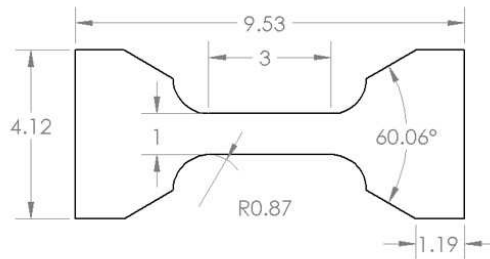


Figure 3. Dimensions of the miniature tensile test specimen; all the dimensions are in mm.

3. RESULTS AND DISCUSSION

3.1. DEPOSITION OF 100/0 AND 30/70 FEEDSTOCKS

Elemental copper has a very high thermal conductivity [27]. Also, it is highly reflective at the wavelength of the current laser [28]. This makes melting of elemental copper extremely challenging. However, in the current study, by blending copper and Delero-22 deposition was achieved. The Delero-22 powder in the powder mixture absorbs the laser to initiate and sustain the melt pool. This melt pool is then capable of melting the elemental copper powder. Upon melting the copper mixes with nickel and the overall reflectivity and thermal conductivity go down substantially while making the deposited material viable for processing through LMD. However, these reflectivity issues have been observed to impact the overall capture efficiency for the blended feedstocks. The 30/70 deposits were observed to be shorter in comparison to the 100/0 deposits. The same can be seen from the machined deposits shown in Figure 4.



Figure 4. Machined thin-wall deposits of solely nickel-rich 100/0 (left) and copper-rich 30/70 (right) with a significant difference in overall height for the same 40 layers of deposition.

Transverse sections of these deposits were sectioned and polished for X-Ray Diffraction (XRD) analysis. The XRD peak patterns from the 100/0 and 30/70 deposits are shown in Figure 5. In both cases, we see strong peaks of the copper-nickel FCC solid solution. The influence of adding copper can be seen from the peak shift from nickel to copper peak positions. Along with the FCC solid solution peaks, peaks corresponding to nickel boride (Ni_3B) were also observed. However, these peaks were absent in the 30/70 peak pattern. Although the peaks are absent we suspect the Ni_3B phase is probably below the detection limits of the XRD analysis. Further microscopy and EDS analyses were performed to investigate these claims.

Transverse cross sections of these deposits were cut, mount in Bakelite, ground, polished and etched for optical microscopy. The etching was carried out using a mixture of 60 ml HNO_3 and 40 ml DI water. The optical microscopy images of both 100/0 and 30/70 are shown in Figure 5. From these microstructure images, a relatively finer dendritic microstructure is seen in 100/0 deposits when compared to 30/70 deposit. In both cases, the microstructure is constituted of two phases. The dendritic phase is expected to be the nickel-copper-silicon solid solution and the inter-dendritic phase is expected to be nickel boride. Due to the lower melting point of nickel boride, it is expected to solidify last and is therefore expected to be the inter-dendritic phase. The coarsening of dendrites in the case of 30/70 could be attributed to the lower powder capture efficiency. Due to the low capture efficiency most of the energy is expected to be absorbed by deposit, thereby

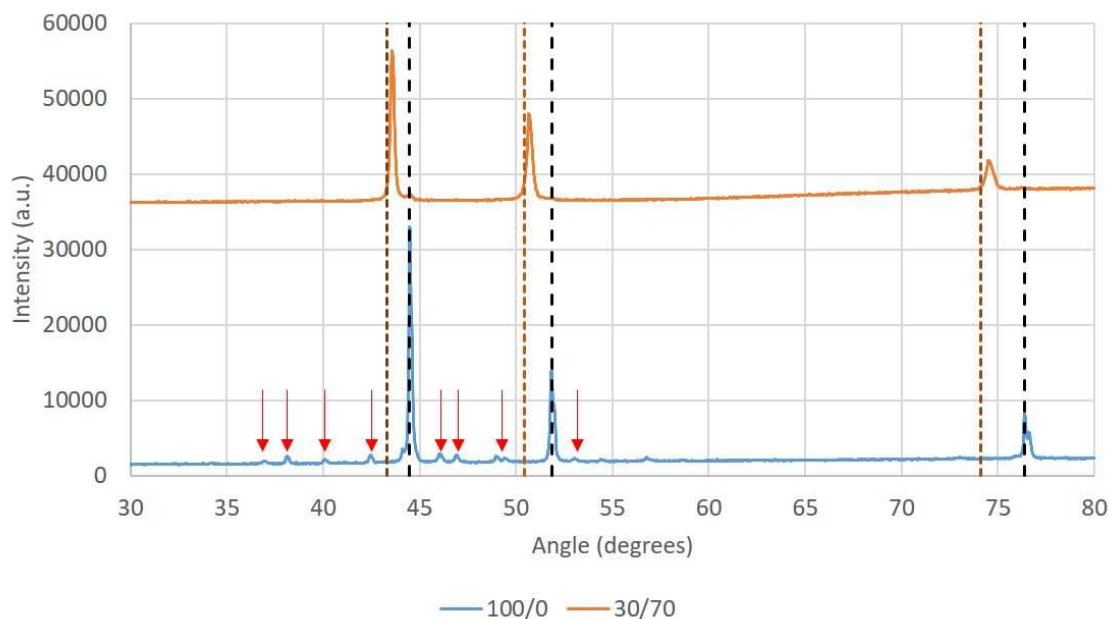


Figure 5. Peak patterns of 100/0 and 30/70 from X-ray Diffraction analysis. The black dotted line represents the peak pattern of elemental nickel and the copper-red dotted line represents the peak pattern of elemental copper. The red arrows indicate the peak positions of nickel boride phase (Ni_3B).

more remelting between successive layers is anticipated. However, validating these claims was not feasible since there were no markers to identify layer boundaries in the 30/70 microstructure. Although a repetitive coarsened dendrite band pattern was observed in the 100/0 deposits. This pattern is expected to be a signature of the layer by layer deposition. Similar microstructural features were reported in the dendritic microstructure of aluminum deposits [29] and 17-4PH steel deposits [30]. The formation of these coarsened dendrite bands was attributed to remelting occurring between layers during LMD.

At relatively higher magnifications, apart from the copper-nickel solid solution and nickel boride phases, the third phase of inclusions was also observed. These inclusions were suspected to be silica particles. These particles were mostly situated in the inter-dendritic phase. A bright field optical microscope image with Nomarski interference contrast is shown in Figure 7. The dark phase in the image is suspected to be silica inclusions.

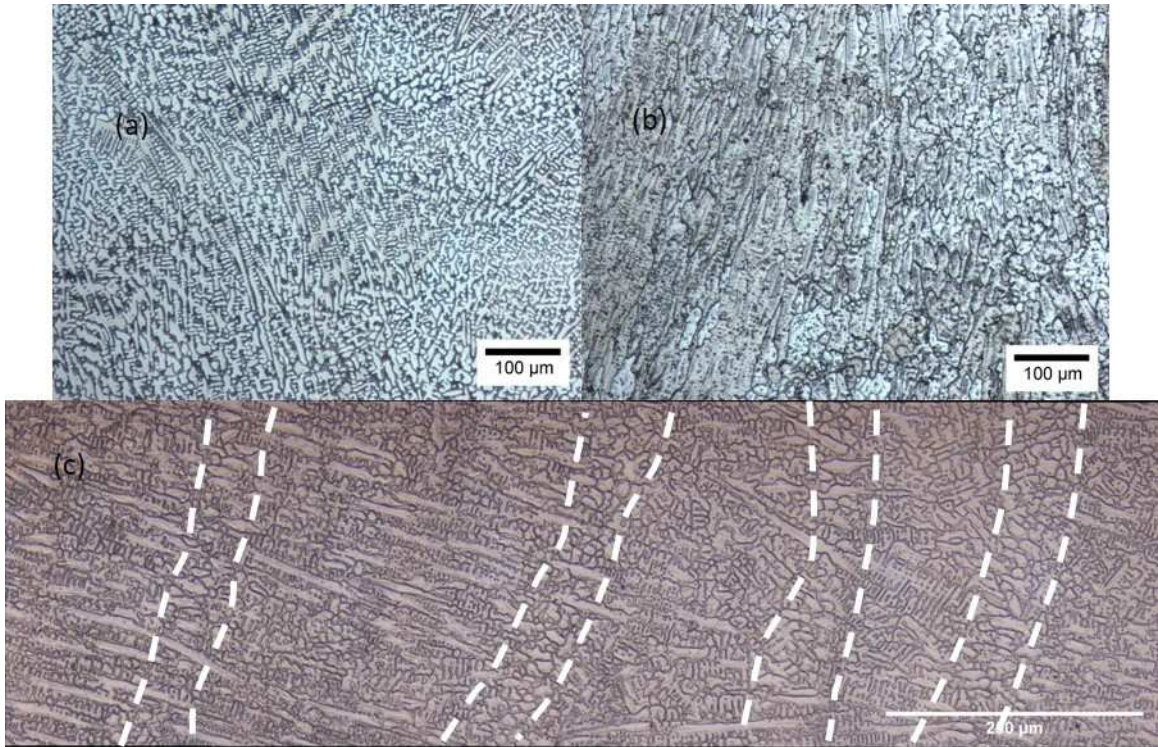


Figure 6. Optical microscope images of (a) 100/0 nickel-rich deposit and (b) 30/70 copper-rich deposit (c) bands of coarsened dendrites on 100/0 deposits, suspected to be originating from remelting during successive layer by layer deposition.

In order to validate the presence of the nickel boride as the inter-dendritic phase and also investigate its presence in 30/70 deposit, standard-less EDS analysis was performed. A line scan EDS analysis across the dendritic and inter-dendritic phases is shown in Figure 8. Boron is a lower atomic number element and is therefore not easily detectable using the SEM. However, the presence of this phase was realized through the variation in copper-nickel content across the phases. The complimentary rise and drops seen in the counts of copper and nickel are attributed to the absence of copper and the presence of nickel boride as the inter-dendritic phase. EDS analysis also revealed as-deposited compositions within 4%wt. difference from as-blended compositions.

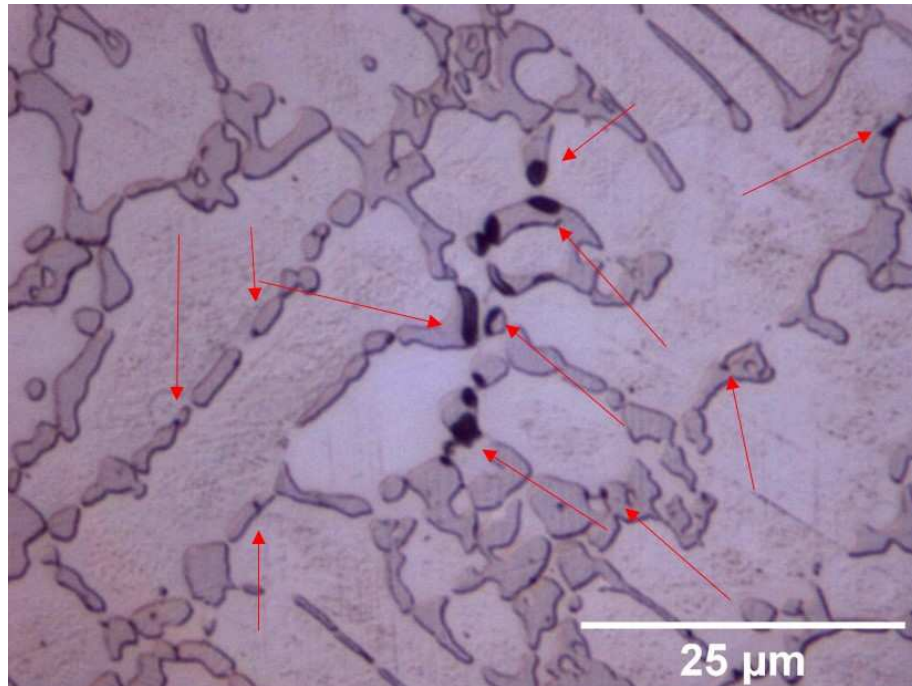


Figure 7. Optical microscope image of 100/0 nickel-rich deposit taken using Nomarski interference contrast. The elevated inter-dendritic phase is nickel boride whereas the dendritic phase is the nickel phase. The dark phase particles (annotated by the red arrows) are suspected to be silica inclusions.

3.2. DISSIMILAR GRADED MATERIAL DEPOSITION

FGM deposits of 100/0 over 30/70 and vice versa were deposited on the AISI 304 substrates. In each case the first material was deposited for 40 layers, then the powder was swapped out to deposit the second material. At the dissimilar material interface, the duty cycle of power was ramped down from a higher value to optimized conditions. This ramp down was performed as three sets (see Figure 2) and was repeated for 100/0 on 30/70 and 30/70 on 100/0.

Typically before starting deposition, preheating is performed by running the laser without powder. This is intended to reduce the temperature gradient during the actual deposition. This aids in attaining good bonding with the substrate and is, therefore, good practice in situations where this bond is of significance. In this study this preheat scan was

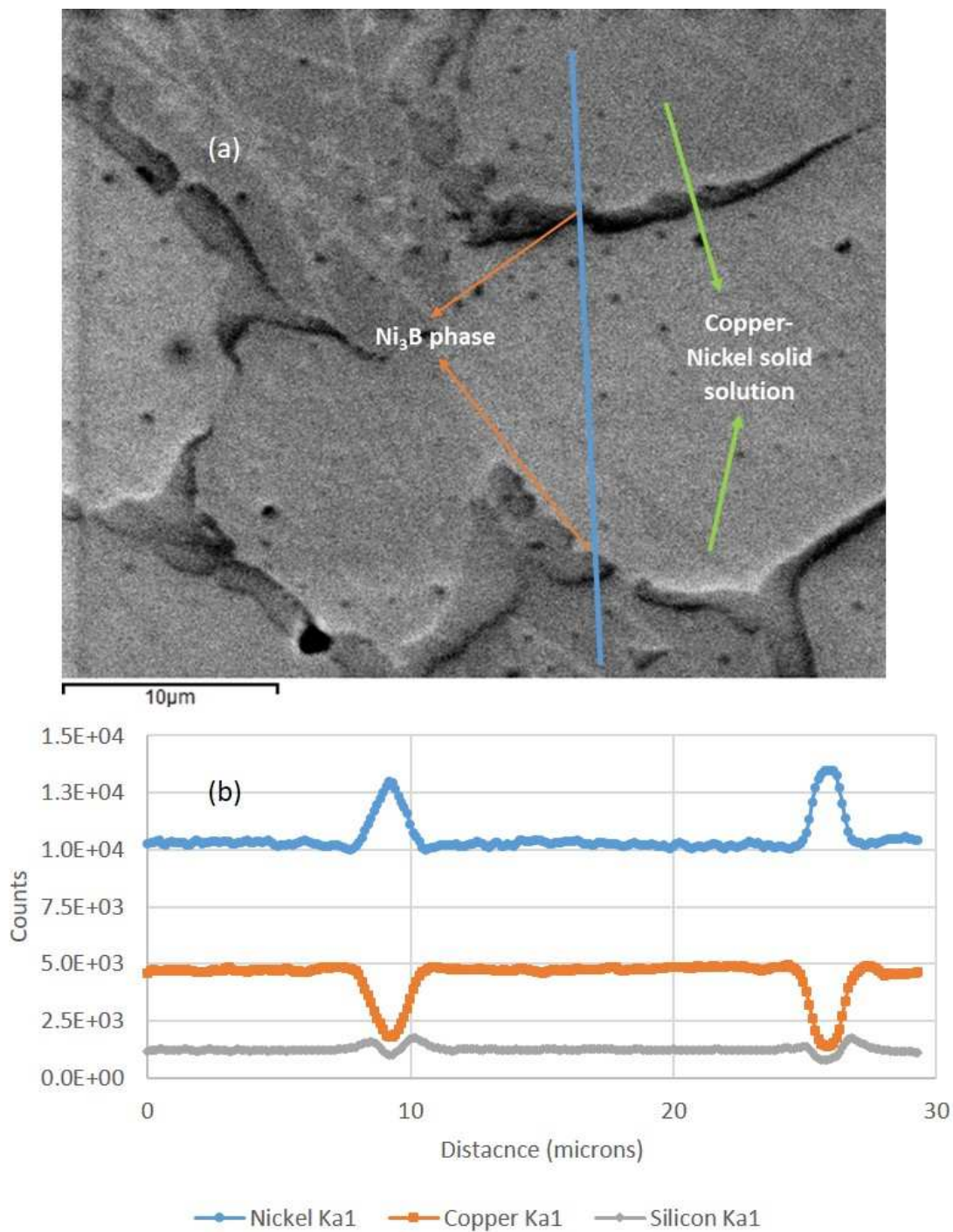


Figure 8. EDS line scan analysis across the dendritic and inter-dendritic phases on an as-polished 30/70 deposit. The complimentary rise and drop in copper and nickel counts are indicative of the presence of nickel boride as the inter-dendritic phase.

not performed, starting deposition with the optimized conditions might lead to insufficient bonding or flawed start in a deposition. However, starting at a higher duty cycle enables one to lower the temperature gradient and attain a flaw-free start. Although, the higher duty cycle could produce larger melt pools and different volumes deposited material. In this study, this phenomenon was leveraged to alter grading in the deposited material. At the dissimilar material interface, different starting values of duty cycles were theorized to create differences in dilution and therefore differences in the grading schemes were expected. A graded material deposit of 30/70 on 100/0 with the set 3 (see Figure 2) duty cycle ramp down is shown in Figure 9.



Figure 9. Copper-nickel FGM deposit fabricated with 100/0 as the pre-deposit and 30/70 as the second deposit. Set 3 duty cycle ramp down parameter were used at the dissimilar material interface.

In order to realize the chemical gradient, transverse and longitudinal sections of these deposits were prepared for optical microscopy, hardness testing, and EDS analysis. The initiation of grading i.e. the dissimilar material interface was optically distinguishable due to the difference in reflectivity of polished surfaces. This difference was also apparent from oxide scale, a clear demarcation between the two dissimilar materials was observed when cut using a wire-EDM. The transition in microstructure can be seen from Figure 10. A clear transition in the microstructure, from relatively finer two-phase dendritic microstructure to a coarser two-phase microstructure, can be seen.

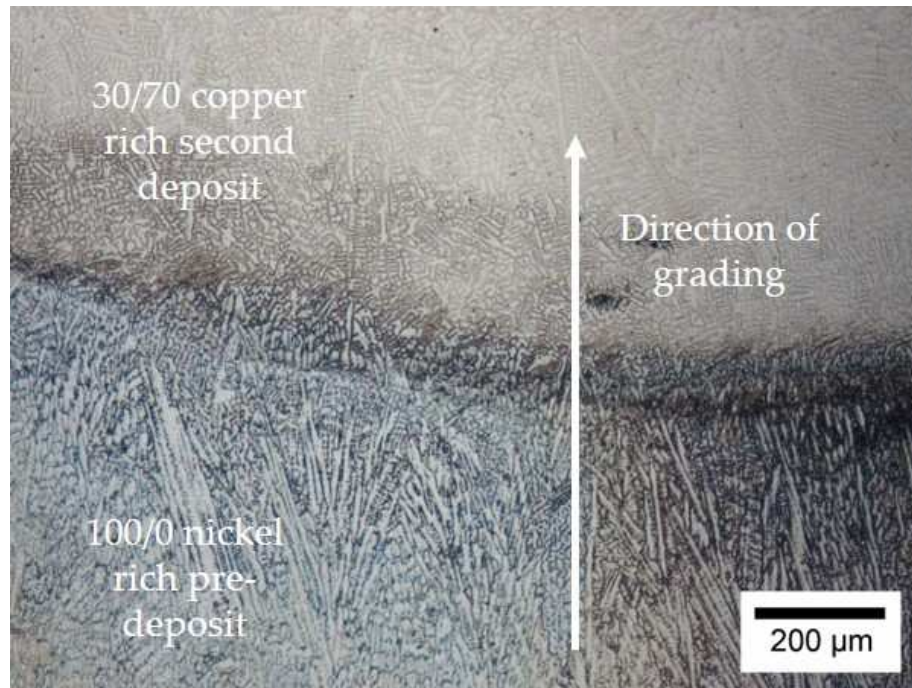


Figure 10. Optical microscope image of the dissimilar material interface on a graded material deposit fabricated by depositing 30/70 on 100/0 using the set 1 (see Figure 2) duty cycle ramp down.

Line scan EDS analysis was performed to realize the variation in chemistry across the height of the deposit. The nickel, copper and silicon content was monitored to realize the trend and nature of grading. The line scan plots are shown in Figure 11 and Figure 12. The x-axis of these plots traverses along the height from the pre-deposit on the left to the second deposit in the right on the axis.

The differences in the chemistry gradient with changing duty cycle and deposition combinations are apparent from Figure 11 and Figure 12. From Figure 11, from set 1 to set 3, the transition length was observed to increase and intermediate steps were also observed to occur. From set 2 to set 3 the length of this intermediate step was also seen to increase. On the other hand, from Figure 12, the length of the transition region was observed to decrease. Similar to the scans in Figure 11, intermediate steps in composition were also seen in the plots in Figure 12. However, these steps were noticed to decrease in length and

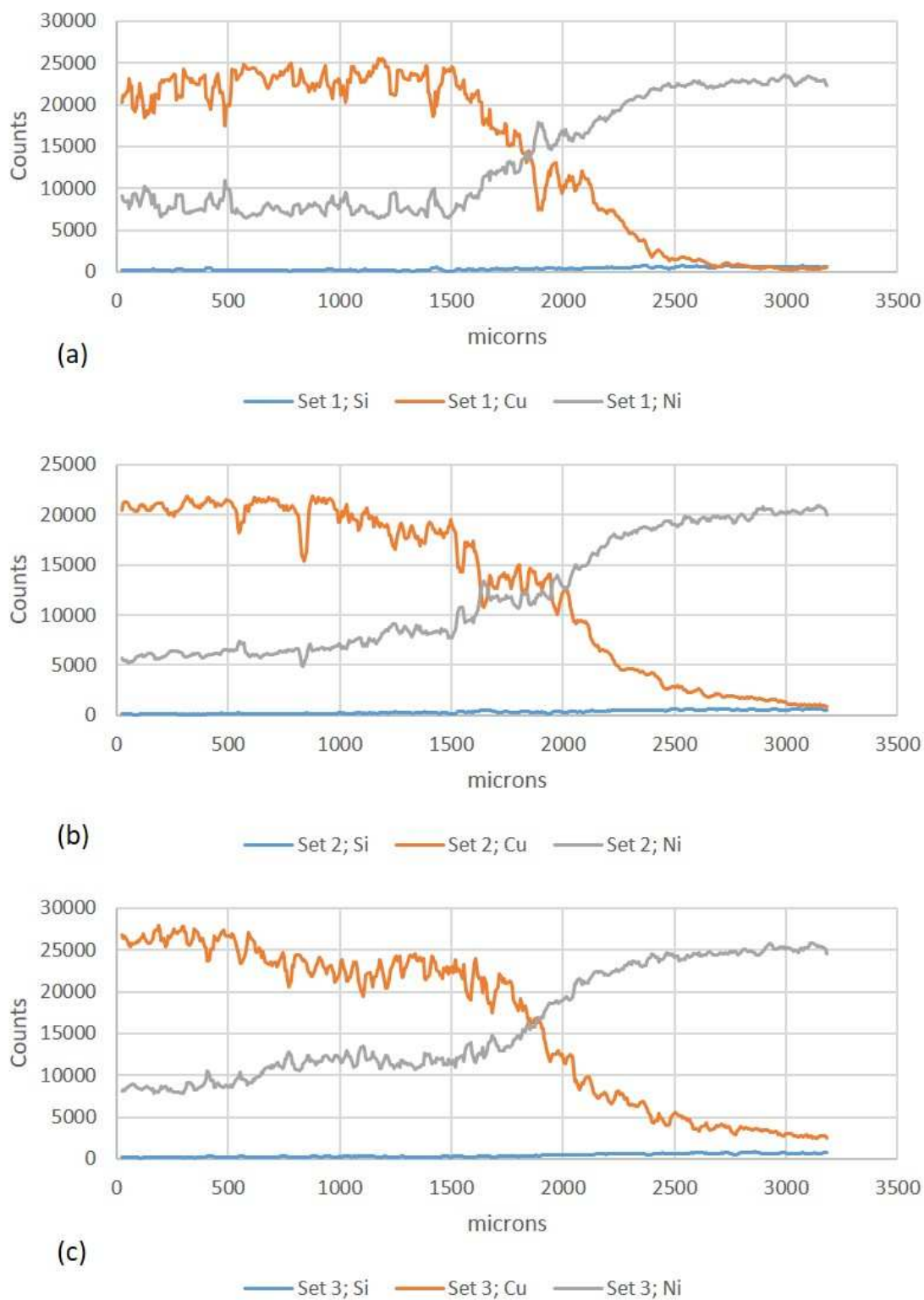


Figure 11. EDS line scan analyses across dissimilar graded material interfaces for the three sets, (a) set 1, (b) set2 and (c) set 3, of duty cycle ramp downs (see Figure 2) when 100/0 nickel-rich deposit was fabricated on 30/70 copper-rich pre-deposit.

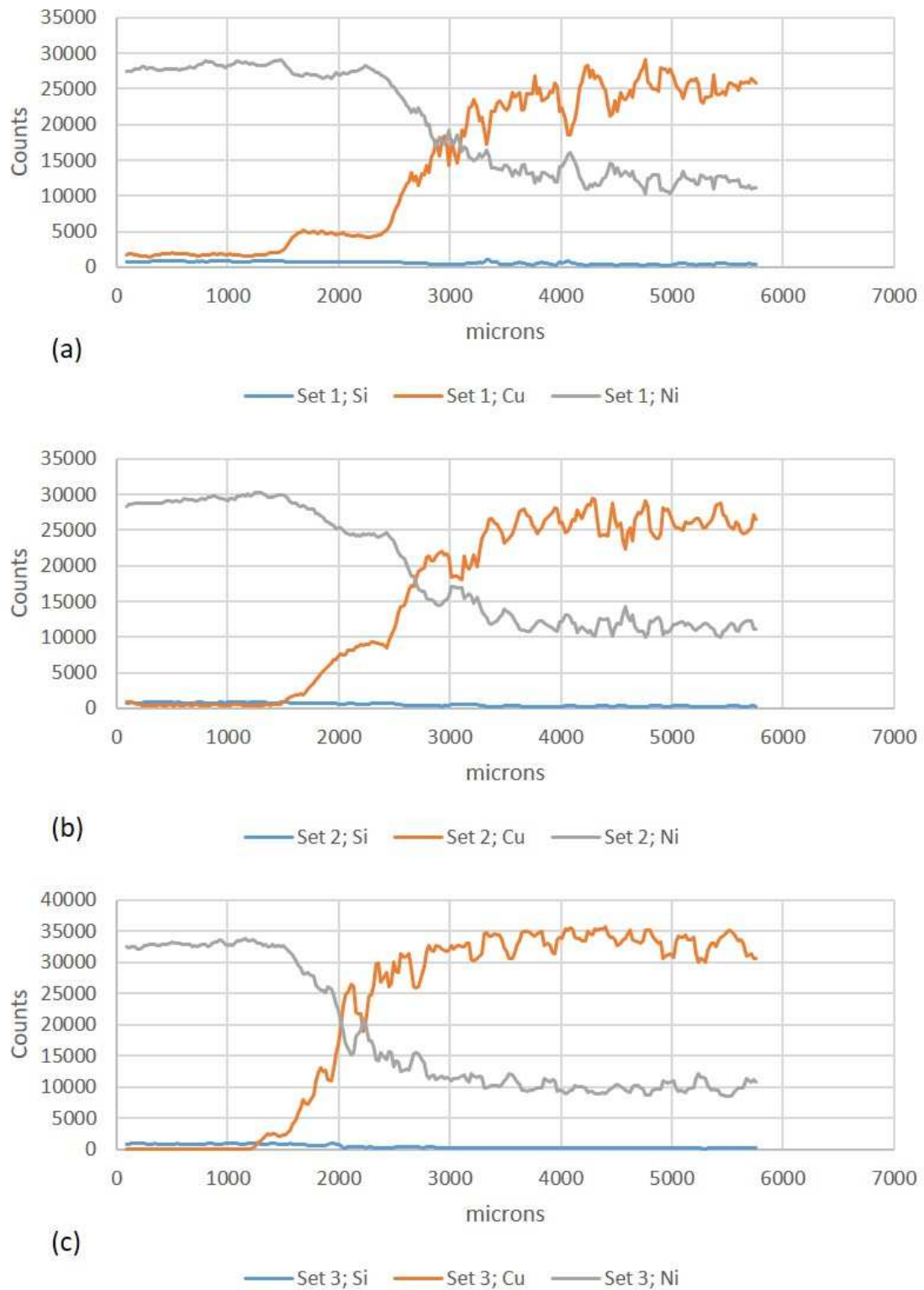


Figure 12. EDS line scan analyses across dissimilar graded material interfaces for the three sets, (a) set 1, (b) set2 and (c) set 3, of duty cycle ramp downs (see Figure 2) when 30/70 copper-rich deposit was fabricated on 100/0 nickel-rich pre-deposit.

disappear with increasing duty cycle. Also in all of the above line scans complimentary rise/drop can be seen in copper and nickel count signals, this is attributed to the presence of the nickel boride phase. This behavior is similar to the observations from the EDS line scan shown in Figure 8.

In order to better realize the differences among these deposits, the length of the chemical gradient from Figure 11 and Figure 12 was measured and plotted in Figure 13. In the case of 30/70 to 100/0 deposition, from set 1 to set 3, the length of the transition was observed to increase monotonically. From set 1 to set 3, this length was observed to more than double with increasing duty cycle. Whereas for 100/0 to 30/70 the length of the chemistry transition was observed to decrease. However, these values were still larger than the largest transition length seen in the case of 100/0 on 30/70 deposits. The scale of the drop in transition length was also not as substantial.

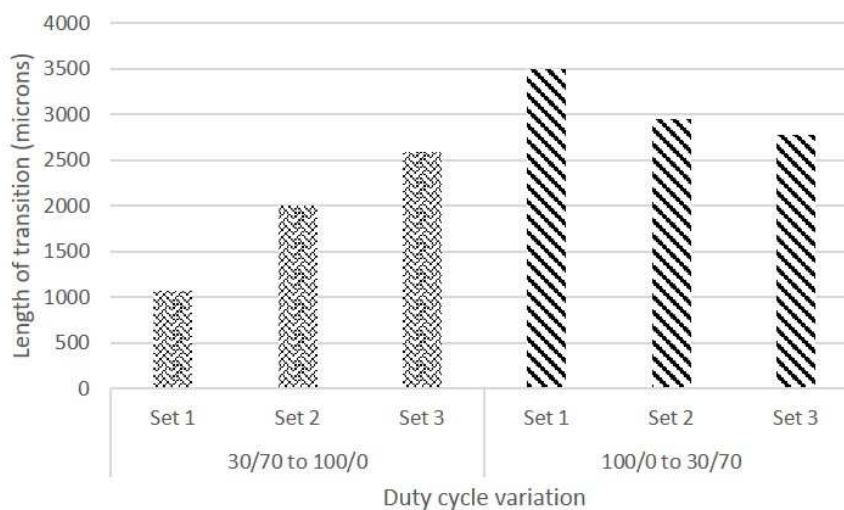


Figure 13. Length of the chemical gradient for the different cases of graded material deposition as measured from Figure 11 and Figure 12.

From set 1 to set 3, the initial values of the duty cycle were increased. This increase results in increasing energy input during deposition of the initial layers. This higher energy is expected to result in a larger melt pool depth and deposited volume. However, due to the ramp down of the duty cycle in successive layers, the remelting is expected to decrease

as the deposition progresses. This difference in remelting depth was theorized to create a gradual and tailorable gradient. Although, if the ramp down of the duty cycle is insufficient, the remelting could be significant enough to rewrite the gradient established in the previous layer. This phenomenon is better explained in the schematic diagram shown in Figure 14. This gradient is also expected to be influenced by the amount of newly deposited material end of every layer. Therefore the differences in capture efficiency of the 100/0 and 30/70 blended powder are expected to give different outcomes. From the line scan data in Figure 11, the occurrence of the intermediate step in transition in set 2 and set 3 implies gradient was preserved across successive layers of deposition. With increasing duty cycle more dilution is seen from the pre-deposit. However, the gradient is retained across layers. In the case of 30/70 on 100/0, Figure 12, with increasing duty cycle the remelting is expected to increase and the gradient was completely changed between successive layers of deposition. This difference is suspected to be a consequence of the difference in capture efficiency of the feedstock powders. To conclude, varying the duty cycle is a viable means for producing different chemistry gradients in this dissimilar graded material system.

In order to assess the influence of varying transition length on mechanical properties, hardness testing and tensile testing were performed. The hardness testing was performed on a Struers Duramin hardness tester. A load of 200gm and a dwell time of 5 seconds were used for measuring hardness. A series of indentations were performed along the height of the deposit to track the hardness variation with the changing chemistry of the deposit. The hardness data from the deposits is shown in Figure 15. The interface shown in Figure 10 was positioned as the center for the hardness analysis. The 30/70 deposits were observed to have to a significantly lower hardness in comparison to the 100/0 deposits. This steep difference can be used to realize the variation in chemistry. The drop/rise in hardness along the chemical gradient was observed to correlate well with the transition lengths measured from EDS analysis. The longest transition lengths as measured from EDS, i.e., set 1 for 100/0 to 30/70 and set 3 for 30/70 to 100/0 showed a very gradual change in hardness. The

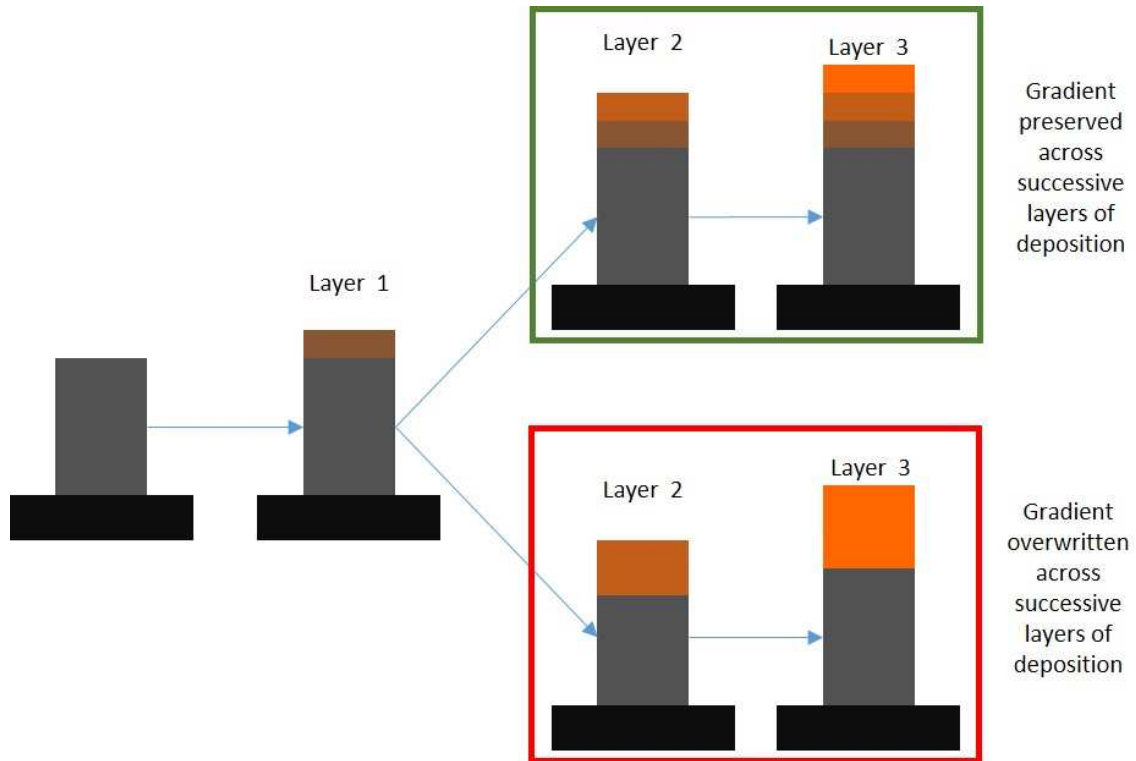


Figure 14. Schematic diagram of transverse sections of FGM deposits detailing the influence of remelting on the gradient development during dissimilar material deposition.

shortest transition lengths as measured from the EDS analysis, i.e., set 3 for 100/0 to 30/70 and set 1 for 30/70 to 100/0 showed a relatively steep change in hardness. Typically the hardness values are expected to correlate with the tensile strength properties. Assuming this holds in the current case, the 30/70 composition would be significantly weaker in comparison to the 100/0. The variation observed in the case of hardness can also be expected in the tensile properties. As seen from the hardness values with increasing copper content the strength should be decreasing. Due to the significant differences in strength, the failure should always occur in the 30/70 portion of the graded material. The deformation in the tensile specimens should also vary with composition. To investigate these claims tensile testing of miniature specimens coupled with DIC analysis was performed. These miniature tensile specimens were prepared with the interface seen in Figure 10 located at

approximately the center of the gage length. The gage length of these specimens was only 3mm so, it was possible that the entire transition length was not located within the gage length. This approach was adopted as it was easy to visually identify the interface. This enabled a reliable and repeatable method of locating the interface and preparing tensile specimens.

Since the difference in the transition lengths was significant for set 1 and set 3 duty cycle ramp downs for both 100/0 on 30/70 and 30/70 deposits, miniature tensile specimens were cut and tested from these deposits. The interface was located at the center for the gage length for all the specimens. The specimens were tested at a constant crosshead speed of 0.6mm/min. The tensile tests were video recorded with the camera oriented to capture the front view of the tensile testing. These videos were processed for DIC analysis and strain field estimation. A speckle pattern was necessary to create sufficient contrast for DIC analysis. The required speckled pattern was applied to all the specimens before tensile testing. The DIC estimated strain fields during the tensile testing post initiation of necking is shown in Figure 16.

From the strain fields shown in Figure 16, the inhomogeneity in strain along the gage length is recognizable. As anticipated from the hardness data, the failure was pushed into the weaker copper-containing region. Majority of the plastic deformation was limited to the portion of the gage length that was containing copper. Minimum to no deformation was observed in the 100/0 side of the deposit. The steep change in the strain field along the gage length is expected to be indicative of the start of the chemistry gradient. The site of failure was expected to differ depending on the length of the transition region and position of the start of the interface within the gage length. Among all of the specimens tested, the failure was always noticed to occur within the copper contained region. The exact chemistry at the site of failure initiation was difficult to pinpoint due to the inclined nature of the fracture site.

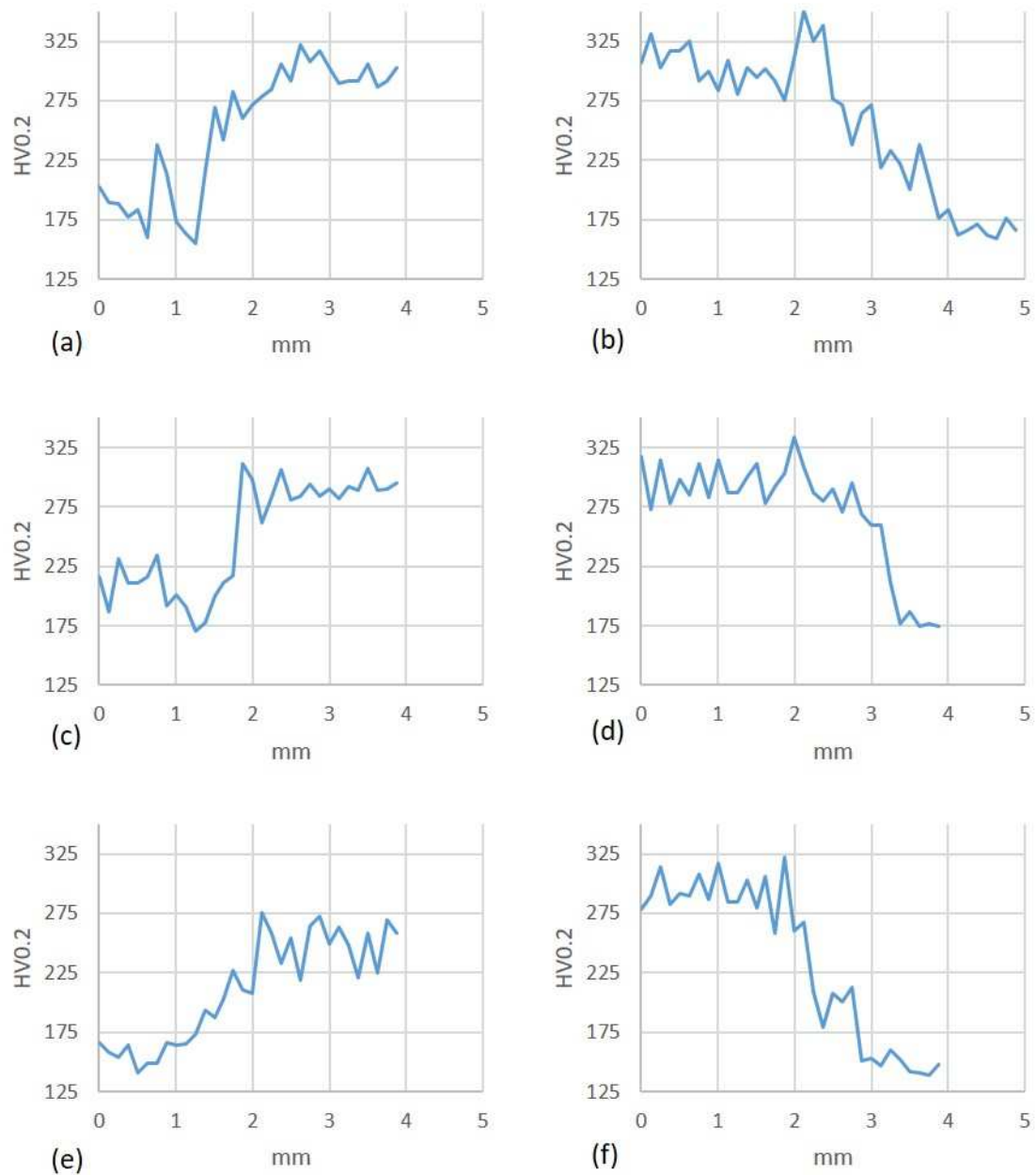


Figure 15. Variation in Vickers hardness values (HV0.2) along the height of the graded material deposits. (a), (c), and (e) are the hardness plots on set 1, set 2 and set 3 deposits of 100/0 on 30/70 respectively. (b), (d), and (f) are the are the hardness plots of set 1, set 2 and set 3 depositions of 30/70 on 100/0 respectively.

The strength and ductility values of tested specimens are shown in Figure 17. Since the start of the interface was located at the middle of the gage length, the transition region doesn't necessarily end within the gage length. The length of the transition region was

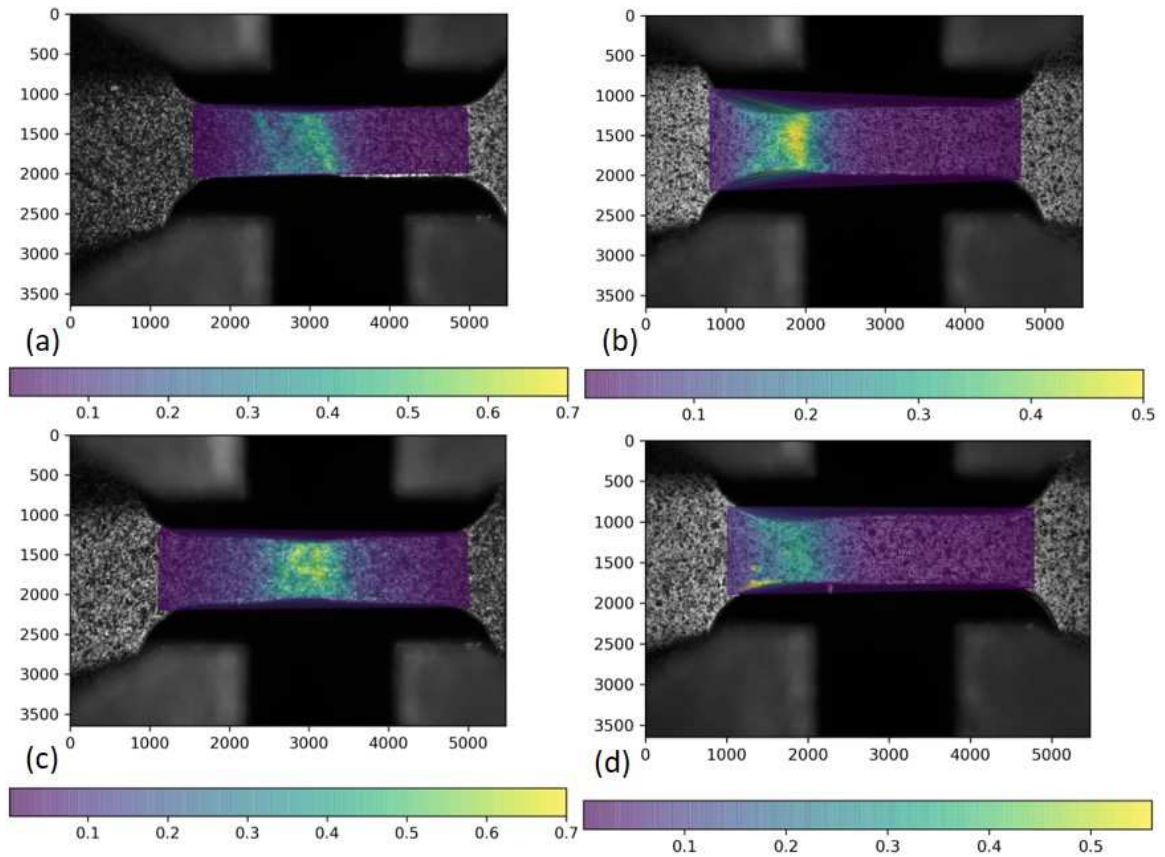


Figure 16. Strain fields calculated from gage length elongation values calculated from DIC analysis for (a) Set 1 100/0 on 30/70, (b) Set 1 30/70 on 100/70, (c) Set 3 100/0 on 30/70 and, (d) Set 3 30/70 on 100/0 deposits.

larger in the 30/70 on 100/0 deposits in comparison to 100/0 on 30/70 deposits. This implies a lower copper content in the 30/70 100/0 tensile specimens. This is reflected from the ultimate strength values. Lower copper content in these deposits is expected to have yield higher strengths.

While the difference in strengths pointed to chemistry differences, the influence of duty cycle wasn't as anticipated. For a given combination of pre-deposit and deposit, the change in transition length did not correlate with the strength variation. In both the cases, with increasing duty cycle the strength was seen to drop. Previously, silica inclusions were observed within the deposit (see Figure 7). With increasing the duty cycle, the population

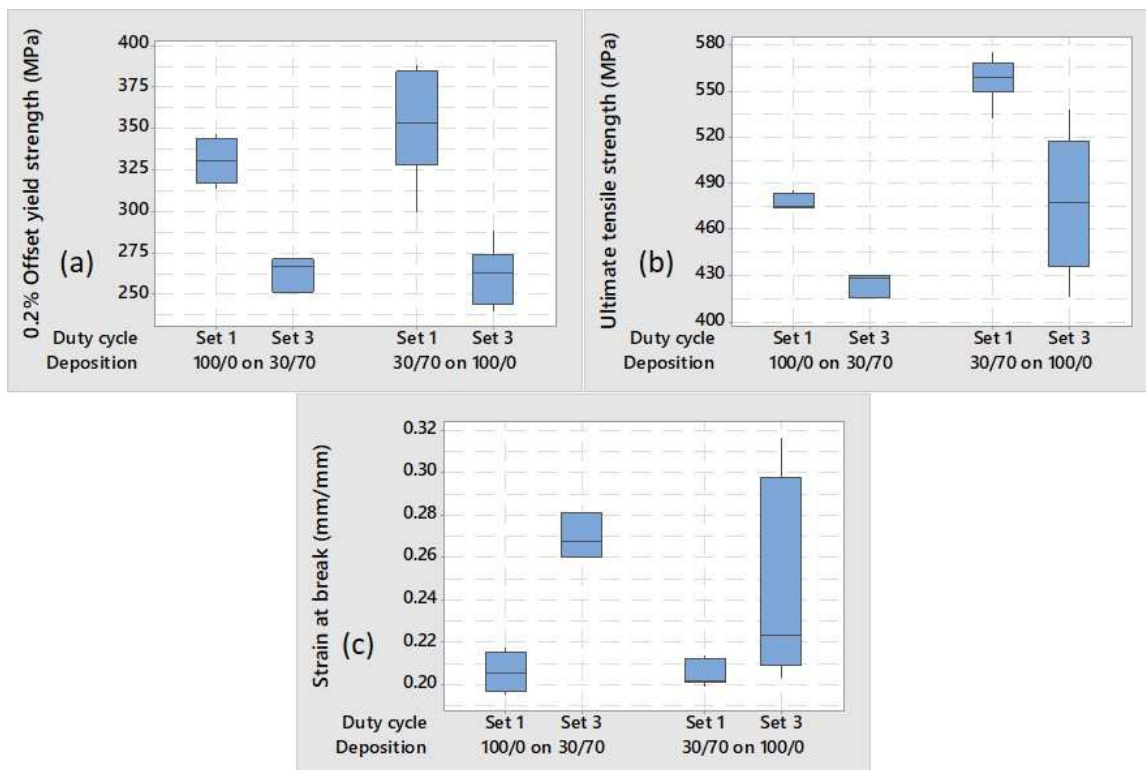


Figure 17. Box and whisker plots of (a) 0.2% Offset yield strength, (b) Ultimate tensile strength and (c) strain at break from crosshead displacement for the miniature tensile specimens prepared from deposits of different combinations. The box spans the 25th and 75th quartile, the vertical lines indicate the range between the minimum and maximum values, and the horizontal line indicates the median value.

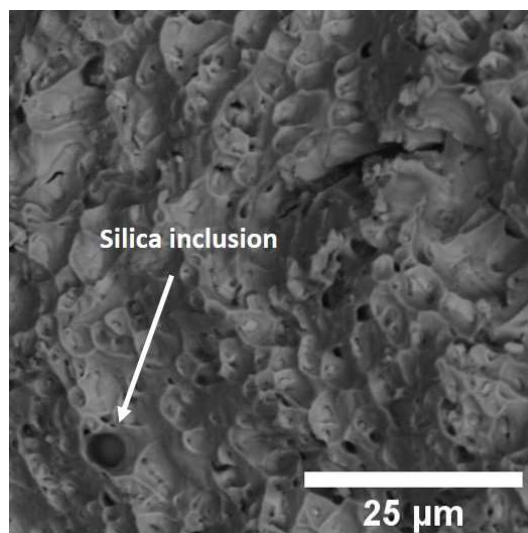


Figure 18. Silica inclusion on the fracture surface of a tensile specimen prepared from Set 3 30/70 on 100/0 deposit.

and size of these inclusions could be influenced. This could be leading to the drop in strength as seen in both combinations of pre-deposit and deposit material. To validate these claims fracture surfaces of broken tensile samples were investigated. A backscattered electron image of the fracture surface is shown in Figure 18. From the fracture surface, an inclusion situated inside the material can be clearly seen. Dimples probably originating from voids nucleated due to the presence of inclusions can also be seen. Presence of such inclusions within the material can lead to early micro-void nucleation and coalescence leading to early failures. In order to further assess the development of the inhomogeneous strain distribution, the strain measurements along the center line of the gage length at different strain values were charted. These trends in strain can be seen in Figures 19 to 22.

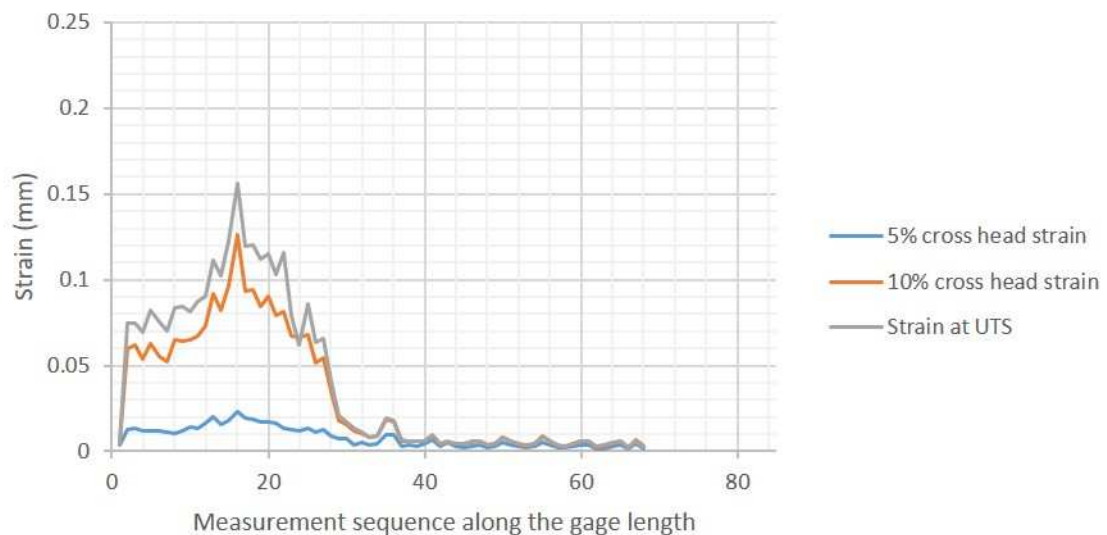


Figure 19. Strain values calculated along the center-line of the gage length of miniature tensile specimens cut from deposits of Set 1 duty cycle for 100/0 on 30/70.

From Figure 19 to 22, the variation and evolution of strain along the center line of the gage length can be observed. The distinction between the nickel-rich and copper-rich sections of the gage length is obvious from the significant difference in strain values along the center line. At relatively low values of overall strain such as 5% cross head strain, a gradual rise in strain from the inflection point can be observed. However, as the overall strain

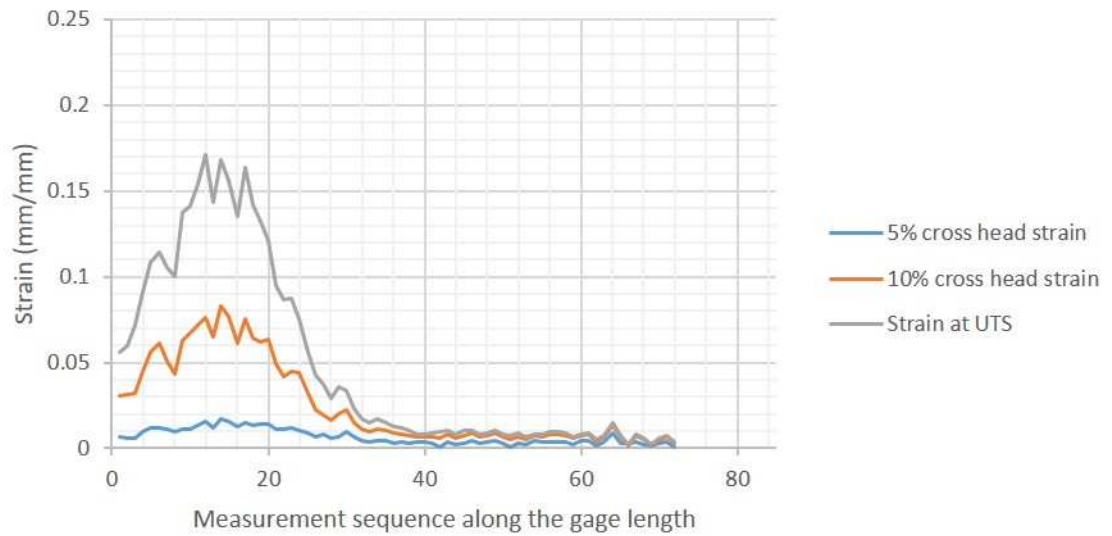


Figure 20. Strain values calculated along the center-line of the gage length of miniature tensile specimens cut from deposits of Set 1 duty cycle for 30/70 on 100/0.

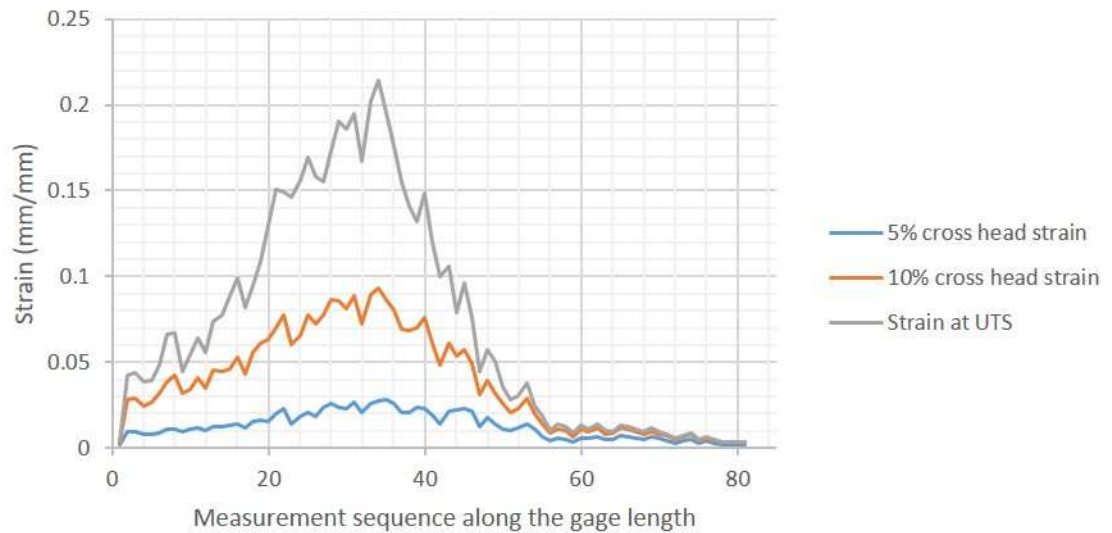


Figure 21. Strain values calculated along the center-line of the gage length of miniature tensile specimens cut from deposits of Set 3 duty cycle for 100/0 on 30/70.

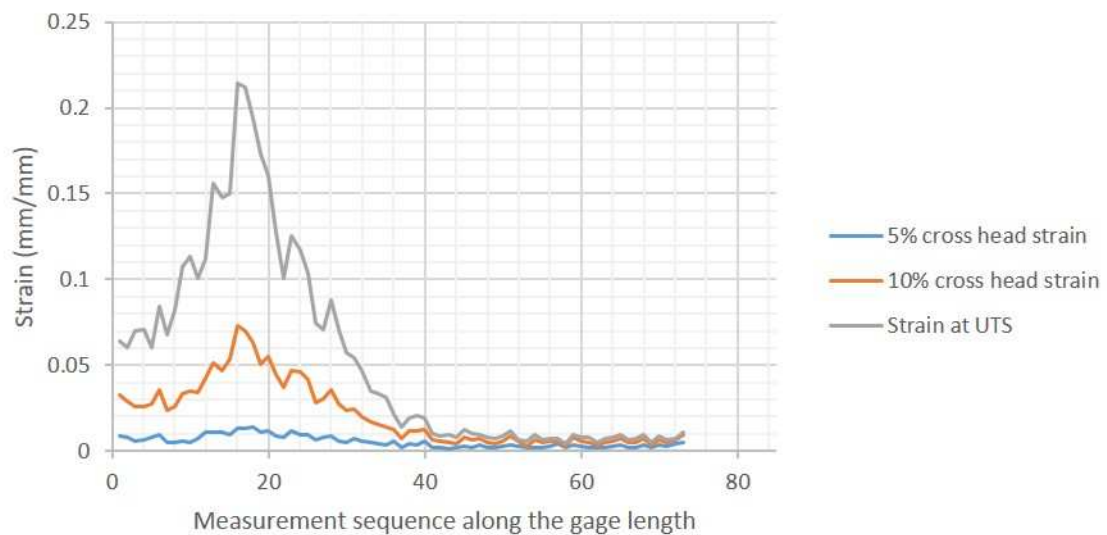


Figure 22. Strain values calculated along the center-line of the gage length of miniature tensile specimens cut from deposits of Set 3 duty cycle for 30/70 on 100/0.

increases, the initiation of localized strain was seen. This was observed to always occur within the copper-rich side of the specimens and away from the interface. This suggests to good bonding between the deposit and pre-deposit in all cases of deposition. This is also indicative of failure within the copper-rich side and not the interface of the deposit.

4. CONCLUSIONS

- Utilizing pulsed width modulation to vary laser power was identified as a viable means for manipulating the chemical gradient in a graded material
- Varying duty cycle and deposition sequence was shown to significantly alter the chemical gradient, in some cases, the length of the gradient was observed to more than double
- The influence of varying duty cycle was characterized and validated through EDS analysis

- The varying chemistry was shown to produce a difference in Vickers hardness and tensile performance
- Strain field estimation using DIC during tensile testing revealed localization of strain to only the copper-containing area of the gage length
- Within the copper-containing portion of gage length, a gradient in strain was also observed
- From the strain field analysis, the failure was believed to occur away from the dissimilar material interface

ACKNOWLEDGEMENTS

This project was supported by Department of Energy Grant No. DE-SC0018879, National Science Foundation Grant No. CMMI 1625736, the Intelligent Systems Center, Center for Aerospace Manufacturing Technologies, and Material Research Center at Missouri S&T. Their financial support is greatly appreciated.

REFERENCES

- [1] MFGM Koizumi. FGM activities in Japan. *Composites Part B: Engineering*, 28(1):1–4, 1997.
- [2] E L Doubrovski, E Y Tsai, D Dikovskiy, J M P Geraedts, H Herr, and N Oxman. Voxel-based fabrication through material property mapping: A design method for bitmap printing. *Computer-Aided Design*, 60:3–13, 2015.
- [3] Woo Y Lee, David P Stinton, Christopher C Berndt, Fazil Erdogan, Yi-Der Lee, and Zaher Mutasim. Concept of Functionally Graded Materials for Advanced Thermal Barrier Coating Applications. *Journal of the American Ceramic Society*, 79(12):3003–3012, 1996.
- [4] Y. Miyamoto, W.A. Kaysser, B.H. Rabin, A. Kawasaki, and R.G. Ford. *Functionally Graded Materials: Design, Processing and Applications*. Materials Technology Series. Springer US, 2014.

- [5] Pierre Muller, Pascal Mognol, and Jean-Yves Hascoet. Modeling and control of a direct laser powder deposition process for Functionally Graded Materials (FGM) parts manufacturing. *Journal of Materials Processing Technology*, 213(5):685–692, may 2013.
- [6] Fumio Watari, Atsuro Yokoyama, Mamoru Omori, Toshio Hirai, Hideomi Kondo, Motohiro Uo, and Takao Kawasaki. Biocompatibility of materials and development to functionally graded implant for bio-medical application. *Composites Science and Technology*, 64(6):893–908, 2004.
- [7] U Leushake, A N Winter, B H Rabin, and B A Corff. General Aspects of FGM Fabrication by Powder Stacking. In *Materials Science Forum*, volume 308-311, pages 13–18. Trans Tech Publications, 2016.
- [8] F. Thümmel, R. Oberacker, and Institute of Materials (Great Britain). *An Introduction to Powder Metallurgy*. Book (Institute of Materials (London, England)). Institute of Materials, 1993.
- [9] Basil R Marple Boulanger, Jean. Graded Casting of Materials with Continuous Gradients. *Journal of the American Ceramic Society*, 77(10):2747–2750, 2016.
- [10] Tomasz Durejko, Michał Ziętała, Wojciech Polkowski, and Tomasz Czujko. Thin wall tubes with Fe 3 Al/SS316L graded structure obtained by using laser engineered net shaping technology. *Materials & Design*, 63:766–774, 2014.
- [11] Ting-ting Qian, Dong Liu, Xiang-jun Tian, Chang-meng Liu, and Hua-ming Wang. Microstructure of TA2/TA15 graded structural material by laser additive manufacturing process. *Transactions of Nonferrous Metals Society of China*, 24(9):2729–2736, 2014.
- [12] H S Ren, D Liu, H B Tang, X J Tian, Y Y Zhu, and H M Wang. Microstructure and mechanical properties of a graded structural material. *Materials Science and Engineering: A*, 611:362–369, 2014.
- [13] Kamran Shah, Izhar ul Haq, Ashfaq Khan, Shaukat Ali Shah, Mushtaq Khan, and Andrew J Pinkerton. Parametric study of development of Inconel-steel functionally graded materials by laser direct metal deposition. *Materials & Design (1980-2015)*, 54:531–538, 2014.
- [14] Waheed Ul Haq Syed, Andrew J Pinkerton, Zhu Liu, and Lin Li. Coincident wire and powder deposition by laser to form compositionally graded material. *Surface and Coatings Technology*, 201(16):7083–7091, 2007.
- [15] Dongjiang Wu, Xiaokang Liang, Qian Li, and Lijia Jiang. Laser Rapid Manufacturing of Stainless Steel 316L/Inconel718 Functionally Graded Materials: Microstructure Evolution and Mechanical Properties. *International Journal of Optics*, 2010:1–5, 2010.

- [16] Weiping Liu and J N DuPont. Fabrication of functionally graded TiC/Ti composites by laser engineered net shaping. *Scripta Materialia*, 48(9):1337–1342, 2003.
- [17] Kamran Shah. *Laser direct metal deposition of dissimilar and functionally graded alloys*. PhD thesis, The University of Manchester (United Kingdom), 2011.
- [18] Jingyuan Yan, Ilenia Battiato, and Georges M. Fadel. Planning the process parameters for the direct metal deposition of functionally graded parts based on mathematical models. *Journal of Manufacturing Processes*, 31:56–71, jan 2018.
- [19] Wei Li, Sreekar Karnati, Yunlu Zhang, and Frank Liou. Investigating and eliminating powder separation in pre-mixed powder supply for laser metal deposition process. *Journal of Materials Processing Technology*, 254:294–301, apr 2018.
- [20] W. Li, S. Karnati, C. Kriewall, F. Liou, J. Newkirk, K.M. Brown Taminger, and W.J. Seufzer. Fabrication and characterization of a functionally graded material from Ti-6Al-4V to SS316 by laser metal deposition. *Additive Manufacturing*, 14, 2017.
- [21] Yoshimi Watanabe, Yoshifumi Inaguma, Hisashi Sato, and Eri Miura-Fujiwara. A Novel Fabrication Method for Functionally Graded Materials under Centrifugal Force: The Centrifugal Mixed-Powder Method. *Materials*, 2(4):2510–2525, dec 2009.
- [22] Xueyang Chen, Lei Yan, Wei Li, Zhiyuan Wang, Frank Liou, and Joe Newkirk. Effect of Powder Particle Size on the Fabrication of Ti-6Al-4V Using Direct Laser Metal Deposition from Elemental Powder Mixture. *Journal of Mechanics Engineering and Automation*, 6(7), jul 2016.
- [23] Lei Yan, Xueyang Chen, Wei Li, Joseph Newkirk, and Frank Liou. Direct laser deposition of Ti-6Al-4V from elemental powder blends. *Rapid Prototyping Journal*, 22(5):810–816, 2016.
- [24] B Ye, M R Matsen, and D C Dunand. Blended elemental powder densification of Ti-6Al-4V by hot pressing. *Journal of Materials Research*, 26(8):965–969, 2011.
- [25] Yunlu Zhang, Lei Yan, and Frank Liou. Improved initial guess with semi-subpixel level accuracy in digital image correlation by feature-based method. *Optics and Lasers in Engineering*, 104:149–158, may 2018.
- [26] Sörn Ocylok, Eugen Alexeev, Stefan Mann, Andreas Weisheit, Konrad Wissenbach, and Ingomar Kelbassa. Correlations of Melt Pool Geometry and Process Parameters During Laser Metal Deposition by Coaxial Process Monitoring. *Physics Procedia*, 56:228–238, jan 2014.
- [27] A Cohen. Properties of Cast Copper Alloys. *ASM Handbook*, Vol 2(Properties and Selection: Nonferrous Alloys and Special-Purpose Materials):p 356–391, 1990.
- [28] Mohammed Naeem. Laser Processing of Reflective Materials. *Laser Technik Journal*, 10(1):18–20, jan 2013.

- [29] M. Javidani, J. Arreguin-Zavala, J. Danovitch, Y. Tian, and M. Brochu. Additive Manufacturing of AlSi10Mg Alloy Using Direct Energy Deposition: Microstructure and Hardness Characterization. *Journal of Thermal Spray Technology*, 26(4):587–597, apr 2017.
- [30] A A Adeyemi, ET Akinlabi, R M Mahamood, K O Sanusi, S Pityana, and M Tlotleng. Influence of laser power on microstructure of laser metal deposited 17-4 ph stainless steel. *IOP Conference Series: Materials Science and Engineering*, 225(1):012028, aug 2017.

III. SUBSTRATE PREHEATING DURING LASER METAL DEPOSITION OF AL4047 ON AL2024 AND AL6061

Sreekar Karnati*, Sriram Praneeth Isanaka, Frank F. Liou

Department of Mechanical & Aerospace Engineering

Missouri University of Science and Technology

Rolla, Missouri 65409–0050

*Corresponding author, Tel: 573–341–4603, Fax: 573–341–4115

Email: skw92@mst.edu

ABSTRACT

Laser Metal Deposition (LMD) of aluminum and its alloys is challenging due to their high reflectivity and thermal conductivity. However, Al4047, an aluminum-silicon alloy was found to be viable for LMD due to the low reflectivity and increased absorbance caused by the presence of silicon. Leveraging remelting, Al4047 was deposited on unworkable alloys such as Al2024 and Al6061. While feasible, deposition of Al4047 on these alloys was found to be unreliable. At room temperature, a large amount of energy input was found to be necessary for initiating deposition. Reliability of deposition initiation was also found to be questionable, issues of balling were found to hinder successful deposition. Preheating substrate to a temperature of 200°C was found to be a solution to these issues. Preheating the substrate improved the reliability of deposition initiation and also reduced the amount of energy needed for deposition. A contrast between the outcomes from depositing at room temperature and 200°C was performed through SEM, EDS, hardness and mini-tensile testing. Deposits from both conditions yielded good bonding with the substrate. Analysis of microstructure revealed different transitions between substrate and deposit for different temperatures. Small vertical cracks were observed across the substrate-part interface. These

were suspected to be a consequence of the thermal stresses during deposition. Failure during tensile testing occurred within the deposit indicating a strong bond between the deposit and the substrate.

Keywords: Additive manufacturing; aluminum alloys; cooling rates; dissimilar alloys; graded materials; mini-tensile testing

1. INTRODUCTION

Laser Metal Deposition (LMD) is a type of Additive Manufacturing (AM) process that is capable of processing metals and alloys in powder form with the aid of high energy sources such as lasers and electron beams [1]. The high energy source creates a molten pool of material on a substrate. Powder particles that are transported by a gas stream are then injected into this melt pool. This leads to the melting and deposition of the powder material onto the substrate [2]. This process is repeated in a layer by layer manner where every newly deposited layer melts and metallurgically bonds with its predecessor [3]. Leveraging the motion systems in an LMD system, complex tool paths can be implemented for deposition. This facilitates the fabrication of complex and intricate geometries. The unique ability to deliver both the material and the energy to specific locations of need has also made LMD systems viable repair solutions. This paper focuses on this deposition and repair capability of LMD systems in an effort to widen their applicability to alloy systems previously considered unsuitable.

LMD systems have existed for over a decade and have achieved significant success in processing iron, titanium, and nickel-based alloys, and even some metal matrix composites. Their ability to process aluminum alloys though has been limited by aluminum's high reflectivity to commonly available wavelengths of incident laser light [4]. To overcome this issue, researchers have proposed solutions that use lower wavelength lasers, or use a higher energy input that in turn increases the energy absorbed by the material [5, 6]. They are actively trying to understand and quantify the energy densities associated with

different process parameters when processing aluminum alloys [7]. Some researchers have even promoted powder-bed systems over LMD systems owing to their different absorption and reflectivity characteristics and in some cases have even developed hybrid processes [8, 9, 10, 11, 12]. Others have tried to use pulsed lasers to ablate small volumes of material on the surface of a substrate, which again allows for the greater absorption as compared to a flat aluminum substrate [13, 14, 15, 16].

Aluminum alloys have always found favor in applications that have demanded high strength to weight ratios [17]. Their lower densities make them ideal for aerospace and other applications that prize weight savings while still exhibiting exceptional strength. Some aluminum alloys are even being looked at as replacements for steel. Owing to their favorable properties, they have been employed in the manufacture of a large number of aerospace components which today require repair and refurbishment. While replacement of the component is viable in some scenarios, it is an expensive solution. In other cases, even the supply chain needed to repair these legacy components have long been shut down. In order to address this knowledge shortfall, organizations like the United States Navy are trying to develop novel solutions with the capability to additively manufacture and repair these legacy components. The research presented in this paper is a step in this direction and provides a process solution that can be adopted and implemented in existing LMD systems to address this need. An additional benefit of this research would be the ability to add features to pre-cast parts which would bridge the flexibility of LMD systems to the favorable economics of conventional manufacturing.

2. RATIONALE

Al4047 is an aluminum-silicon alloy with 11-13 %wt. in silicon. This alloy is primarily used in welding applications. Particularly it is used as a filler material for welding Al6061 alloy. The feasibility for depositing Al4047 using LMD systems has previously been demonstrated [18, 19]. The silicon in the alloy is expected to lower the reflectivity.

Since in LMD, the feedstock is used in powder form, a higher absorption is also expected due to the large surface area of the powder. Both these attributes make this alloy viable for LMD applications. This alloy can thereby be used to add features and repair existing components made from reflective aluminum alloys.

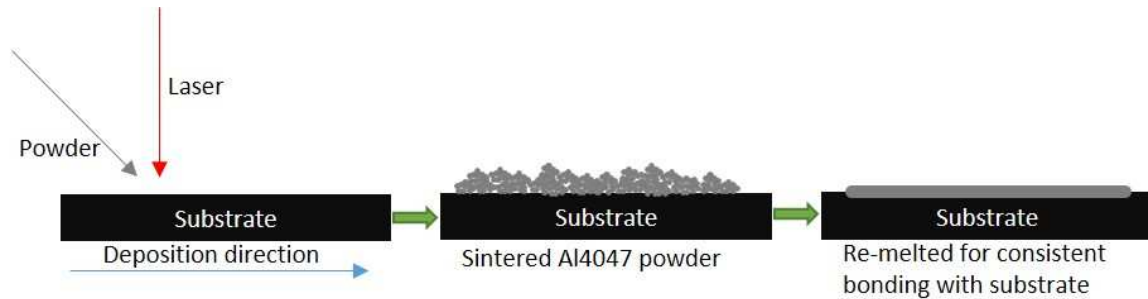


Figure 1. Deposition of Al4047 on Al2024 through sintering followed by remelting [19].

Al2024 is a highly reflective alloy. Most solid-state lasers, especially the ones in the infrared spectrum cannot easily process such an alloy [20]. However, through sintering and then remelting Al4047 on the surface of the Al2024 substrate, successful bonding between the two has been demonstrated [19]. A schematic representation of their deposition strategy is shown in Figure 1. While feasible, this approach has been identified to be less reliable at room temperature. In this approach, the successful initiation and sustenance of the melt pool during LMD is dependent on the successful sintering of Al4047 powder. The high thermal conductivity of the aluminum alloys makes it challenging to sinter Al4047 powder on the substrate. Inconsistent amounts of sintering have been identified to lead to balling and thereby failing in a deposition. The outcome from 4 replications of 8 layer deposition of Al4047 on Al2024 is shown in Figure 2. While identical process parameters were used for these depositions, a widely varied outcome was noticed. This difference in deposition quality was attributed to varying amounts of success achieved at the first layer of the deposition. Without special measures to favor reliable sintering, the deposition initiation

can be challenging. Also, successful bonding with the substrate is dependent on producing melt pools with sufficient depth to penetrate the sintered powder and the substrate. Large amounts of energy input are necessary to produce the melt pool of required depth.

Substrate preheating was theorized to be an effective means to enable successful sintering in the first layer of deposition. The higher substrate temperature is also expected to lower the temperature gradient and thereby minimize the conduction losses. This is expected to increase in the success rate of deposition. The following work is aimed at assessing the validity of these claims. The influence of increasing the substrate temperature will be assessed through a comparative study between depositions performed at room temperature and elevated substrate temperature.

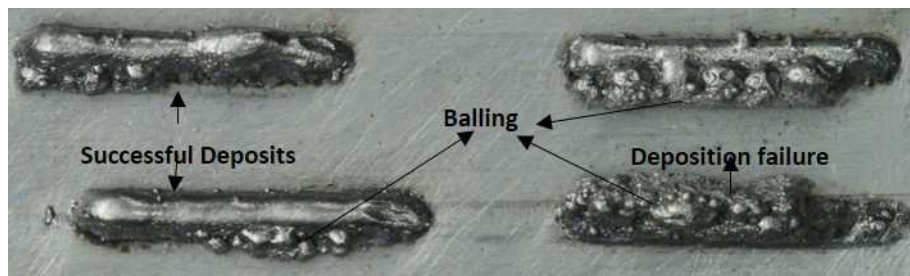


Figure 2. Top view of 4 replications of 8 layer deposits of Al4047 on an Al2024 substrate. Power of 1kW and 150mm/min scan speed were used for all deposits.

3. EXPERIMENTAL SETUP

The experimental setup employed in this research includes a fiber laser from IPG Photonics, which has a peak power of 1kW, an operating wavelength of 1064nm, and a spot size of approximately 2mm in diameter. Different energy inputs during deposition were implemented through pulse width modulation. To change energy input, the peak power was kept constant and the duty cycle was varied. A schematic diagram illustrating the setup of the LMD system used in this study is shown in Figure 3. The motion during deposition was facilitated through a custom fabricated CNC motion stage. The powder was fed using

an edge nozzle as shown in Figure 2. A Baystate model 1200 powder feeder was used to deliver powder for deposition. The powder used for deposition was -100/+325 mesh, gas atomized Al4047 powder acquired from Valimet Inc.

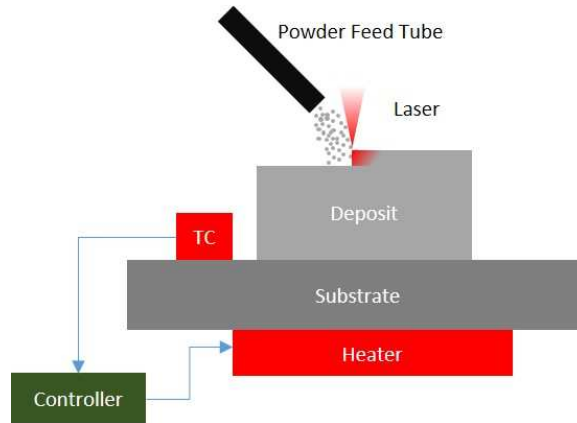


Figure 3. Schematic layout of the deposition system used in the current study. TC is the thermocouple used to read the temperature on the deposition surface of the substrate.

Bar stock pieces of 4"x1"x1" cross section were used for deposition. These substrates were prepared from commercially procured Al2024 and Al6061 alloy. In order to preheat the substrate before and during deposition, a closed loop heating setup was incorporated into the deposition system. The temperature on the top surface of the substrate was tracked to maintain the required preheat temperature. With the increase in preheat temperature, the ease in deposition initiation was also seen to increase. While preheating 4"x1"x1" pieces of bar stock is not particularly challenging, implementing preheat on large and existing components can be challenging. This challenge only increases with increase in preheat temperature. A preliminary optimization based on deposition success and visual inspection was performed to identify the deposition parameters. The optimized parameters used for the study are shown in Table 1.

An FEI Helios NanoLab 600 FIB/FESEM with an Oxford energy dispersive spectrometer was used to estimate the chemical composition. A HIROX optical microscope was also employed for microstructural imaging. The variation in mechanical properties

Table 1. Optimized process parameters employed in the experimentation.

Substrate temperature (K)	Power (kW)	Duty Cycle (%)	Scan speed (mm/min)	Input energy density (Power/Scan speed) (MJ/m)
300	1	100	150	0.4
473	1	43	450	0.057

was realized through Vickers microhardness testing. An Instron universal testing machine, customized for miniature tensile testing was used to characterize deposit-substrate interfacial bond strength. The deposits were sliced to 1mm thicknesses and miniature tensile specimens were cut across the substrate deposit interface. These specimens were tested to evaluate the bond integrity between the deposit and the substrate. The dimensions of the mini-tensile specimen and locations of specimens cut on deposit performed on Al2024 at room temperature are shown in Figure 4. A Hansvedt DS-2 wire-EDM was used to machine the mini-tensile specimens.

4. RESULTS AND DISCUSSION

Incorporating substrate preheating into deposition significantly improved the deposition success rate and quality. At room temperature, large amounts of energy input, 1kW peak power at 100 % duty cycle and a slow scan speed of 150mm/min were necessary to perform deposition on both Al2024 and Al6061 alloys. A large amount of energy input was necessary to account for the low absorption and high thermal conductivity of both the alloys. Through preheating the substrate the thermal gradient was to be lowered and thereby the conduction losses were expected to be minimized. Also, the increase in substrate temperature was expected to favor sintering of Al4047 powder during the initial layers of deposition. The improvement in deposition quality with substrate preheating can

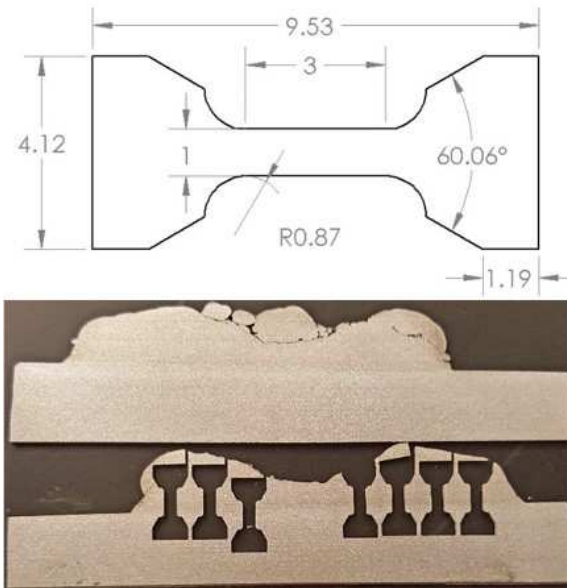


Figure 4. Dimensions of the miniature tensile specimen in mm (top). A 1mm thick longitudinal slices of Al4047 deposit on Al2024 substrate performed at room temperature and locations along the deposit-substrate interface from which specimens have been prepared.

be seen in Figure 5. While the improvement in deposit quality and ease of deposition were apparent, the influence on the constitution of the deposit-substrate interface and deposit needed investigation.



Figure 5. 2inch long deposit of Al4047 on an Al6061 substrate at room temperature (left) and 1inch long deposit of Al4047 on an Al6061 substrate preheated to 473K (right).

In order to assess the quality of the bond between the substrate and the deposit, transverse cross-sections of the deposits were prepared. These sections were mounted in Bakelite, ground and polished to visualize the interface between the two. The last stage of polishing was using 0.05micron colloidal silica. The presence of silicon in the

deposit provides a natural contrast and the specimens can be examined in the as-polished condition. In the case of both the alloys, there is a stark difference between the interfaces of deposits made with and without preheating. In the room temperature deposition case, for both the alloys, the start of the deposit can be seen through a very sharp transition in the microstructure. However, in the case with preheat, the transition in microstructure is comparatively more gradual. In LMD, during the deposition of dissimilar alloys, at the interface between the two alloys, there is a transition in chemistry from the former alloy to the latter. This transition is referred to as the dilution zone. From the microstructure images in Figure 6, the different substrate temperatures during deposition seem to have influenced the constitution of this dilution zone.

It is to be noted that different power and scan speeds were used for the deposits at different substrate temperatures. This difference in process parameters is known to influence the size and shape of the melt pool. In the case of the deposition at room temperature, intentionally large amounts of energy were supplied for the deposition. This amount of energy input is expected to have created deep melt pools and large deposition volumes in each layer. Therefore the transition in the microstructure is suspected to be steep. Whereas in the case of the preheated substrate, a lower energy input and faster scan speed have been employed. This is expected to produce a shallower melt pool and a small deposition volume end of each layer. This is presumed to have created a comparatively more gradual transition at the interface.

For the most part, the above-discussed deposits were found to have minimal flaws. Sporadic porosity both irregular (possible lack of fusion or cold shut) and spherical (gas porosity) in shape can be observed in them. Possible micro-cracks have also been observed. Particularly in the deposit made on an Al6061 substrate with preheating. From Figure 6(d), thin cracks originating from the interface into the substrate can be observed. The vertical

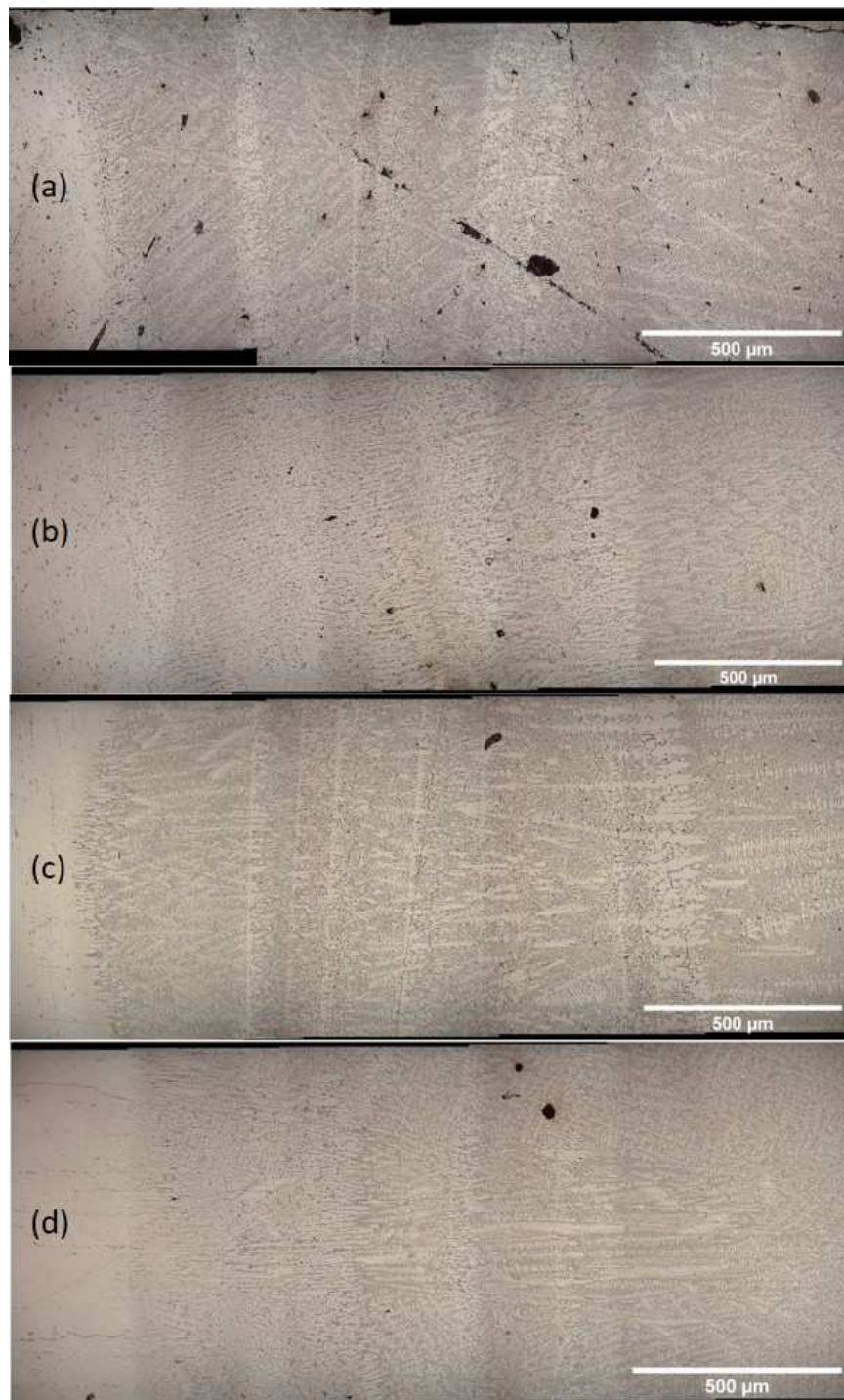


Figure 6. Stitched optical microscope images of microstructure gathered at the interfaces of deposits of all conditions. The substrate to deposit progression from left to right.(a). Al4047 on an Al2024 substrate at room temperature (b). Al4047 on an Al2024 substrate preheated to 473K (c). Al4047 on an Al6061 substrate at room temperature (d). Al4047 on an Al6061 substrate preheated to 473K.

nature of these cracks suggests these could be due to residual stresses generated during deposition. The steep thermal gradient inherent to LMD can create large residual stresses which can lead to crack formation and propagation.

In order to validate the above-shown transition in microstructure was actually the transition in chemistry, EDS line scans were performed across the interfaces of deposits for all conditions. The variation in aluminum and silicon contents was tracked to pinpoint the start of the deposit and end of the substrate. The transition in microstructure was observed to correlate with the change in chemistry observed in the EDS line scans. Data from a line scan performed across the interface of an Al4047 deposit on an Al2024 substrate with preheating is shown in Figure 7. The transition from substrate to deposit can be realized by the rise in the intensity of the silicon signal. The alternating silicon and aluminum signals are a characteristic feature of the Al4047 microstructure. Al4047 is a hypo-eutectic alloy. The microstructure is constituted of primary β -aluminum as dendrites and eutectic (alternating β -aluminum and silicon) microstructure. The same can be realized of the EDS map shown in Figure 8. The blank spots in the silicon color map correspond to the presence of primary β -aluminum.

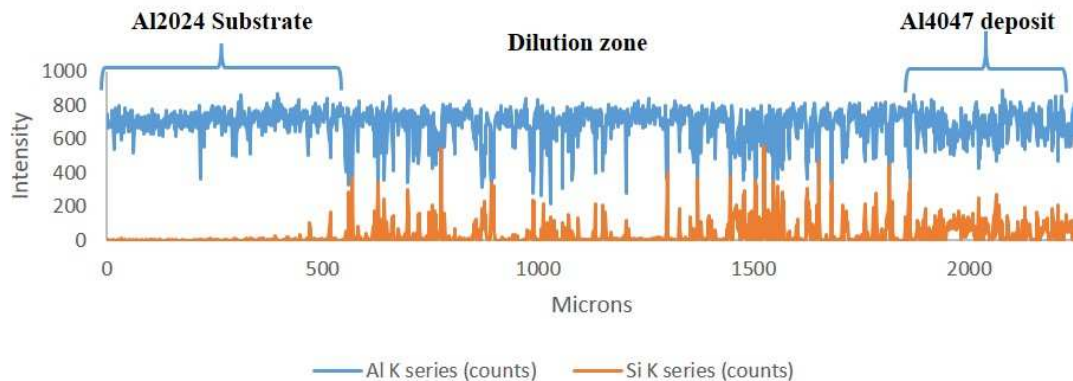


Figure 7. Secondary electron image with a false color overlay of EDS area map showing the silicon (yellow) and aluminum (blue) in the microstructure of Al4047 deposit.

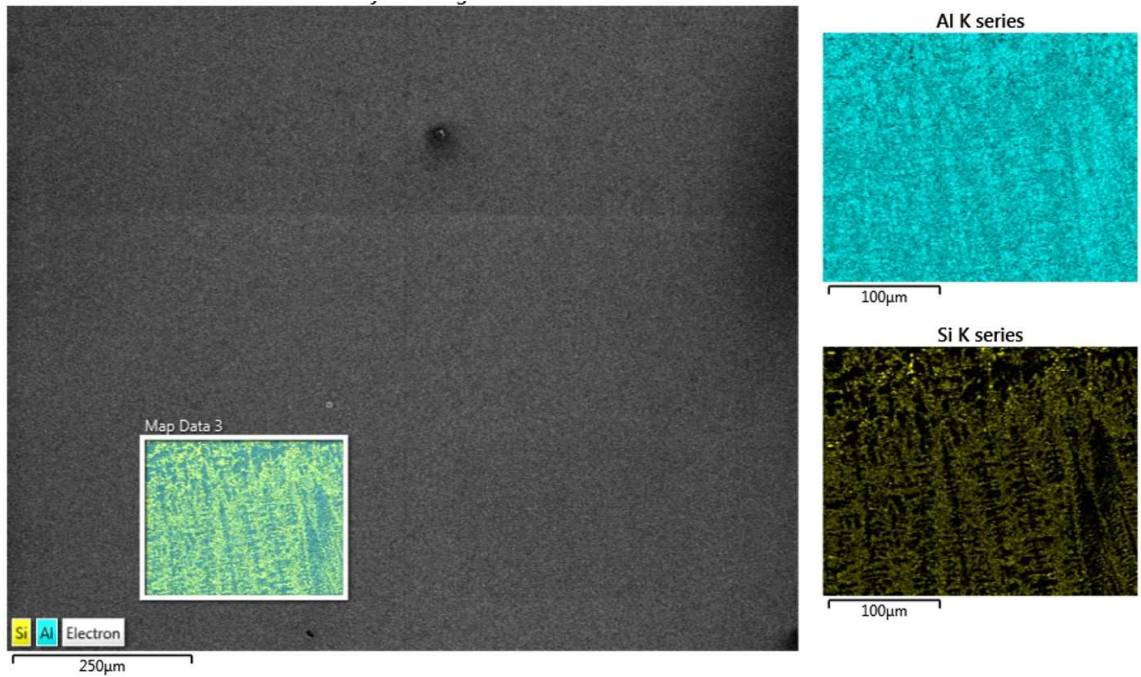


Figure 8. EDS line scan data gathered across the interface of an Al4047 deposit on an Al2024 substrate with substrate preheat. The rise in counts of silicon indicates the start of the deposit.

From the microstructure images in Figure 6, differences in the overall dendrite morphology can be clearly observed. This difference is suspected to be a consequence of different substrate temperatures and composition. Also, bands of dendrites possibly correlating with the deposited layers can also be observed. The influence of different substrates and preheat temperatures was evaluated through the estimation of the average cooling rate. The Secondary Dendrite Arm Spacing (SDAS) in the Al4047 deposits was measured and analyzed to estimate average cooling rate [18]. These measurements were performed within the deposit in locations near and sufficiently far from the substrate. The 95% confidence intervals of measured SDAS values and calculated cooling rate values are shown in Figure 9. From these values, with increase in substrate temperature the cooling rate at the top of the Al4047 deposit (locations sufficiently far from the substrate where its influence can be ignored) for the Al2024 substrate is expected to decrease. Whereas for the case of

Al6061 no significant change was observed. However, for the case of preheated Al6061, the improved deposition efficiency and lowered energy input seem to have resulted in a significant increase in cooling rate. This difference from Al2024 is suspected to be due to the differences between thermal absorption and conductivity between the two alloys. Al6061 has a higher thermal conductivity than Al2024 alloy and could have therefore resulted in a higher cooling rate. This high cooling rate in Al6061 could be the reason for the cracks seen in Figure 6(d). This warrants further optimization of process parameters to eliminate issues of cracking.

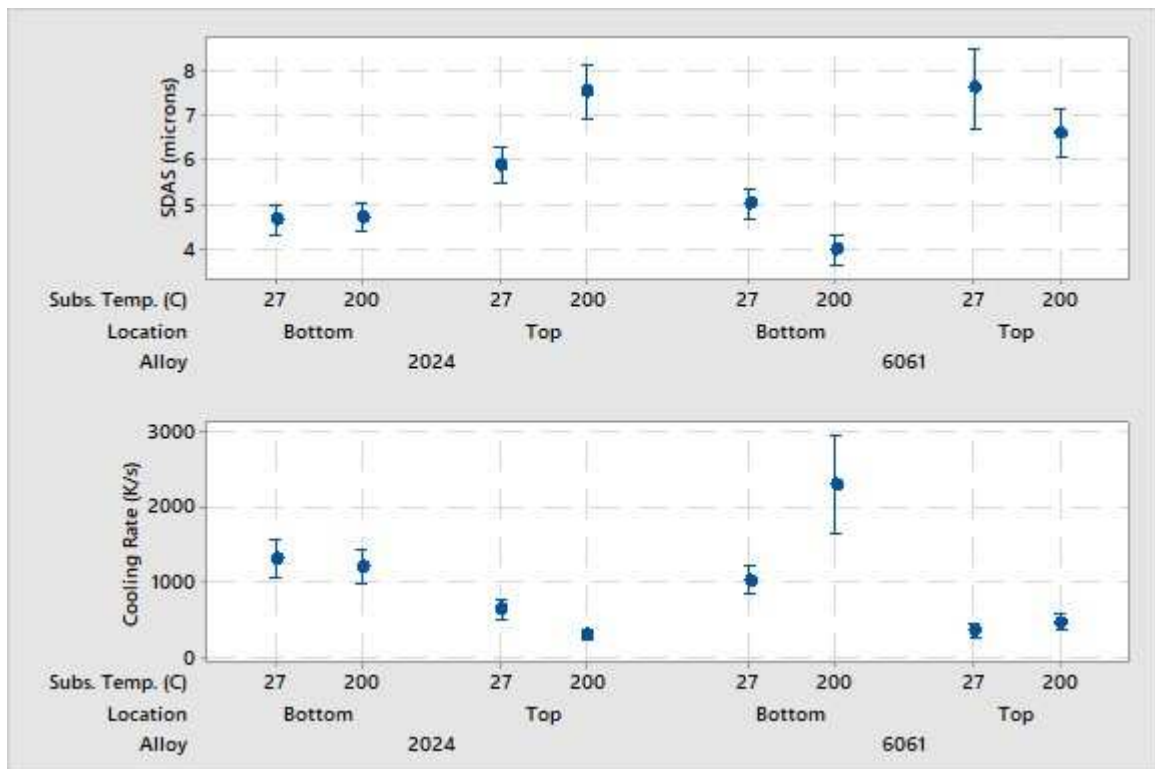


Figure 9. 95% confidence intervals of measured SDAS values and calculated average cooling rates.

In order to assess the variation in the mechanical properties along the substrate-deposit interface, Vickers microhardness testing was performed. The hardness data from all the 4 cases are shown in Figure 10. The transition from substrate to deposit is apparent in all cases. The hardness of the deposit was comparable in all the cases. Al2024 was observed

to have a higher hardness value in comparison with deposited Al4047. However, preheating was observed to have increased the hardness of the alloy. Al6061, on the other hand, was harder than the deposit when fabricated under room temperature. Upon preheating, the hardness of the alloy seems to have been lowered. From either case, it is apparent that preheating can change the material properties of the substrate. This can be an issue while depositing on pre-existing components. Follow up heat treatments might be necessary to recondition the parts post LMD fabrication.

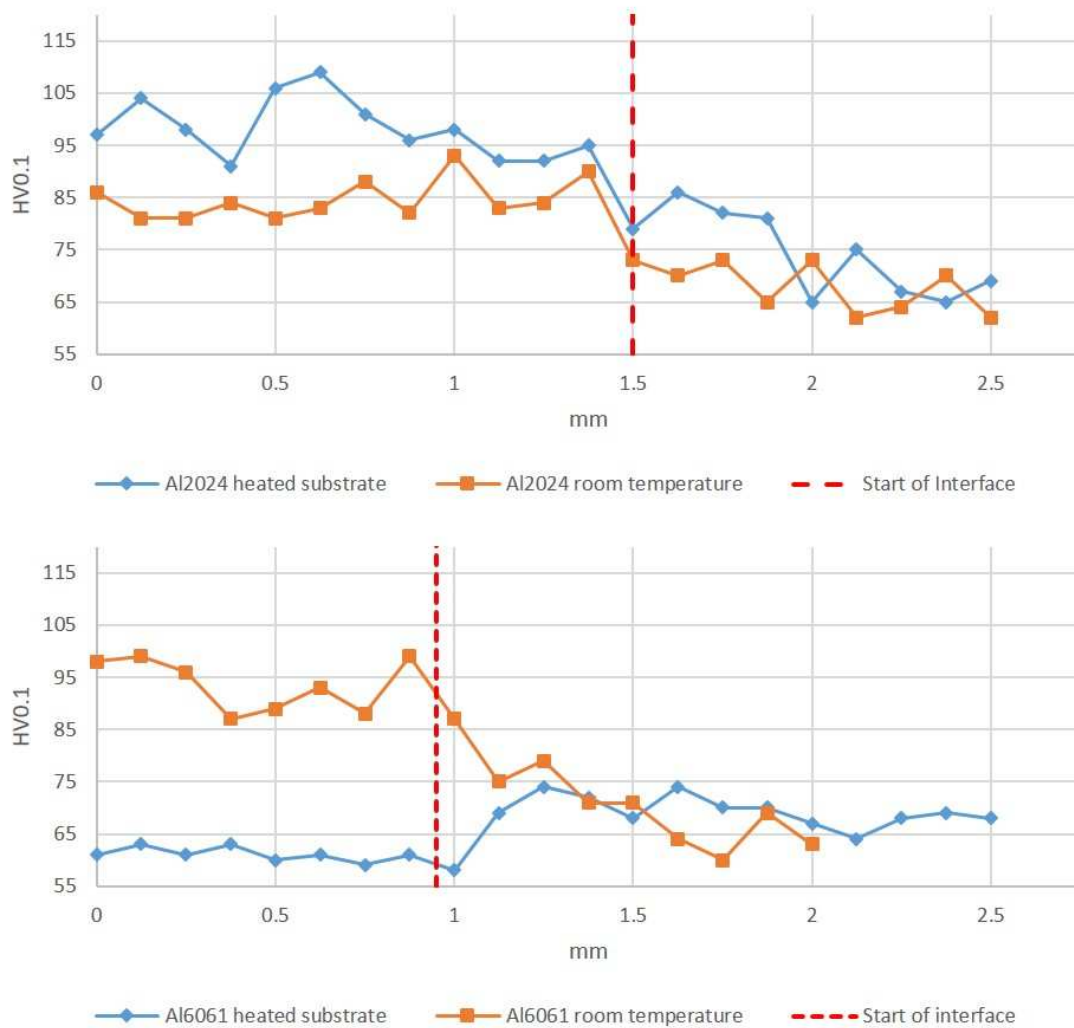


Figure 10. Variation of microhardness across the substrate-deposit interface of Al4047 deposits on both Al2024 and Al6061 alloys.

The integrity of the substrate-deposit bond was investigated through mini-tensile testing. Mini-tensile samples were cut from the deposits of all 4 cases. The substrate-deposit interface was located within the gage length of these specimens. These specimens were tested at a constant strain rate of 10-3mm/mm/s. The crosshead displacement of the testing machine was tracked to calculate the elongation and strain of the specimens. For comparison metrics, commercially procured cold rolled and annealed Al4047 was also tested. The data from these tensile tests is shown in Figure 11. The strength of the deposits was comparable if not higher than the strength of the wrought specimens. While the strength values were comparable among the deposits, the strain values were seen to vary across the different cases. However, there was no discernable trend to the variation in strain values.

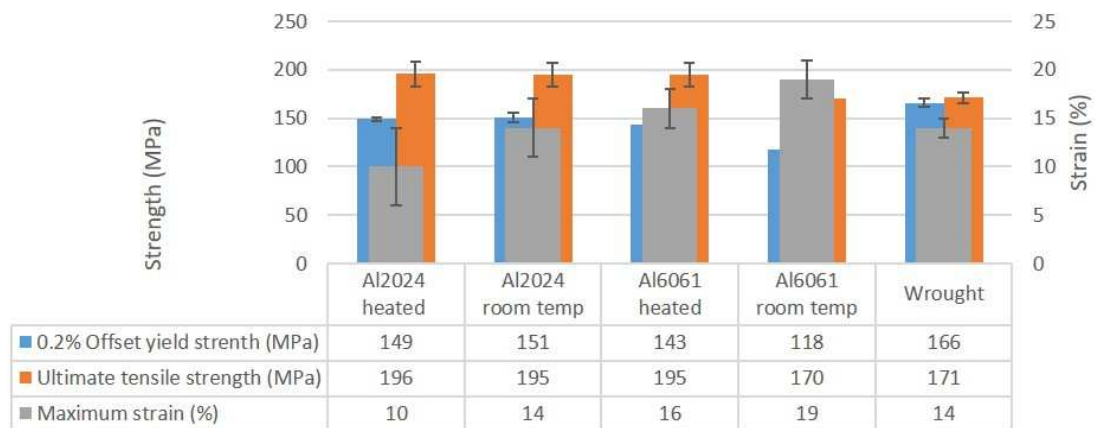


Figure 11. Mechanical property values from mini-tensile testing with one-sigma error bars.

As an extension, the fracture surfaces of the mini-tensile specimens were analyzed to determine the nature of the fracture and the zone that yielded. Most of the samples failed in the Al4047 zone or the deposit zone. This was verified by using SEM image data as shown in Figure 12 and confirmed using EDS line scans. The fracture surfaces indicate the presence of both brittle and ductile fracture elements where the silicon exhibits brittle crack initiation which progresses through the alpha-aluminum as a ductile fracture [21].

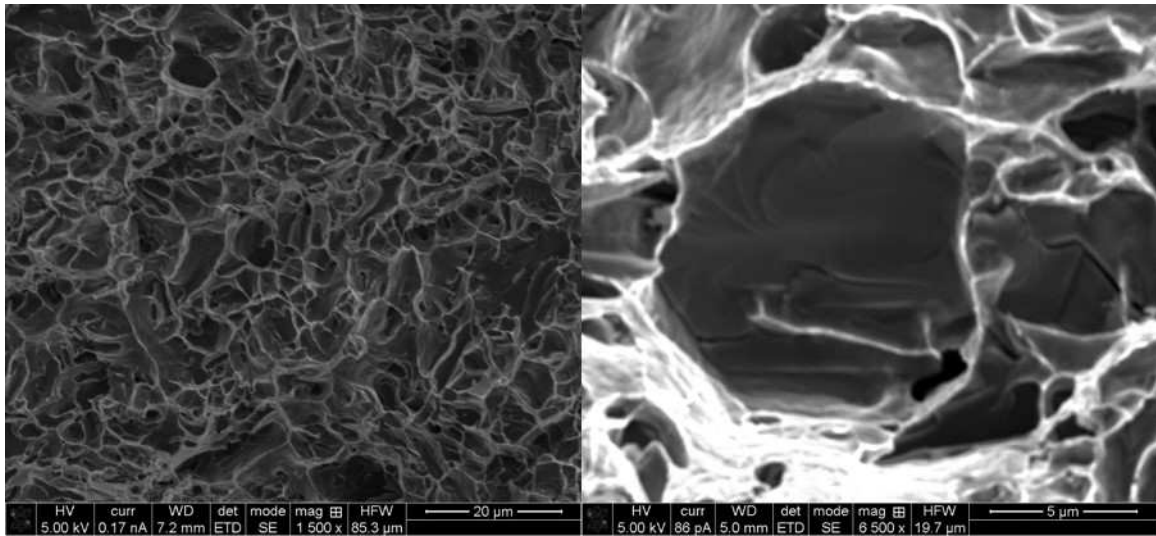


Figure 12. Fracture surface images of broken minitensile sample with ductile (left, alpha aluminum) and brittle (right, silicon) failure signatures.

5. CONCLUSIONS

This research successfully proves the capability of existing LMD systems to manufacture and repair aluminum alloy components. Some of the highlights include

- Successful additive manufacturing of thin-wall Al4047 alloy structures
- Substrate preheating seems to improve repeatability of deposition and quality of deposition
- The feasibility of working with Al2024 and Al6061 and adaptability to other aluminum alloys
- The metallurgical bonding of two dissimilar aluminum alloys proving the possibility of functionally grading and repair
- Different dilution zone produced with substrate preheat and different process parameters

- The solid metallurgical bond with the substrate proven with mini-tensile data and fractography
- The consistency of the deposition proven using SEM, EDS and micro-hardness analyses

ACKNOWLEDGEMENTS

The authors would like to thank the support from Intelligent Systems Center (ISC), and Material Research Center (MRC) at the Missouri University of Science and Technology for the help in sample preparation and testing. The support from NSF grants CMMI-1547042 and CMMI 1625736 is also appreciated. The authors would also like to thank Jill Sertell and Jack Hoerchler for their aid in proof-reading this manuscript.

REFERENCES

- [1] J Laeng, J G Stewart, and F W Liou. Laser metal forming processes for rapid prototyping - A review. *International Journal of Production Research*, 38(16):3973–3996, 2000.
- [2] J Mazumder, D Dutta, N Kikuchi, and A Ghosh. Closed loop direct metal deposition: Art to Part. *Optics and Lasers in Engineering*, 34(4-6):397–414, 2000.
- [3] D D Gu, W Meiners, K Wissenbach, and R Poprawe. Laser additive manufacturing of metallic components: Materials, processes and mechanisms. *International Materials Reviews*, 57(3):133–164, 2012.
- [4] Laurentiu Slatineanu, Oana Dodun, Margareta Coteata, Irina Besliu Grigoras, and Lorelei Gherman. Possibilities of using a 1070 nm laser in machining of some metallic materials. In *6th International Conference on Advanced Topics in Optoelectronics, Microelectronics and Nanotechnologies, ATOM-N 2012, August 23, 2012 - August 26, 2012*, volume 8411, pages Romanian Ministry of Education and Research – ANCS, Constanta, Romania, 2012. SPIE.
- [5] Seiji Katayama, Hiroyuki Nagayama, Masami Mizutani, and Yousuke Kawahito. Fibre laser welding of aluminium alloy. *Welding International*, 23(10):744–752, 2009.

- [6] Chang-Da Wen and Issam Mudawar. Emissivity characteristics of roughened aluminum alloy surfaces and assessment of multispectral radiation thermometry (MRT) emissivity models. *International Journal of Heat and Mass Transfer*, 47(17-18):3591–3605, 2004.
- [7] A G Paleocrassas and J F Tu. Low-speed laser welding of aluminum alloy 7075-T6 using a 300-W, single-mode, ytterbium fiber laser. *Welding Journal (Miami, Fla)*, 86(6):179–s–186–s, 2007.
- [8] Xiaoqing Cao and Beshah Ayalew. Control-oriented MIMO modeling of laser-aided powder deposition processes. In *2015 American Control Conference, ACC 2015, July 1, 2015 - July 3, 2015*, volume 2015-July, pages 3637–3642, Chicago, IL, United states, 2015. Institute of Electrical and Electronics Engineers Inc.
- [9] Fuquan Li, Yanbin Chen, Liqun Li, and Lianfeng Wei. Investigation of surface modification of Al alloy by laser-TIG hybrid melt injection WC powder. *Zhongguo Jiguang/Chinese Journal of Lasers*, 36(10):2722–2727, 2009.
- [10] Daniel Moser, Sreekanth Pannala, and Jayathi Murthy. Computation of effective radiative properties of powders for selective laser sintering simulations. *JOM*, 67(5):1194–1202, 2015.
- [11] Alexander Stepanov, Heidi Piili, M Islam, Antti Salminen, and O NyrhilÃd. Comparison of theoretical and practical studies of energy input in laser additive manufacturing (lam) using stainless steel. *Lasers in Engineering*, 28:289–302, 01 2014.
- [12] Zhongliang Zhuang, Gang Song, Meili Zhu, and Liming Liu. Rapid prototyping of aluminum alloy with vertical deposition by laser-arc hybrid heat source. *Hanjie Xuebao/Transactions of the China Welding Institution*, 34(5):71–74, 2013.
- [13] L Cultrera, P Miglietta, and A Perrone. Detailed studies of aluminum thin films morphology deposited by pulsed laser ablation. *Journal of Alloys and Compounds*, 504(SUPPL. 1):S399–S404, 2010.
- [14] J A Knapp and D M Follstaedt. Mechanical properties of high strength aluminum alloys formed by pulsed laser deposition. In *Proceedings of the 1995 MRS Fall Meeting, November 26, 1995 - December 1, 1995*, volume 397, pages 387–392, Boston, MA, USA, 1996. Materials Research Society.
- [15] J A Knapp, D M Follstaedt, and S M Myers. Precipitate-hardened aluminum alloys formed using pulsed laser deposition. *Journal of Applied Physics*, 79(2):1116–1122, 1996.
- [16] Shaobo Sun, Lijing Zheng, Yingying Liu, Jinhui Liu, and Hu Zhang. Characterization of Al-Fe-V-Si heat-resistant aluminum alloy components fabricated by selective laser melting. *Journal of Materials Research*, 30(10):1661–1669, 2015.
- [17] Joseph R Davis and Joseph R Davis. *Aluminum and aluminum alloys*. ASM international, 1993.

- [18] G P Dinda, A K Dasgupta, S Bhattacharya, H Natu, B Dutta, and J Mazumder. Microstructural Characterization of Laser-Deposited Al 4047 Alloy. *Metallurgical and Materials Transactions A*, 44(5):2233–2242, 2013.
- [19] S.P. Isanaka, S. Karnati, and F. Liou. Blown powder deposition of 4047 aluminum on 2024 aluminum substrates. *Manufacturing Letters*, 7, 2016.
- [20] Mohammed Naeem. Laser Processing of Reflective Materials. *Laser Technik Journal*, 10(1):18–20, jan 2013.
- [21] Malgorzata Warmuzek. *Aluminum-silicon casting alloys: an atlas of microfractographs*. ASM international, 2004.

SECTION

2. CONCLUSIONS

The aim of this project was to investigate the feasibility of fabricating custom designed, graded materials using LMD that will cater for functionality and unconventional repair. The papers presented in this dissertation document the research and success achieved in this regard. Some of the highlights from this research are,

- The successful demonstration of feasibility for using modular copper and nickel powder feedstocks, to fabricate a wide range of alloy compositions through blending and deposition
- The measurement of variation in mechanical properties across the wide range of copper-nickel alloys fabricated using LMD through the use of mini-tensile testing
- The successful demonstration of feasibility of using pulse width modulation in laser power to manipulate chemical gradient in copper-nickel FGM
- The characterization of the influence of differences in chemical gradient in copper-nickel FGMs' through DIC coupled mini-tensile testing
- The successful demonstration of feasibility of depositing Al4047 on both Al2024 and Al6061
- The extensive characterization study on the influence of substrate preheating on Al4047 deposition

REFERENCES

- [1] Koizumi, M. FGM activities in Japan. *Compos. Part B Eng.* 1997, 28, 1-4.
- [2] Miyamoto, Y.; Kaysser, W.A.; Rabin, B.H.; Kawasaki, A.; Ford, R.G. *Functionally graded materials: design, processing and applications*; Springer Science & Business Media, 2013; Vol. 5; ISBN 1461553016.
- [3] Leushake, U.; Winter, A.N.; Rabin, B.H.; Corff, B.A. General Aspects of FGM Fabrication by Powder Stacking. In *Proceedings of the Materials Science Forum*; Trans Tech Publications, 2016; Vol. 308-311, pp. 13-18.
- [4] Thummler, F. *An introduction to powder metallurgy*; Wood, I.J. and J. V, Ed.; Institute of materials: London, 1993; ISBN 090171626X.
- [5] Marple Boulanger, Jean, B.R. Graded Casting of Materials with Continuous Gradients. *J. Am. Ceram. Soc.* 2016, 77, 2747-2750.
- [6] Qian, T.; Liu, D.; Tian, X.; Liu, C.; Wang, H. Microstructure of TA2/TA15 graded structural material by laser additive manufacturing process. *Trans. Nonferrous Met. Soc. China* 2014, 24, 2729-2736.
- [7] Durejko, T.; Zietala, M.; Polkowski, W.; Czujko, T. Thin wall tubes with Fe 3 Al/SS316L graded structure obtained by using laser engineered net shaping technology. *Mater. Des.* 2014, 63, 766-774.
- [8] Liu, W.; DuPont, J.N. Fabrication of functionally graded TiC/Ti composites by laser engineered net shaping. *Scr. Mater.* 2003, 48, 1337-1342.
- [9] Ren, H.S.; Liu, D.; Tang, H.B.; Tian, X.J.; Zhu, Y.Y.; Wang, H.M. Microstructure and mechanical properties of a graded structural material. *Mater. Sci. Eng. A* 2014, 611, 362-369.
- [10] Li, W.; Karnati, S.; Kriewall, C.; Liou, F.; Newkirk, J.; Brown Taminger, K.M.; Seufzer, W.J. Fabrication and characterization of a functionally graded material from Ti-6Al-4V to SS316 by laser metal deposition. *Addit. Manuf.* 2017, 14.
- [11] Yan, L.; Chen, X.; Li, W.; Newkirk, J.; Liou, F. Direct laser deposition of Ti-6Al-4V from elemental powder blends. *Rapid Prototyp. J.* 2016, 22, 810-816.
- [12] Muller, P.; Mognol, P.; Hascoet, J.-Y. Modeling and control of a direct laser powder deposition process for Functionally Graded Materials (FGM) parts manufacturing. *J. Mater. Process. Technol.* 2013, 213, 685-692.
- [13] Clayton, R.M. *The use of elemental powder mixes in laser-based additive manufacturing*, Missouri University of Science and Technology, 2013.

- [14] Katrin I Schwendner Peter C Collins, Craig A Brice, Hamish L Fraser, R.B. Direct laser deposition of alloys from elemental powder blends. *Scr. Mater.* 2001, 45, 1123-1129.
- [15] Doubrovski, E.L.; Tsai, E.Y.; Dikovskiy, D.; Geraedts, J.M.P.; Herr, H.; Oxman, N. Voxel-based fabrication through material property mapping: A design method for bitmap printing. *Comput. Des.* 2015, 60, 3-13.
- [16] Lee, W.Y.; Stinton, D.P.; Berndt, C.C.; Erdogan, F.; Lee, Y.-D.; Mutasim, Z. Concept of Functionally Graded Materials for Advanced Thermal Barrier Coating Applications. *J. Am. Ceram. Soc.* 1996, 79, 3003-3012.
- [17] Muller, E.; DraÅar, ÄÑ.; Schilz, J.; Kaysser, W.A. Functionally graded materials for sensor and energy applications. *Mater. Sci. Eng. A* 2003, 362, 17-39.
- [18] Watari, F.; Yokoyama, A.; Omori, M.; Hirai, T.; Kondo, H.; Uo, M.; Kawasaki, T. Biocompatibility of materials and development to functionally graded implant for bio-medical application. *Compos. Sci. Technol.* 2004, 64, 893-908.
- [19] Boschetto, A.; Bottini, L.; Veniali, F. Roughness modeling of AlSi10Mg parts fabricated by selective laser melting. *J. Mater. Process. Technol.* 2017, 241, 154-163.
- [20] Feng, K.; Chen, Y.; Deng, P.; Li, Y.; Zhao, H.; Lu, F.; Li, R.; Huang, J.; Li, Z. Improved high-temperature hardness and wear resistance of Inconel 625 coatings fabricated by laser cladding. *J. Mater. Process. Technol.* 2017, 243, 82-91.
- [21] Dutta, B.; Froes, F.H. The Additive Manufacturing (AM) of titanium alloys. *Met. Powder Rep.* 2017.
- [22] Chen, X.; Yan, L.; Li, W.; Liou, F.; Newkirk, J. Effect of Powder Particle Size on the Fabrication of Ti-6Al-4V using Direct Laser Metal Deposition from Elemental Powder Mixture. *Solid Free. Fabr.* 2016.
- [23] Chakrabarti, D.J.; Laughlin, D.E.; Chen, S.W.; Chang, Y.A. Cu (Copper) Binary Alloy Phase Diagrams. *Alloy Phase Diagrams*, 1992, 3, p 2.167-2.182.
- [24] Naeem, M. Laser Processing of Reflective Materials. *Laser Tech. J.* 2013, 10, 18-20.
- [25] Davis, J.R.; Davis, J.R. Aluminum and aluminum alloys; ASM international, 1993; ISBN 087170496X.

VITA

Sreekar Karnati was born and brought up in Hyderabad, Telangana, India. He obtained his undergraduate degree in Manufacturing Science and Engineering from Indian Institute of Technology, Kharagpur, India in 2012. During his senior year, he worked on the project titled, “A Molecular mechanics investigation of the mechanical properties of functionalized CNT-epoxy composites” under the supervision of Dr. Baidurya Bhattacharya. His work involved developing a molecular dynamics model of the CNT epoxy composite and estimating its mechanical properties through simulation. After his graduation, in Fall 2012 he started graduate studies in Manufacturing Engineering at Missouri University of Science and Technology, Rolla, Missouri. During his course of study, he has worked on fabrication and characterization of advanced materials namely, functionally graded materials, high entropy alloys, and structurally amorphous materials via laser metal deposition. He received his M.S. degree in Manufacturing Engineering from Missouri University of Science and Technology in 2015. He continued his tenure at Missouri S&T to pursue PhD in Mechanical Engineering. During which he worked on his dissertation titled, “Design, fabrication, and characterization of functionally graded materials”. He has published research material in numerous journal articles and conference proceedings. He received his Ph.D. in Mechanical Engineering from the Missouri University of Science and Technology in May 2019.